

8-2010

DEVELOPMENT OF A FINITE ELEMENT MODEL TO PREDICT THE BEHAVIOR OF A PROTOTYPE WHEEL ON LUNAR SOIL

Marisa Orr

Clemson University, mkorr@alumni.clemson.edu

Follow this and additional works at: https://tigerprints.clemson.edu/all_dissertations



Part of the [Engineering Mechanics Commons](#)

Recommended Citation

Orr, Marisa, "DEVELOPMENT OF A FINITE ELEMENT MODEL TO PREDICT THE BEHAVIOR OF A PROTOTYPE WHEEL ON LUNAR SOIL" (2010). *All Dissertations*. 579.

https://tigerprints.clemson.edu/all_dissertations/579

This Dissertation is brought to you for free and open access by the Dissertations at TigerPrints. It has been accepted for inclusion in All Dissertations by an authorized administrator of TigerPrints. For more information, please contact kokeefe@clemson.edu.

DEVELOPMENT OF A FINITE ELEMENT MODEL TO PREDICT
THE BEHAVIOR OF A PROTOTYPE WHEEL ON LUNAR SOIL

A Dissertation
Presented to
the Graduate School of
Clemson University

In Partial Fulfillment
of the Requirements for the Degree
Doctor of Philosophy
Mechanical Engineering

by
Marisa Kikendall Orr
August 2010

Accepted by:
Dr. Sherrill B. Biggers, Committee Chair
Dr. Lisa C. Benson, Committee Chair
Dr. Paul F. Joseph
Dr. Joshua D. Summers

ABSTRACT

The All-Terrain Hex-Limbed Extra-Terrestrial Explorer (ATHLETE) is a mobile lunar lander under development by the National Aeronautics and Space Administration's Lunar Architecture Team. While previous lunar missions have lasted only a few days, the ATHLETE is designed to last for 10 years, which will enable a sustained U.S. presence on the moon and exploration of the more treacherous regions which are not suitable for landing. Because the ATHLETE will carry entire astronaut habitats, its six wheels must be carefully designed to support a large load on soft lunar soil efficiently.

The purpose of this thesis is to develop a finite element model that will allow designers to examine how the tractive performance of the lunar wheel is affected by changes in the wheel geometry through numerical analysis. It has been shown in the literature that a wheel rolling on soil is not suited to a plane strain analysis. Two different three-dimensional deformable wheel models are explored, a single-part shell model and a multi-part solid-shell model. For the purposes of this research, the shell model offers sufficient detail with less computational expense. The key to obtaining a smooth pressure distribution is in careful selection of the contact stiffness. For the soil model, a set of parameters to represent a pressure-dependent elasto-plastic cap hardening lunar soil was assembled. Two different methods of selecting an appropriate soil bed size are compared. A holistic method that determines all dimensions at once was found to be quick and reliable. Finally, the wheel and soil models were integrated into one finite element model in the commercial code, Abaqus™, and three small studies were conducted to demonstrate the utility of the model in predicting changes in traction due to

change in wheel design and operation. For example, the model can help determine how quickly the wheel can accelerate without significant slippage. The model can also inform design decisions. The pilot tests suggested that softening the cylinders and/or the spokes could improve traction, but softening the cylinders too much can lead to structural failure.

DEDICATION

To my wonderful husband for his love and support and to my parents for their lifelong encouragement. I could not have done it without you.

ACKNOWLEDGMENTS

First and foremost, I would like to thank Clemson University and the South Carolina Space Grant Consortium for providing the funding that allowed me to complete this work. I would also like to gratefully acknowledge the following people for their support. Timothy Reeves has been a great sounding board for ideas and inspiration. Manoj Chinnakonda, Renuka Jagadish, and Balajee Ananthasayanam all made significant contributions to the numerical modeling of the Lunar Wheel and Balajee has taught me many tricks for dealing with ABAQUS. My creative inquiry team challenged me and helped me learn about the design process. Vivake Asnani at NASA Glenn shared helpful insights about sand modeling and behavior and also provided key literature.

The guidance of my advisory committee has been invaluable. Dr. Joshua Summers allowed me the opportunity to work on this project and has kept me focused on achieving practical, useful results. Dr. Paul Joseph has an amazing ability of identifying the fundamental mechanics of a complex system such as the Lunar Wheel. He has challenged me to really understand exactly what I am modeling. Dr. Lisa Benson has been a fantastic advisor and mentor. She has helped me maintain my sanity and my funding. My committee chair, Dr. Sherrill Biggers has placed his confidence in me and allowed me the freedom to choose my own project path and develop as a well-rounded researcher. My thanks to all of you.

TABLE OF CONTENTS

ABSTRACT.....	ii
DEDICATION.....	iv
ACKNOWLEDGMENTS.....	v
LIST OF TABLES.....	ix
LIST OF FIGURES.....	xi
1. MOTIVATION.....	1
1.1 Approach.....	5
1.2 Research Objective.....	5
1.3 Research Questions.....	7
2. BACKGROUND AND LITERATURE REVIEW.....	10
2.1 Soil Mechanics.....	12
2.2 Lunar Regolith.....	20
2.3 Lunar Environment.....	23
2.4 Lunar Wheel Development.....	24
2.5 Finite Element Analysis of Wheel-Soil Interaction.....	27
3. LUNAR WHEEL MODEL.....	31
3.1 Finite Element Code Selection.....	31

3.2	Computation Time	31
3.3	Wheel Modeling and Element Selection	33
3.4	Contact.....	50
3.5	Wheel Mesh Refinement	53
3.6	Calibration	53
3.7	Summary.....	56
4.	SOIL MODEL.....	60
4.1	Material Model Selection	60
4.2	Soil Parameters	61
4.3	Reduction of Edge Effects.....	64
4.4	Boundary Conditions	72
4.5	Friction Coefficient	73
4.6	Soil Mesh Refinement.....	74
5.	DEMONSTRATION OF THE INTEGRATED MODEL	80
5.1	Start-up Effects	80
5.2	Cylinder Wall Thickness	87
5.3	Spoke Stiffness	90
6.	CONCLUSIONS AND FUTURE WORK.....	96

APPENDICES	99
Appendix A: The Stress Tensor.....	100
Appendix B: Characterization of Discrete Shear Band	102
Appendix C: Implementation on the Palmetto Cluster	107
Appendix D: Sample Abaqus Input File	112
REFERENCES.....	119

LIST OF TABLES

Table 1.1 Research Questions and Hypotheses	7
Table 2.1 Ultimate Bearing Capacity (kPa) of a Square Footing with $B = 200$ mm.	19
Table 2.2 Recommended Values for Lunar Soil Cohesion and Friction Angle [31]	21
Table 3.1 Computational Efficiency on Multiple Nodes.....	32
Table 3.2 Element Types	47
Table 3.3 Computation Times of Refined Wheel Meshes.....	50
Table 3.4 Effect of Contact Stiffness on Wheel Deflection	52
Table 3.5 Wheel Mesh Refinement.....	53
Table 3.6 Materials and Element Types by Section.....	59
Table 4.1 Soil Model Properties	61
Table 4.2 Bulk Density and Shear Strength Parameters of Soil Model Layers.....	62
Table 4.3 Soil Model Properties [87]	63
Table 4.4 Sequential Sizing Method	67
Table 4.5 Summary of Holistic Sizing Method	71
Table 4.6 Effect of Mesh Size on Holistic Method Results	72
Table 4.7 Effect of Boundary Conditions.....	73
Table 4.8 Effect of Friction Coefficient	74
Table 4.9 Soil Mesh Refinement.....	75

Table 5.1 Effect of Start-up Time on Traction	84
Table 5.2 Effect of Cylinder Wall Thickness	87
Table 5.3 Effect of Spoke Stiffness on Displacement and Contact	
Area.....	91
Table 6.1 Research Questions Answered	96

LIST OF FIGURES

Figure 1.1 All-Terrain, Hex-Limbed, Extra-Terrestrial Explorer (ATHLETE), photo courtesy NASA/JPL-Caltech	2
Figure 1.2 Lunar Wheel Concept	4
Figure 2.1 Literature Map	11
Figure 2.2 von Mises (left) and Tresca (right) Yield Criteria	13
Figure 2.3 Drucker-Prager (left) and Mohr-Coulomb (right) Yield Criteria	14
Figure 2.4 Consolidation Test Results of GRC-1 Lunar Soil Simulant	17
Figure 2.5 General Shear Failure	18
Figure 2.7 Cap Hardening of GRC-1 (linear scale)	23
Figure 2.8 Michelin Tweel™	24
Figure 2.9 First Generation Prototypes Designed by Clemson Students [5]	25
Figure 2.10 Prototype Wheel	26
Figure 3.1 Physical Prototype with Close-up of Spokes	34
Figure 3.3 Shell Model	35
Figure 3.4 Image of Full Solid-Shell Wheel Created by Mirroring Half Model	36
Figure 3.5 Finite Element Model of Lunar Wheel, 2D View	37
Figure 3.8 Shear Band	40

Figure 3.9 Shear Band Cylinder.....	40
Figure 3.10 Contact Pressure - S4R Elements.....	43
Figure 3.11 Contact Pressure - S4 Elements.....	43
Figure 3.12 Contact Pressure - C3D8R Elements, 1 Element Thick	44
Figure 3.13 Contact Pressure - C3D8R Elements, 2 Elements Thick	44
Figure 3.14 Contact Pressure - C3D8I Elements, 1 Element Thick.....	45
Figure 3.15 Contact Pressure - C3D8I Elements, 2 Elements Thick	45
Figure 3.16 Contact Pressure - SC8R Elements, 1 Element Thick.....	46
Figure 3.17 Contact Pressure - SC8R Elements, 2 Elements Thick	46
Figure 3.18 S4R Elements, Refined Mesh	49
Figure 3.19 SC8R Elements, Refined Mesh.....	49
Figure 3.20 Pressure Distribution for $k=10$ MPa/mm	51
Figure 3.21 Pressure Distribution for $k=100$ MPa/mm	51
Figure 3.22 Pressure Distribution for $k=1000$ MPa/mm	52
Figure 3.23 Experimental (gray) and Numerical (blue) Load- Deflection Curves	55
Figure 3.24 Final Wheel Model Showing von Mises Stress	57
Figure 3.25 Side View of Final Wheel Model.....	58
Figure 3.26 Final Wheel Model Contact Pressure on Rigid Surface	58
Figure 4.1 Initial Size	68
Figure 4.2 Iteration 1 – Increased Size.....	69

Figure 4.3 Iteration 2 - Decreased Size	70
Figure 4.4 Comparison of Tolerance Limits: 0.05 mm (left) and 0.5 mm (right).....	72
Figure 4.5 Results of Mesh Refinement	76
Figure 4.6 Spokes Collapsing Under Gravity Load	77
Figure 4.7 Spokes Collapsing due to Rotation.....	77
Figure 4.8 Contact Pressure due to Gravity Load (bottom is outside edge of wheel)	78
Figure 4.9 Contact Pressure due to Rotation (bottom is outside edge of wheel, rolling to the right)	78
Figure 5.1 Smooth Step Velocity Profile.....	81
Figure 5.2 Smooth Step Acceleration Profile	81
Figure 5.3 Soil Thrust over the Start-up Period.....	83
Figure 5.4 Start-up: 0 to 1 kph in 20 seconds	85
Figure 5.5 Start-up: 0 to 1 kph in 10 seconds	85
Figure 5.6 Start-up: 0 to 1 kph in 5 seconds	86
Figure 5.7 Start-up: 0 to 1 kph in 10 seconds, followed by constant speed for 5 seconds	86
Figure 5.8 Cylinder Wall Thickness = 0.7 mm (baseline)	88
Figure 5.9 Cylinder Wall Thickness = 0.5 mm.....	89
Figure 5.10 Cylinder Wall Thickness = 0.3 mm.....	90
Figure 5.12 Spoke Thickness 0.01 mm	93

Figure 5.13 Spoke Thickness 0.1 mm	94
Figure 5.14 Spoke Thickness 1 mm	95
Figure B.2 Case 1, Height = 31.2 mm, 1 cylinder set	104
Figure B. 3 Case 2, Height = 15.6 mm, 2 cylinder sets.....	104
Figure B.4 Case 3, Height = 7.8 mm, 4 cylinder sets.....	104
Figure B.5 Shear Stress vs. Strain for Three Shear Band Heights.....	105
Figure B.6 Shear Stress vs. Strain for Three Glass Cylinder Thicknesses	106
Figure C.1 Writing the Input File.....	108
Figure C.2 Uploading to the Remote Directory.....	109
Figure C.3 Creating a .pbs File	110
Figure C.4 Submitting the .pbs File to the Queue.....	111

1. MOTIVATION

As noted in *The Vision for Space Exploration*, a 2004 National Aeronautics and Space Administration (NASA) Report:

The moon will provide an operational environment where we can demonstrate human exploration capabilities within relatively safe reach of Earth. Human missions to the Moon will serve as precursors for human missions to Mars and other destinations, testing new sustainable exploration approaches, such as space resource utilization, and human-scale exploration systems, such as surface power, habitation, and life support, and planetary mobility. [1]

Exploration of areas away from potential landing sites requires a new level of mobility. One potential solution recommended by the National Aeronautics and Space Administration's Lunar Architecture Team is the development of mobile lunar landers, such as the All-Terrain, Hex-Limbed, Extra-Terrestrial Explorer (ATHLETE) [2]. The ATHLETE, as shown in Figure 1.1, is under development at the Jet Propulsion Laboratory (JPL) as part of the NASA Exploration Technology Development Program.

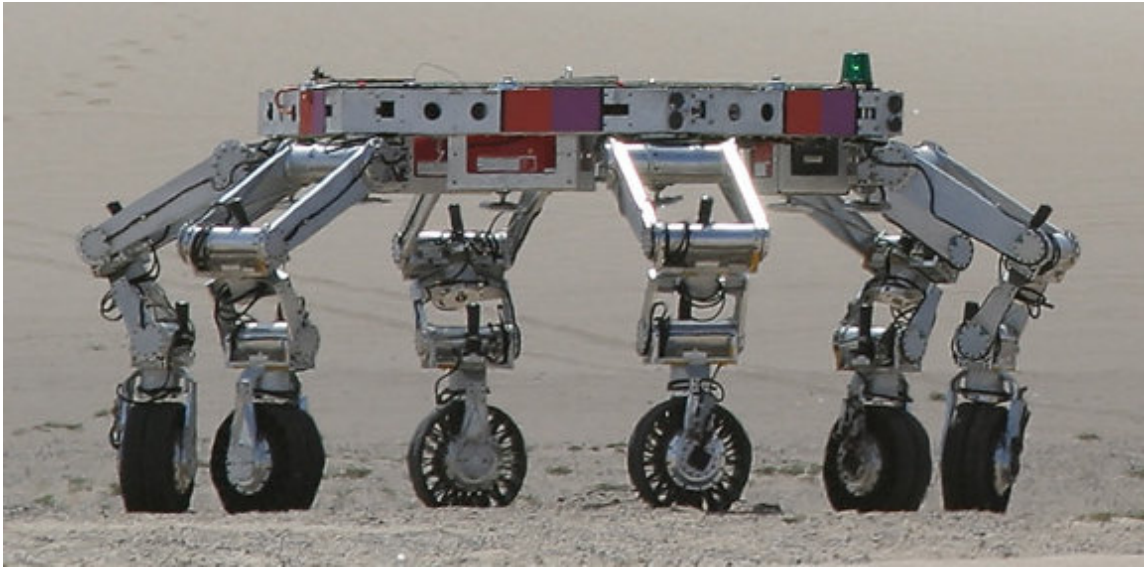


Figure 1.1 All-Terrain, Hex-Limbed, Extra-Terrestrial Explorer (ATHLETE), photo courtesy NASA/JPL-Caltech

The benefit of a mobile lander is that redundancy is reduced because many of the subsystems required for a surface vehicle are the same or identical to those required for a lander [2]. The most notable feature of the ATHLETE is the six-degree-of-freedom wheeled legs. This spider-like design enables the explorer to roll through smooth terrain or lift one limb at a time to “walk” through rough terrain. The vehicle can carry a small habitat that will allow astronauts to have a mobile base, thus allowing them to explore some of the more treacherous lunar regions.

While the ability to “walk” is useful for rough terrain, on a flat terrain, it often requires four times as much energy as rolling [3]. Careful design of wheels will enable the vehicle to use energy efficiently as it traverses the moon’s surface. Wheels used on the Lunar Roving Vehicle (LRV) were qualified to support a load of 254N per wheel for up to 120 km [4], but the design specifications for the ATHLETE, which is designed to

house a mobile astronaut habitat on the moon, require wheels that will last for 10,000 km [5] and support a load of 2500N per wheel. A simple terrestrial solution would be to use a pneumatic tire. In a lunar environment, however, pneumatic tires are not a safe option for several reasons:

- a) Rubber properties would change with the large temperature swings experienced on the moon.
- b) The moon lacks the atmosphere necessary to protect rubber from solar radiation, hence it would deteriorate quickly.
- c) A flat-tire is a single point failure that renders the wheel useless.
- d) A tire explosion in a hard vacuum would be dangerous for astronauts.

Mobility for a sustained presence on the moon requires a new level of wheel technology. One promising concept for the ATHLETE wheel is being jointly developed by Clemson University, JPL, NASA Glenn Research Center, Michelin, and Milliken through a grant from the South Carolina Experimental Program to Stimulate Competitive Research (SC EPSCoR). The design is inspired by the Michelin Tweel™, a non-pneumatic structure that retains the important characteristics of the traditional tire while removing many of the design limitations [6].

One key characteristic of pneumatic tires is that they are “top loaders,” that is, the hub is suspended from the top half of the tire. Air pressure keeps the tire from collapsing on itself. Rigid wheels do not have the constraints of maintaining air pressure, but their “bottom loader” design is not an efficient use of material. Only the material directly under the hub is supporting the load at any given time. The Tweel™ is a top loader, but

rather than air, a polyurethane shear band sandwiched between two inextensible membranes is utilized to maintain its shape. Rather than sidewalls, spokes are used to support the load on the hub. To prevent bottom loading, the spokes are designed to buckle under compression [6].

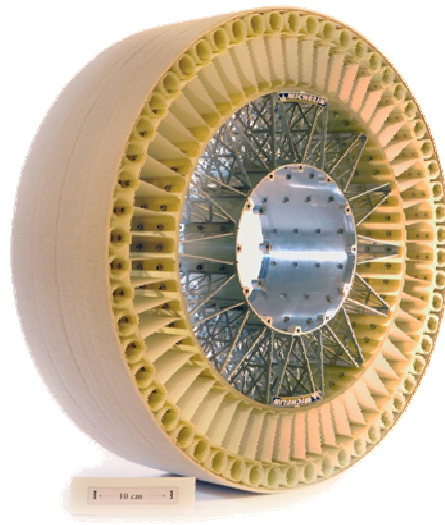


Figure 1.2 Lunar Wheel Concept

Because polyurethane cannot tolerate lunar conditions, the shear band for the lunar wheel had to be redesigned using meta-materials to replicate the shear characteristics of polyurethane. The discrete nature of the meta-materials has disrupted the uniform pressure profile of the polyurethane Tweel™, and it is not yet known how this will affect the sinkage, slippage, and pulling capacity of the wheel on the lunar terrain.

1.1 Approach

A computational continuum approach is chosen to explore the macroscopic effects of the wheel-soil interaction. Analytical approaches, such as Bekker [7-8] and Wong [9], require simplification that will not capture the level of detail required in the wheel design, therefore a numerical solution is required. The computational approaches can be divided into continuum and discrete approaches. The discrete element method focuses on microscopic interactions and can be very detailed, but is computationally very expensive per volume of soil. The region of sand affected by the ATHLETE wheel is expected to be quite large due to its load and radius (over 350 mm). Modeling such a large volume with the Discrete Element Method would require unreasonable amounts of computational time and power. For examining macroscopic measures such as traction, a finite element model using the continuum approach allows an appropriate level of wheel detail and a suitably-sized soil region at an affordable computational cost.

1.2 Research Objective

The overarching goal of this research is to develop a finite element model that will allow designers to predict the behavior of a lunar Tweel™ on lunar soil. To be of practical use to designers, the model is subjected to the following constraints:

- 1) The model will be created in an efficient, sustainable software package, which is widely available to designers and has a graphic interface that allows immediate visualization of design changes.
 - a) Efficient – The code should have parallel processing capabilities, ideally at the domain-level.

- b) Sustainable - One way to ensure the software is maintained is to select a commercial software package.
 - c) Widely-available – Using an in-house code would hamper the dissemination of the model, therefore the selected code should be commercial or open-source.
 - d) Graphic – A good graphic interface will allow designers to make changes quickly and easily with immediate visual feedback.
- 2) The maximum runtime for cluster computing will be three days or less of wall time (the actual time the designer has to wait for results). This would allow a designer to make changes throughout the week, submit a job on Friday, and have results by Monday. A design limit is not imposed on the number of processors used in the three day period. For MPI-based parallel processing, the model is divided into domains, each of which is assigned to a processor. The division of the model into domains is constrained by the model definition. For example, all elements involved in a particular contact interaction must be in the same domain. The computation wall time is driven by the largest domain. When the largest domain is as small as possible within the constraints of the model, additional processors will not decrease wall time. Three days is set as a maximum, but the wall time should be kept as small as possible to increase utility.
- 3) Because the behavior of the lunar Tweel™ on soil is not well understood, the simulations will be as realistic as possible within the above constraints. A realistic soil model will capture experimentally observed soil behaviors such as side berms and rutting. A realistic lunar Tweel™ model will consist of parts with dimensions,

properties, and features that clearly replicate those of the physical lunar Tweel™ prototype. Possible future work could include studying the wheel-soil model to determine which features may be simplified for quicker analysis without significant loss of fidelity.

1.3 Research Questions

The process of meeting the research objective can be partitioned into several components, each corresponding to a research question. The research questions driving this research are detailed in Table 1.1

Table 1.1 Research Questions and Hypotheses

Research Question #1	Does a wheel model with 3-D solid elements for some of its components offer visible improvements in the prediction of the pressure distribution of the prototype wheel over a shell-based 3-D model?
1.1	Which of the following shell element types is sufficient to predict a smooth pressure profile? <ul style="list-style-type: none"> • Fully Integrated Conventional Shell (S4) • Reduced Integration Conventional Shell (S4R)
1.2	Which of the following continuum element types is sufficient to predict a smooth pressure profile? <ul style="list-style-type: none"> • Solid (C3D8R) • Incompatible mode (C3D8I) • Continuum shell (SC8R)
1.3	Do the continuum elements offer enough improvement in the pressure profile to merit the added computational expense?
1.4	How do contact conditions affect the wheel deflection and pressure distribution?
Hypothesis #1	Using 3-D solid elements for some components of the wheel model will offer visible improvements in the prediction of the pressure distribution over a shell-based model.

Research Question #2	Can a constitutive model that captures experimentally observed soil behaviors such as side berms and rutting be implemented in the selected finite element code?
2.1	Which models are currently available in the selected commercial code?
2.2	Which models allow the use of an explicit solver?
2.3	Which models include pressure dependence?
2.4	Which models allow non-associated flow?
2.5	Which models include plastic compaction effects under hydrostatic pressure?
2.6	Which model best meets the requirements of this study?
2.7	What soil parameters should be used?
2.7.1	What soil parameters are known for lunar soil?
2.7.2	What soil parameters are known for lunar soil simulant?
2.7.3	For parameters for which no lunar soil or simulant data is available, what are reasonable approximations?
Hypothesis #2	Using a combination of parameter values from lunar soil, lunar soil simulant, and a mechanically similar terrestrial sand, a model can be selected that meets the above requirements and predicts experimentally observed soil behaviors such as side berms and rutting.
Research Question #3	How can the finite element model parameters (such as boundary conditions and soil bed dimensions) be systematically selected in order to improve efficiency and maintain accuracy?
3.1	How do far-field boundary conditions affect simulation results? (sliding vs. pinned)
3.2	How does the location of the boundaries relative to the wheel affect simulation results?
3.2.1	What depth of soil is required for convergent results?
3.2.2	What length of soil behind the wheel is required for convergent results?
3.2.3	What length of soil ahead of the wheel is required for convergent results?
3.2.4	What width of soil to the side of the wheel is required for convergent results?

Hypothesis #3	The finite element model parameters for the soil bed can be systematically selected to maximize efficiency and maintain accuracy at the millimeter level.
Research Question #4	How can the model be used to inform wheel design and operation?
4.1	Are the model predictions affected by the rate of acceleration at start-up?
4.2	Are the model predictions affected by the thickness of the cylinder walls in the shear band of the wheel?
4.3	Are the model predictions affected by the stiffness of the wheel spokes?
Hypothesis #4	The model will predict differences in traction and sinkage in accordance with design changes in the wheel model.

The first research question guides the development and selection of an appropriate wheel model. It is addressed in Chapter 3. The next two research questions guide soil model the selection and development. They are covered in Chapter 4. The goal in answering these questions is to identify the most efficient soil model in terms of providing the most realistic results within the three-day limit of cluster computing time. Research Questions #3 utilizes a rigid version of the prototype wheel to determine appropriate dimensions of the soil bed because the rigid wheel will be an extreme case that will maximize the requirements for the soil bed. The size determined will be conservative when used with deformable wheels. The deformable wheel defined in Chapter 3 is then used for determining the appropriate level of mesh refinement. Research Question #4 integrates the deformable wheel and soil models and explores the way that the integrated model can be used to inform wheel design and operation.

2. BACKGROUND AND LITERATURE REVIEW

This chapter begins with a concept map of the relevant literature (Figure 2.1). The map is composed of four main parts: Soil Characterization, Semi-Empirical Prediction, Modeling/Analytical Techniques, and Lunar Exploration. Various aspects of soil mechanics are discussed in Section 2.1; information specific to lunar soil is next in Section 2.2. Section 2.3 explains the lunar environment. The next section gives a brief history of the development of the lunar wheel, and finally, Section 2.5 details prior work in finite element analysis of wheel-soil interaction.

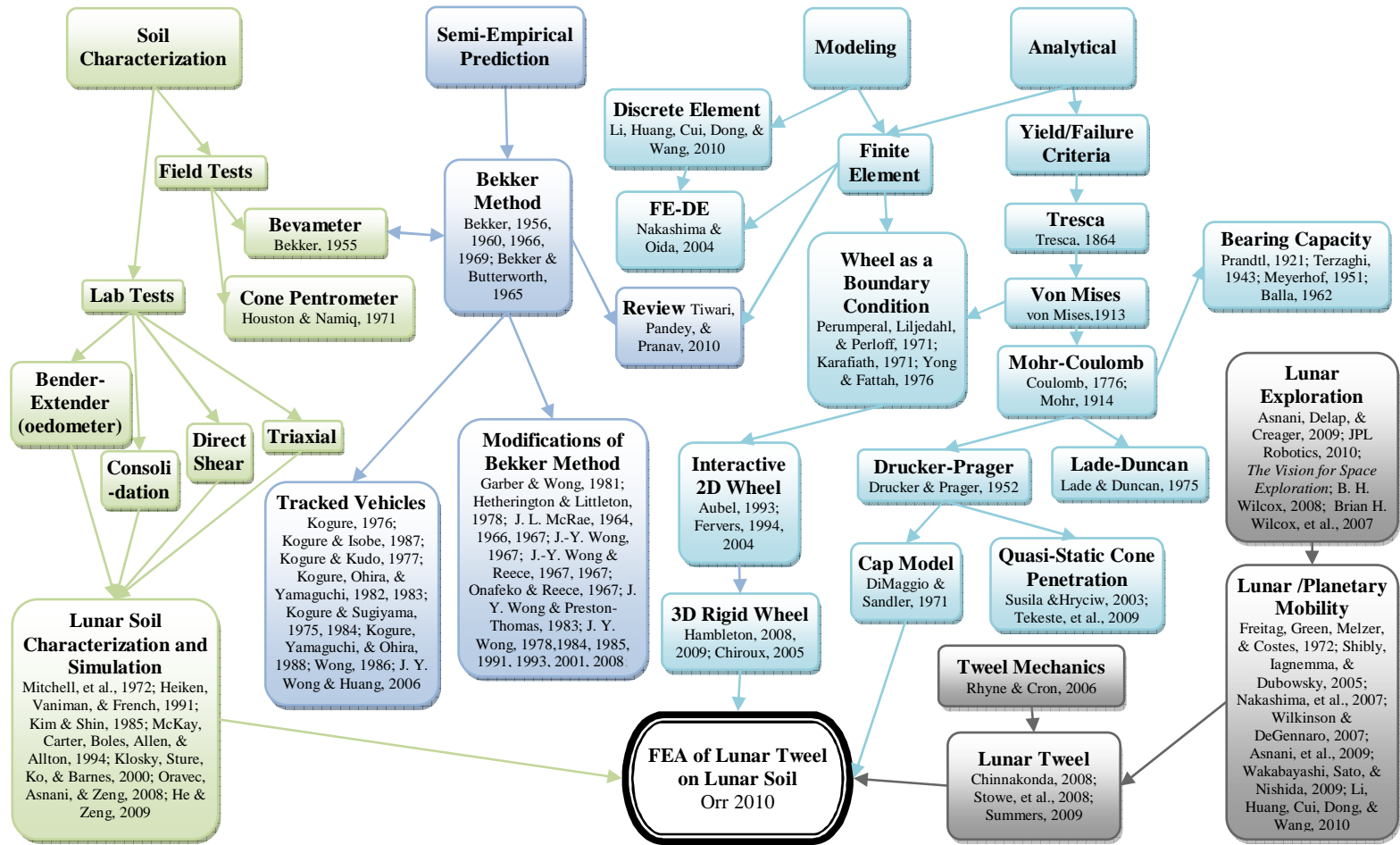


Figure 2.1 Literature Map

[1, 10-13, 7, 14-15, 8, 16-58, 6, 59, 5, 60-67, 2-3, 68-76, 9, 77-80]

2.1 Soil Mechanics

Soil is a complex material to model and predict because it has such a wide range of admissible behaviors. Macroscopically, it can behave similar to a solid or a liquid; it might hold its shape or flow, compress or expand. Microscopically, particles can slide, roll, interlock, or crush. Soil behavior depends on a range of criteria, including confining pressure, deviatoric stress, relative density, and stress history.

2.1.1 Shear Strength

Since the 1700's, soil mechanists have realized that most soil deformation is irreversible, and therefore principles of elasticity are inadequate for predicting soil behavior. In fact, plasticity principles have been in use in the study of earth pressure even before plasticity theory formally existed. Tresca's 1868 yield criterion is actually special case of Coulomb's 1773 theory of earth pressure [81].

The Tresca and von Mises models are dependent on the maximum shear stress and second invariant, respectively. These models were developed for metals but provide reasonable approximations for cohesive soils like clay. In principle stress space, the von Mises criterion is an infinite cylinder around the hydrostatic stress axis (the line $\sigma_1 = \sigma_2 = \sigma_3$), and the Tresca criterion is an infinite hexagonal prism inscribed within the von Mises cylinder. These are illustrated in Figure 2.2 Dry, sandy, lunar soil is considered a frictional soil. Just as the force of friction that can be developed between two objects depends on the normal contact force, the shear stress that can be endured by a frictional soil without plastic deformation depends on the normal stress.

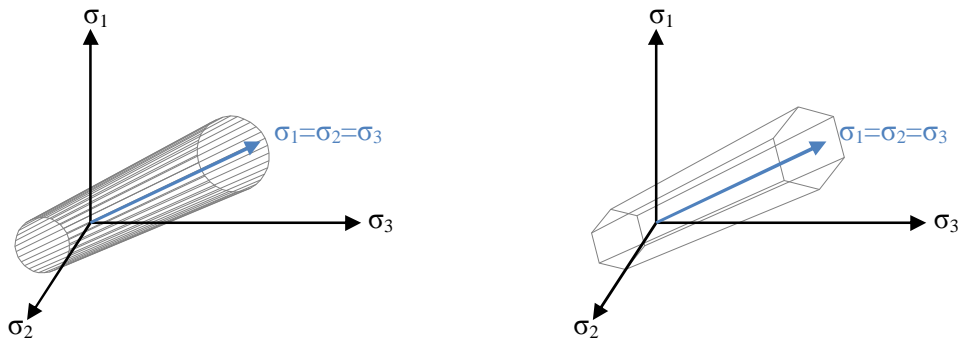


Figure 2.2 von Mises (left) and Tresca (right) Yield Criteria

A common and relatively simple yield criterion for soil that includes the normal stress is the Mohr-Coulomb Criterion. This criterion states that the shear strength of a soil at any point is equal to a cohesive component plus a frictional component that depends on the normal stress. The cohesion, c , represents the shear strength of the soil in the absence of confining pressure. As the normal stress, σ_n , increases, the shear strength of the soil, τ , increases by σ_n times the tangent of the internal angle of friction, ϕ . The tangent of ϕ is similar to a Coulomb friction coefficient. The Mohr-Coulomb yield surface can be written:

$$\tau - c - \sigma_n \tan \phi = 0 \quad (2-1)$$

The sign convention adopted for this text is that compressive stresses are positive. This is a common practice in soil mechanics because tensile stresses are practically non-existent. In principal stress space, this creates a semi-infinite pyramid with a hexagonal cross-section around the hydrostatic axis.

The Drucker-Prager yield criterion uses the mean pressure, p , to create a smoothed version of the above condition, which results in a semi-infinite cone, defined by equation (2-2),

$$t - d - p \tan \beta = 0 \quad (2-2)$$

where d and β are soil parameters which can be chosen such that the cone circumscribes or inscribes a particular Mohr-Coulomb surface and t is a measure of the deviator stress.

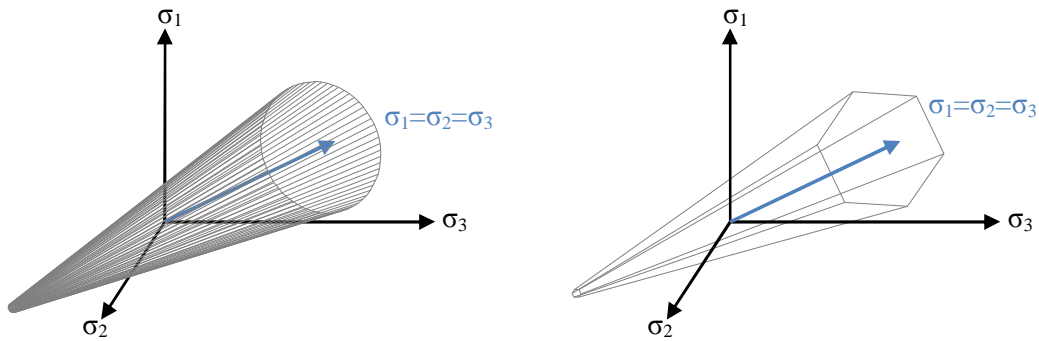


Figure 2.3 Drucker-Prager (left) and Mohr-Coulomb (right) Yield Criteria

For three-dimensional problems, the Mohr-Coulomb parameters can be converted as shown in equations (2-3) and (2-4) to create a Drucker-Prager surface that circumscribes (using the minus signs) or inscribes (using the plus signs) the Mohr-Coulomb surface [82].

$$\tan \beta = \frac{6 \sin \phi}{3 \pm \sin \phi} \quad (2-3)$$

$$d = \frac{6c \cos \phi}{3 \pm \sin \phi} \quad (2-4)$$

The variable t is a measure of the deviator stress which is related to the Mises equivalent stress, q , and the third invariant of the deviatoric stress, r , by parameter K as shown in equation (2-5) [83]. More detail about the stress invariants is given in Appendix A.

$$t = \frac{q}{2} \left[1 + \frac{1}{K} - \left(1 - \frac{1}{K} \right) \left(\frac{r}{q} \right)^3 \right] \quad (2-5)$$

When K is unity, the failure surface is a circle in the deviatoric plane, centered about the hydrostatic axis, and

$$t = q = \sqrt{\frac{1}{2} \left[(\sigma_1 - \sigma_2)^2 + (\sigma_2 - \sigma_3)^2 + (\sigma_1 - \sigma_3)^2 \right]} \quad (2-6)$$

When K is less than unity, the third invariant of the deviatoric stress, r , is incorporated into the rule. In terms of principal stresses,

$$r = \frac{(\sigma_1 + \sigma_2 - 2\sigma_3)(\sigma_1 - 2\sigma_2 + \sigma_3)(2\sigma_1 - \sigma_2 - \sigma_3)}{27} \quad (2-7)$$

Because sand quickly becomes non-linear and inelastic, a common modification to the Drucker-Prager shear failure surface is to add an elliptical cap to the wide end and a smooth transition surface from the cone to the cap. If the sand reaches the elliptical surface, the resulting plastic flow is assumed to be associated. Most metals exhibit associated flow, which means that the strain increment aligns with the stress increment. In other words, the plastic potential surface is the same as the yield surface. If the stress state reaches the Drucker-Prager surface, the sand is assumed to exhibit non-associated flow. In this case, the plastic potential is assumed to be an elliptical surface.

2.1.2 Compressibility

The cap is added to the Drucker-Prager model to capture the non-linear compressibility of soil. Initially, the soil compresses easily as the individual grains resituate. Once the sand is firmly packed, further compression requires crushing or compressing of the individual grains. In terms of continua, this is modeled as a logarithmic strain hardening curve. This curve is defined in equation (2-8) by the compression index (C_c) and swelling index (C_s) of the soil, as well as an initial pressure (p_0) and initial void ratio (e_0). The plastic volumetric strain, ε_{vol}^p , can be calculated as:

$$\varepsilon_{vol}^p = \frac{C_c - C_s}{2.3(1 + e_0)} \ln\left(\frac{p}{p_0}\right) \quad (2-8)$$

The compression and swelling indices can be obtained from a consolidation test. The void ratio is a volumetric ratio of void to solid material. The void ratio plus one yields the total bulk volume of one unit of solid volume. The results of a consolidation test of a lunar soil simulant, GRC-1 are shown in Figure 2.4. The test begins at a known void ratio (top left corner of the graph) and then slowly consolidates the soil by increasing the pressure. The slope of this line is the compression index. The soil is then decompressed back to the initial pressure and then recompressed. Because the soil does not expand all the way back to its initial void ratio, the decompression/recompression lines have a shallower slope, which is the swelling index.

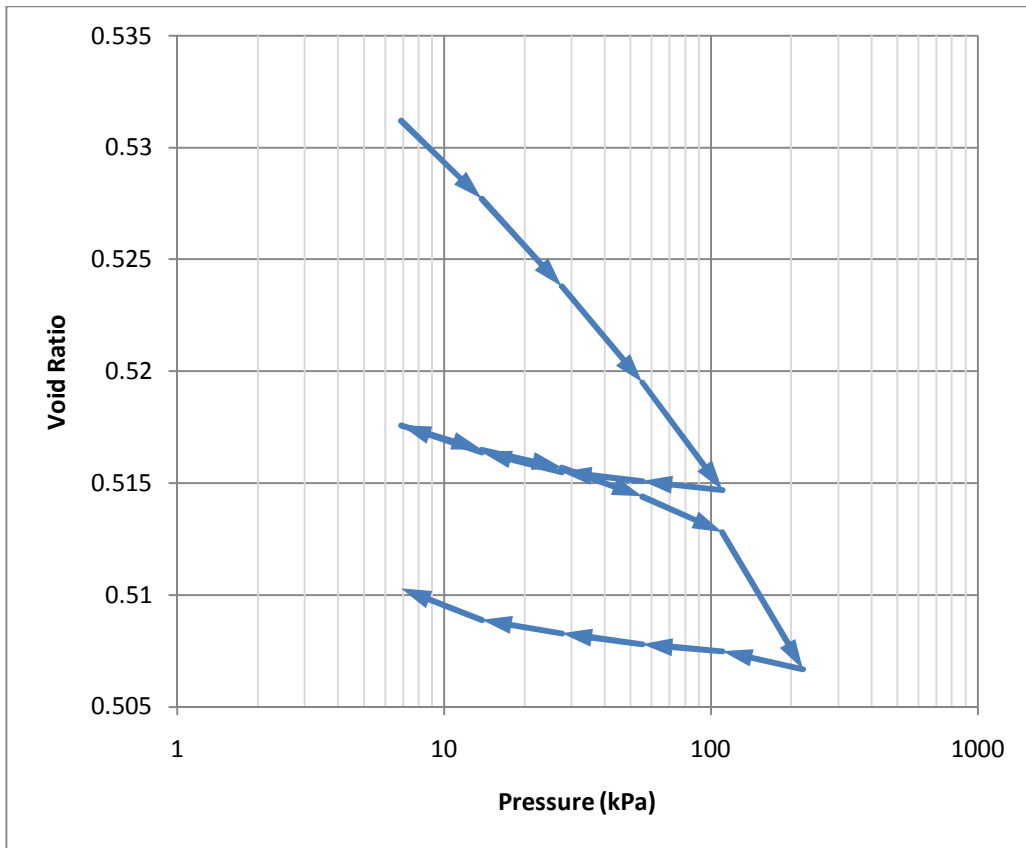


Figure 2.4 Consolidation Test Results of GRC-1 Lunar Soil Simulant

2.1.3 Bearing Capacity

Another useful concept from geotechnical engineering is the calculation of bearing capacity. This work began with Terzaghi in 1943 [63] who used Prandtl's plastic failure theory [58] to predict bearing capacity for shallow strip footings. He assumed the soil would fail by general shear failure, illustrated in Figure 2.5. He removed any soil above the base of the foundation (the overburden) and replaced it with a surcharge pressure equivalent to its weight, q . This effectively neglects any shear resistance developed in the overburden layer. The wedge of soil right below the foundation (zone I)

is pushed downward. The failure surface that develops pushes the radial zones (zones II) outward, which in turn push the Rankine passive zones (zones III) upward.

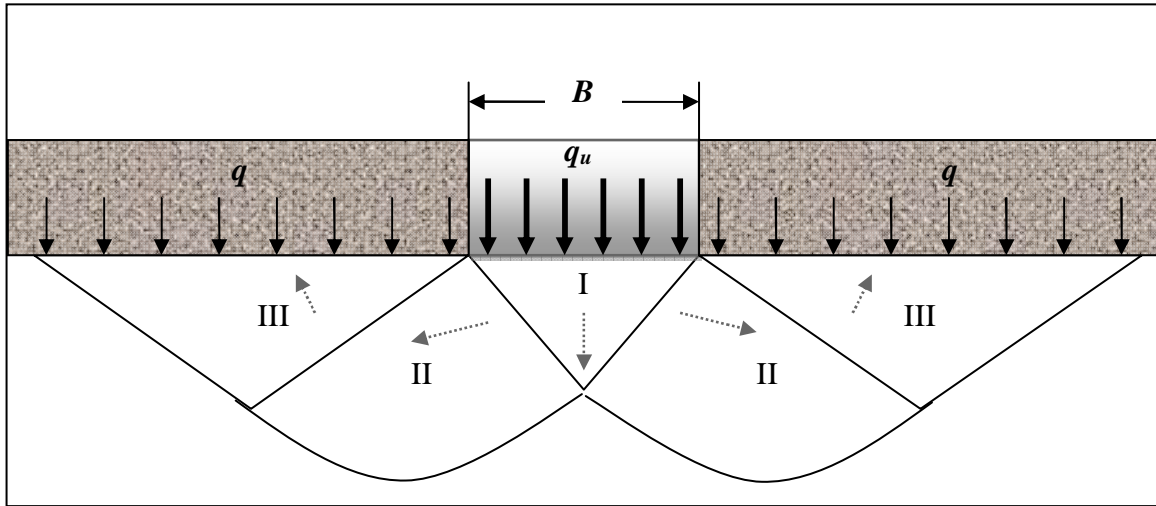


Figure 2.5 General Shear Failure

Based on the failure mechanism shown in Figure 2.5, Terzaghi used superimposition to approximate the ultimate bearing capacity, q_u . Terzaghi's work was later refined by Meyerhof [51, 84], Balla, and DeBeer and Vesic. One refinement was the discovery that the upper vertices of zone I make an angle of $45+\phi/2$ degrees below horizontal, not ϕ degrees, as Terzaghi had predicted. Although there has been some disagreement over the calculation of the bearing capacity factors, the form remains the same. For a square footing, the ultimate bearing capacity, q_u , is

$$q_u = q_c + q_q + q_\gamma = 1.3cN_c + qN_q + 0.4\gamma BN_\gamma \quad (2-9)$$

The bearing capacity depends on the cohesion of the soil, c ; the surcharge (weight of the soil that was removed from the analysis), q ; the bulk unit weight of the soil, γ ; and the

most narrow dimension, B , of the foundation. The bearing capacity factors can be calculated as follows:

$$N_c = (N_q - 1) \cot \phi \quad (2-10)$$

$$N_\gamma = (N_q - 1) \tan(1.4\phi) \quad (2-11)$$

$$N_q = e^{\pi \tan \phi} \tan^2 \left(45 + \frac{\phi}{2} \right) \quad (2-12)$$

These equations yield the bearing capacities listed in Table 2.1 for a situation where the overburden depth is zero.

Table 2.1 Ultimate Bearing Capacity (kPa) of a Square Footing with $B = 200$ mm.

Friction Angle, ϕ (degrees)	Cohesion, c (kPa)					
	0	0.01	0.1	1	10	100
30	22	23	26	61	414	3940
35	52	53	58	112	652	6049
40	132	133	142	230	1111	9923
45	371	373	389	545	2112	17775
50	1234	1238	1269	1581	4704	35929

2.1.4 Critical State Soil Mechanics

Another way of studying soil mechanics is based on the concept of a critical state [85] at which a saturated soil will flow as a frictional fluid without further changes in stress or specific volume. This behavior has been observed in saturated reconstituted clays. The first models based on this theory are the Cam Clay and the Modified Cam Clay models, which, as their names suggest, were developed with the intention of

predicting the behavior of clay. More recently, models based on critical state theory have been developed for sand, but typically require complex yield surfaces. It is unclear whether these models predict the behavior of dry sand with any accuracy. Furthermore, the critical state methods require many parameters, some of which have little or no useful physical meaning [81], and little critical state data is available for sands. Because lunar soil can be described as a frictional-cohesive silty sand, and there is no water on the moon to saturate the soil, the critical state models will not be considered further in this research.

2.2 Lunar Regolith

One of the most comprehensive resources for lunar information is the “Lunar Sourcebook: A User’s Guide to the Moon” [31]. The moon is made up of relatively flat areas, called lunar maria that are covered with dry, frictional, silty sand and mountainous regions referred to as highlands [31]. The term “regolith” includes all loose rocks, sand, and silt that are not part of the lunar bedrock. The lunar maria are fairly smooth regions comprised mainly of iron and titanium from basaltic lava flows. Here the regolith is believed to be 4-5 m deep. The highlands are mountainous regions largely made up of calcium and aluminum. The regolith is believed to be roughly 10-15 meters deep in the highlands. The entire surface is coated with a fine dust that is highly electrostatically charged.

The lack of atmosphere (15 orders of magnitude less than Earth’s atmosphere) and water results in particles that are unweathered and angular. They have been formed largely by meteoroids shattering the rock. The jagged edges afford interlocking between

particles which produces unusually high shear strength. The bulk density and shear strength varies with depth from the surface. The Lunar Sourcebook [31] recommends the values shown in Table 2.2 for the bulk density and Mohr-Coulomb shear strength parameters. Additionally, they proposed the following model for depths up to 3 meters:

$$\rho = 1.92 \frac{z + 12.2}{z + 18} \quad (2-13)$$

Table 2.2 Recommended Values for Lunar Soil Cohesion and Friction Angle [31]

Depth Range (cm)	Bulk Density, ρ (g/cm³)	Cohesion, c (kPa)	Friction Angle, ϕ (degrees)
0-15	1.50	0.52	42
0-30	1.58	0.90	46
30-60	1.74	3.00	54
0-60	1.66	1.6	49

The properties listed in Table 2.2 have been used by NASA's Glenn Research Center to create a lunar soil simulant with mechanical properties similar to the lunar soil [56]. This soil, called GRC-1, is a mixture of terrestrial sands that can be easily and inexpensively obtained for testing purposes.

He and Zeng [30] at Case Western Reserve reported the compression index and swelling index of GRC-1 to be 0.02 and 0.005, respectively. This hardening curve, along with several experimental data points is shown in Figure 2.6 and Figure 2.7.

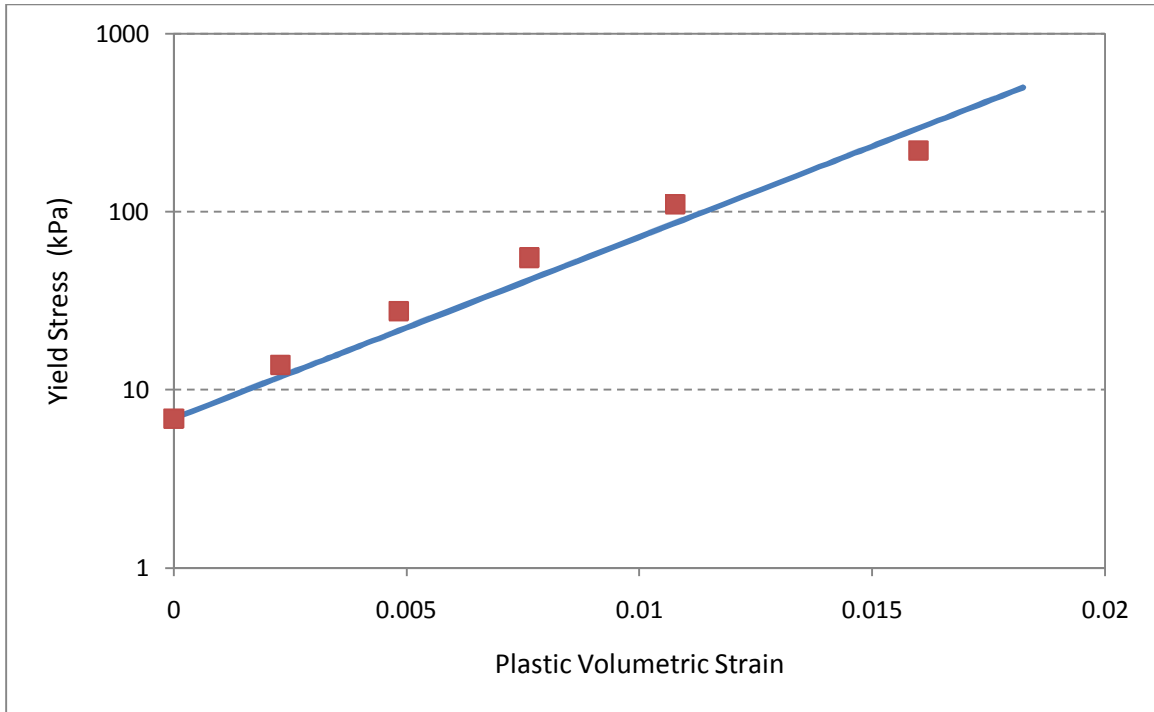


Figure 2.6 Cap Hardening of GRC-1 (semilog scale)

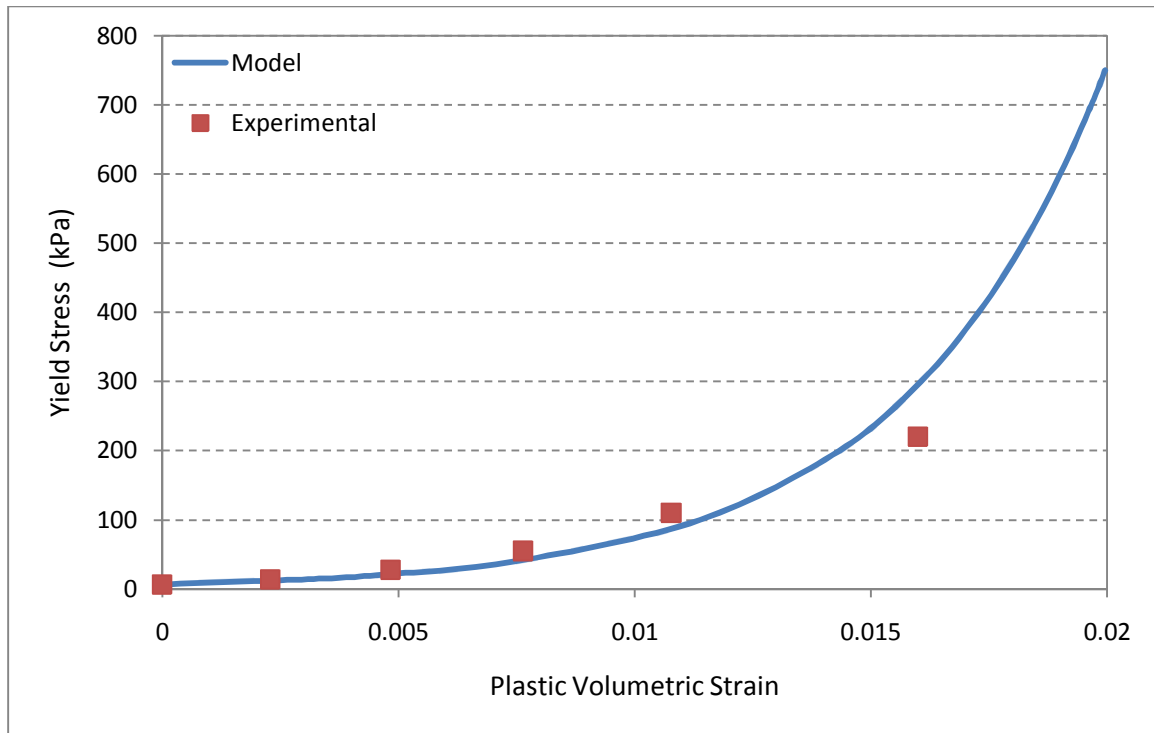


Figure 2.7 Cap Hardening of GRC-1 (linear scale)

2.3 Lunar Environment

Environmentally, the moon is a treacherous place. The temperature ranges from 100 to 400 Kelvin (-280 to 260 Fahrenheit). Because the same side of the moon always faces the earth, one rotation corresponds to one complete orbit around the earth. One lunar day is 27.3 earth days [86]. Long days and nights result in huge temperature swings. The average daytime temperature is 107°C and the average nighttime temperature is -153°C [31]. Radiation is also a concern, as there is no atmosphere to shield the lunar surface from solar rays and meteors. These conditions severely limit the material choices available for use on lunar missions.

2.4 Lunar Wheel Development

The Tweel™ is the non-pneumatic integrated tire/wheel developed by Michelin and recognized as one of the TIME 2005 Inventions of the Year¹ (shown in Figure 2.8). The benefit of the Tweel™ is that it can maintain relatively uniform contact pressure without pneumatics, which makes it a good candidate for lunar exploration; however, the design of the Tweel™ relies heavily on the low shear modulus and incompressibility of polyurethane, which cannot endure the extreme lunar temperatures.



Figure 2.8 Michelin Tweel™

One key characteristic of pneumatic tires is that they are “top loaders,” that is, the hub is suspended from the top half of the tire. Air pressure keeps the tire from collapsing on itself. Rigid wheels do not have the constraints of maintaining air pressure, but their “bottom loader” design is not an efficient use of material. Only the material directly

¹ <http://www.time.com/time/business/article/0,8599,1129516,00.html>

under the hub is supporting the load at any given time. The Tweel™ is a top loader, but rather than air, a polyurethane shear band sandwiched between two inextensible membranes is utilized to maintain its shape. Rather than sidewalls, spokes are used to support the load on the hub. To prevent bottom loading, the spokes are designed to buckle under compression [6].

On a flat, rigid surface, the contact pressure, p_c , of a Tweel™ can be approximated by equation (2-14)

$$p_c \cong \frac{Gh}{R} \quad (2-14)$$

where G is the shear modulus of the circumferential elastic beam, h is the height of the beam, and R is the outer radius [6].



Figure 2.9 First Generation Prototypes Designed by Clemson Students [5]

Lunar wheels inspired by the Tweel™ have been under development at Clemson University since 2006 when a partnership was established with Michelin and JPL. Soon after, Milliken and NASA Glenn Researchers were brought into the project as well. The

first generation prototypes shown in Figure 2.9 were the result of a senior design project to redesign the Tweel™ using non-polymeric materials. Their designs were then advanced by Conger and analyzed for wear and fatigue concerns by Stowe [5].



Figure 2.10 Prototype Wheel

Currently, a third generation lunar wheel has been constructed by Michelin, shown in Figure 2.10. At the center of the prototype wheel is a metal truss system which represents the hub. The wheel motor and tool attachments will eventually be housed in this area. To allow counter-deflection, the spokes must be extensible; however, the sailcloth material used for the spokes has a large elastic modulus. To combat this problem, the spokes are wrapped over a short curved plate made of a glass composite. Tension in the spoke causes the plate to bend, which results in an overall extensibility of the spoke system. The outer edge of the spoke is connected to the inner membrane. Both the inner and outer membranes are made from glass composite which has little

extensibility in the circumferential fiber direction. The shear band between these two membranes is composed of concentric cylinders which are riveted to each membrane. Finally, a 2mm layer of a felt-like material is wrapped around the outer membrane. This compliant layer helps to subdue the pressure spikes that arise from the discrete nature of the shear band.

The hub is continuous along the axis of the wheel, but the spokes and inner membrane have two lobes with an 8 mm gap between them. Each lobe is connected to two cylinder and outer membrane segments, with a 6 mm gap between them.

2.5 Finite Element Analysis of Wheel-Soil Interaction

Perumpral [57] is often credited with the first finite element prediction of soil deformation under a wheel. A piecewise linear elastic model was used for the soil. The initial shape of the soil included a wheel indentation with an equally deep rut behind it. As with all early models, the wheel was not actually modeled, but represented by a stress distribution based on experimental data from Onafeko and Reece [55].

In 1976, Yong and Fattah [80] used the elasto-plastic von Mises criterion to predict yield and incorporate the unloading response of a rigid wheel represented by a displacement boundary condition.

Until Aubel [11] published his seminal work in 1993, the interaction between wheel and soil had been determined by hand, subject to many idealizations, and then input into the finite element code as a boundary condition. Aubel coupled an elastic tire model and a Drucker-Prager soil model with non-associated plastic flow. For the first

time, the external loading was used as an input to the simulation and the contact shape, stresses, and deformations were the resulting output.

In the following year, Fervers [22] implemented a similar model that incorporated a rigid wheel with a lugged profile. In later works, he developed a 2-D finite element model of an air-filled tire which included a rim, an air-filled volume, a belt, and a layer of tread [23]. The tire carcass is accounted for by imposing a load-deflection relationship between the rim and the outer edge of the tread.

Hambleton and Drescher [26-28] used Abaqus/Explicit to show that three-dimensional effects are significant for rigid wheels on sand and confirmed this experimentally using particle image velocimetry. Plane strain simulations were matched with a cylinder that spans the width of the sand container. In this case, shear bands imitating Prandtl's solution for failure of a soft material under a punch (which is the basis for Terzaghi's analysis of failure under a shallow foundation) were visible. However, when a wheel that does not span the entire width of the container but is flush to one side is indented into the sand, the results are quite different. In addition to the fact that a berm (upheaval of sand) develops to the side of the wheel, the displacement of the sand lacks the sharp gradients observed in the plane strain case. Instead, the displacements are large near the wheel and gradual diminish with depth and horizontal distance away from the wheel. This phenomenon was also observed in the simulations which modeled the sand using a modified Drucker-Prager model with a non-associated flow rule. The goal of Hambleton and Drescher's work was to develop approximate analytical prediction of rut

depth based on wheel and soil parameters (vertical and horizontal forces, wheel width, wheel diameter, soil density, friction angle, cohesion).

Chiroux et al. [18] successfully modeled three-dimensional wheel-soil interaction including compaction effects in Abaqus/Explicit using a cap plasticity soil model. The distinctive features of this study are;

(1) The wheel is dynamically loaded by a vertical weight force and a rotation, rather than a forced sinkage and/or translation.

(2) A dynamic analysis was used to provide a time history of the interaction and the dynamic behavior.

(3) Although the number of elements was limited by computational resources (a single engineering workstation), dividing the soil into multiple, independently meshed parts connected by surface ties allowed the researchers to mesh efficiently. Additionally, infinite elements were used at a distance in front of and behind the wheel.

The Chiroux study provides a feasibility check for the study presented here, but lacks the rigor to draw any firm conclusions. A shallow depth of soil (less than $0.4d$) was modeled and there is no evidence of any convergence checks.

The present study combines both a sophisticated soil model and a realistic wheel model that will enable a designer to make informed decisions about the wheel design. The soil model used is similar to that of Chiroux except that it is stratified to represent the variation of properties with soil depth, and rather than infinite elements, which are not well documented in the literature or fully explained in the software documentation, a larger region of soil is modeled using coarse elements far away from the wheel

interaction. The lunar wheel is an entirely new concept, thus only simple 2D models have been generated prior to this work, and they have not yet been widely published.

3. LUNAR WHEEL MODEL

3.1 Finite Element Code Selection

In accordance with the research objectives outline in Chapter 1, Abaqus/CAE: the Complete Abaqus Environment™ was selected for the creating and analyzing the finite element model. This product meets the constraints of being efficient, sustainable, widely available, and graphic. Additionally and perhaps most importantly, it is licensed at the researcher's home institution. Abaqus™ is efficient because it has MPI (Message-Passing Interface) parallel processing capabilities that allow the problem to be parallel processed at the domain level. The model is actually partitioned between processors, which is more efficient than thread-based processing where lower-level tasks are parsed between processors. Because the code is commercial, it is expected that it will be maintained by Dassault Systemes for the foreseeable future. The software package is expensive, but available to any organization. The graphic interface included in the Complete Abaqus Environment™ allows designers to graphically make changes to the model and see results instantly.

3.2 Computation Time

The Palmetto Cluster was used for parallel processing the simulations on multiple nodes. Details of this process can be found in Appendix C. Each node has a dual processor and each processor has four cores, for a total of 8 cores per node. The relationship between cores and wall time is not linear because as the number of cores

increases, so does the interaction among cores. Inevitably, one core will have to wait on output from another core. Minimizing the wait time is known as load balancing. The time spent actually executing tasks (not waiting on input) is called CPU time. The actual elapsed time is called the wall time. CPU usage is the ratio of the CPU time to the maximum possible CPU time, which, in this case is the eight times the wall time (because the master node has eight cores). The CPU usage is essentially a measure of efficiency. A sample job of a rigid wheel on soil made up of 165672 elements was run multiple times to examine the effect of using multiple nodes. As Table 3.1 shows, using multiple nodes decreases the wall time dramatically. Even with 10 nodes, the CPU usage is over 90%. Using 20 nodes for the same simulation causes a significant drop in the efficiency of the individual cores, but the wall time is still reduced. The efficiency with which a job can be parallel processed is problem dependent. For small problems, such as those with only the wheel, two nodes were used. Problems modeling the soil were run on 10 or 20 nodes.

Table 3.1 Computational Efficiency on Multiple Nodes

Nodes	Wall time	CPU time of master node (8 cores) (hh:mm:ss)	Max possible CPU time (wall time *8 cores) hh:mm:ss	CPU usage
1	24:00:32	177:39:48	192:04:16	92%*
2	10:24:32	82:16:40	83:16:16	99%
10	2:39:30	19:22:57	21:16:00	91%
20	1:58	11:37:06	15:44:00	74%

* Job did not complete in the 24 hr time limit, so results may not be representative

3.3 Wheel Modeling and Element Selection

Two finite element models of the wheel have been developed. The first is an extrusion of a single wire frame; the second is built up of 175 part instances connected by surface-to-surface ties. The physical prototype (Figure 3.1) is made up of rigid metal hub, collapsible spokes, and a shear band (double cylinders sandwiched between two inextensible rings). The models are designed to mimic the mechanics of the prototype in an efficient way while maintaining a geometric configuration similar to the actual prototype wheel. In both models, only the outer perimeter of the rigid hub is modeled. In the figure, a tread covers the 6-8 mm gaps between the four lobes which are captured by the solid model, but not by the shell model. Note that each of the spokes wraps over a curved piece of glass composite. The spoke material is too stiff to allow the wheel to work properly, but as these springboards bend, the spoke is effectively lengthened.

Each model is described in more detail in the Sections 3.2.1 and 3.2.2. In section 3.3.3, the different element types available for each are discussed and results are compared.

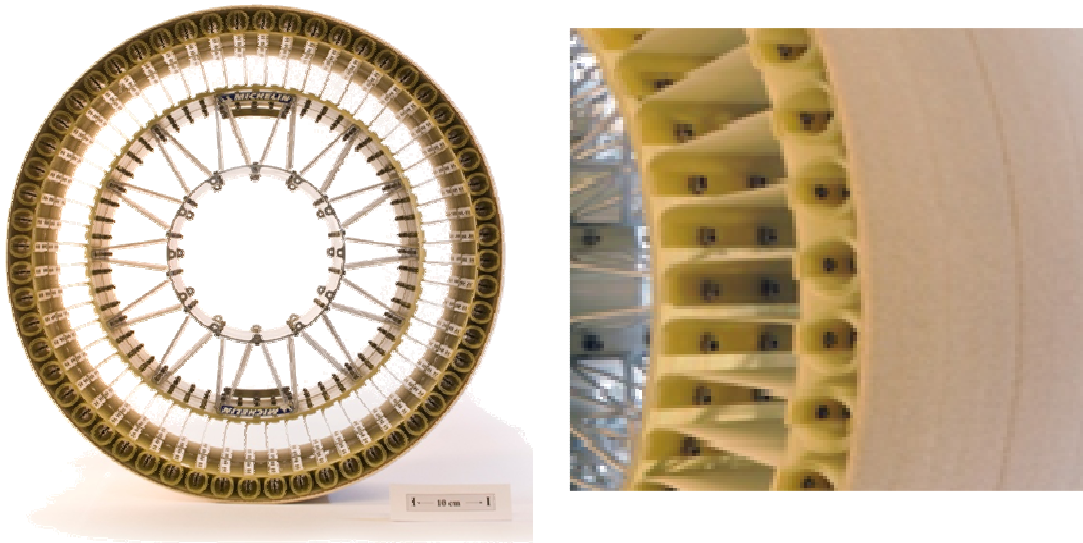


Figure 3.1 Physical Prototype with Close-up of Spokes

The actual wheel is made largely from a unidirectional glass composite; however, an explicit analysis in ABAQUS allows only isotropic materials. Because of the geometry of the wheel, this simplification had little impact on the final results.

3.3.1 Shell Model

The basis for the shell model is the sketch shown in Figure 3.3. This wire frame is then extruded to create one half of the wheel. The figure shows the full wheel, but because of symmetry only half has to be modeled. Although the wheel is one part, each section can have different properties. Shell elements are used everywhere except the straight part of the spokes. The springboards (curved part of the spoke that attaches to the hub) are meshed with shell elements that have bending resistance. The actual spoke is meshed using membrane elements that do not support any bending or transverse shear loads. Because they transmit only in-plane loads, membrane elements are ideal for representing the spoke material that has a large stiffness in tension but collapses easily in

compression. The cylinders are connected to the inner and outer rings along an axial line and contact is not defined between them. The lines in the left figure represent the midplane of each shell.

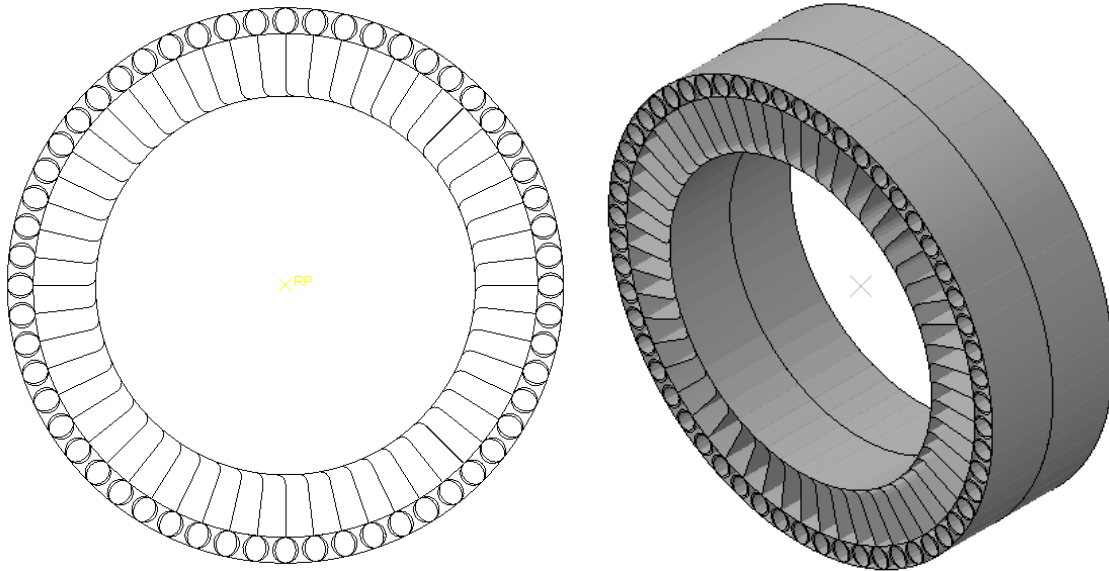


Figure 3.3 Shell Model

3.3.2 Solid-Shell Model

The solid-shell model was built part by part and then assembled using surface-to-surface ties. The inextensible rings are modeled as three-dimensional solid parts. Each double cylinder set and spoke is modeled separately as a shell. The assembly as a whole is described first, followed by the individual parts.

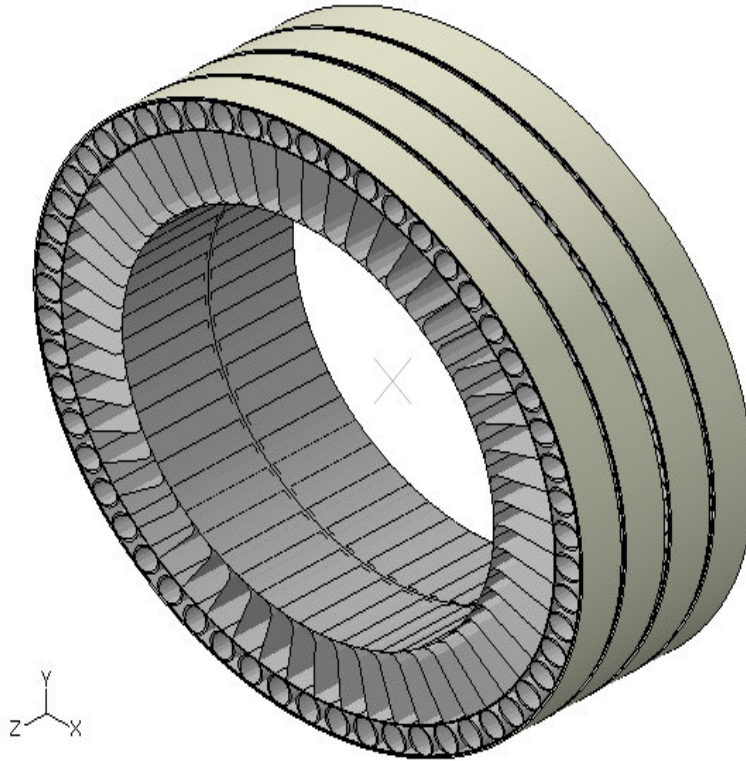


Figure 3.4 Image of Full Solid-Shell Wheel Created by Mirroring Half Model

Due to the symmetry of the problem, only half of the wheel is modeled. In Figure 3.4 above, the half-model is mirrored to give an image of the full wheel. The hub is one solid piece, while the spokes and inner membrane have two 106 mm segments separated by an 8 mm gap. Each 106 mm lobe has two cylinder and outer membrane segment that are 50 mm each, separated by a 6 mm gap. With the exception of the gaps, the wheel is prismatic along the z -axis. For the remainder of the document, only the modeled half will be shown.

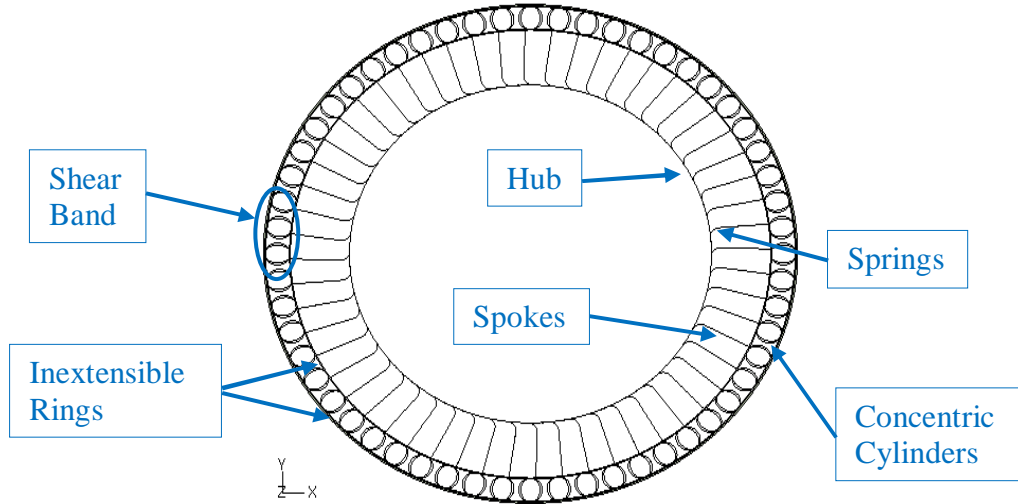


Figure 3.5 Finite Element Model of Lunar Wheel, 2D View

A two-dimensional view of the wheel is given in Figure 3.5. The inner circle represents the hub and is rigidly tied to a reference point at the center of the wheel. It is a discrete rigid cylindrical shell. In the prototype wheel, the hub is a rigid truss system that will house the wheel motor. At the central reference point, a translational inertia of 1500 kg is added to represent the mass of the lunar rover.

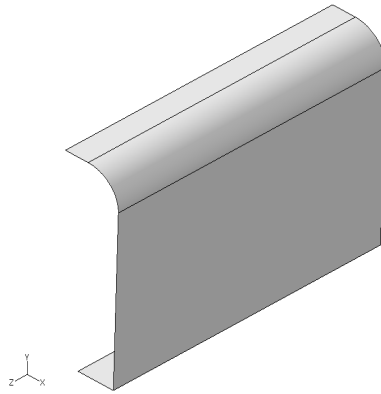


Figure 3.6 Spoke

The spoke system is modeled as one part with three sections (Figure 3.6). The curved top section and the bottom flat section are made of shell elements, while the middle section is composed of membrane elements that do not support any bending or transverse shear loads. Because they transmit only in-plane loads, membrane elements are ideal for representing the spoke material that has a large stiffness in tension but collapses easily in compression. Technically, these elements can support pure in-plane compression, but the geometry is such that a compressive load also causes bending, which the membrane elements cannot resist, and therefore the spokes collapse as shown in Figure 3.7.

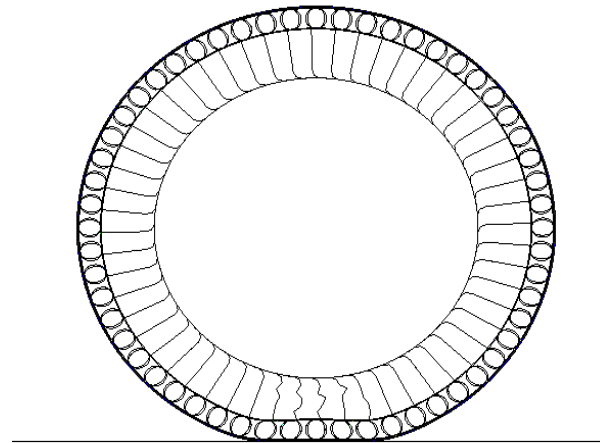


Figure 3.7 Deformed Wheel Shape

Each spoke is fixed to the inner ring of the shear band at the edge of the small cylinders, which are also fixed to the outer membrane (Figure 3.8). As shown in Figure 3.8 and Figure 3.9, the connected regions are modeled as flat surfaces which are joined by concentric elliptic semi-cylinders. These are modeled with conventional thin shell elements. A detailed analysis of the relationship between the cylinder properties and the effective shear modulus is given in Appendix B.

The inextensible rings are modeled with solid continuum elements that allow transverse shear to develop through the thickness. Surface-to-surface ties are used to connect the parts together.

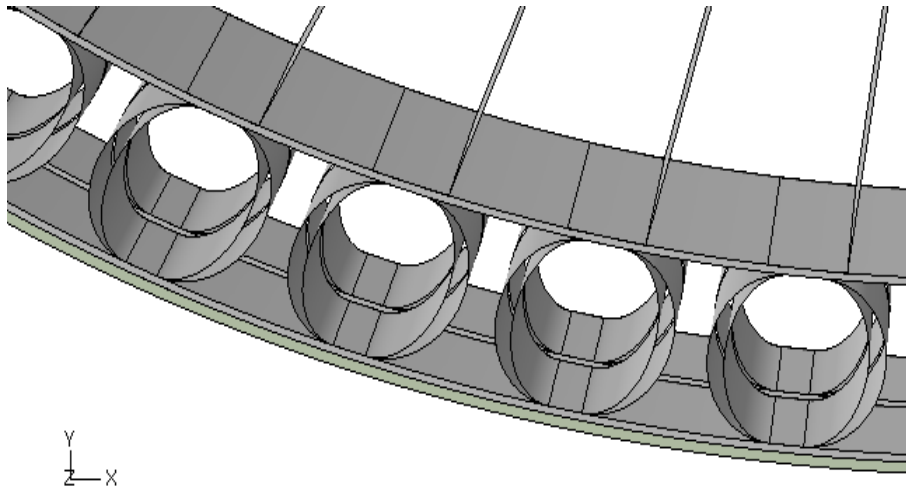


Figure 3.8 Shear Band

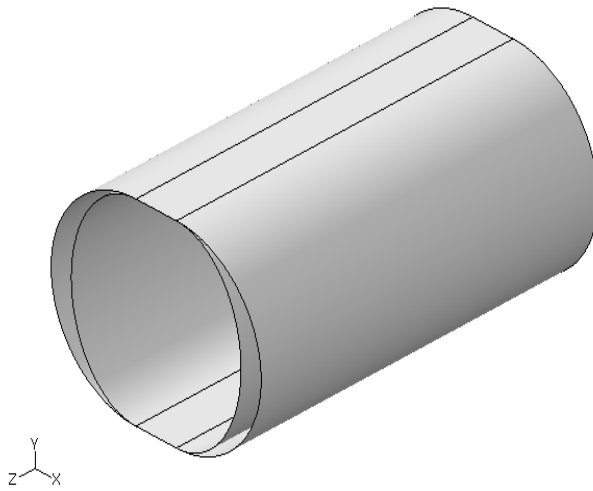


Figure 3.9 Shear Band Cylinder

3.3.3 Element Selection

Multiple types of elements are available in Abaqus™, each with its own strengths and limitations. The properties of each element type are discussed below. In both the models discussed above, M3D4R elements were used for the spokes and S4R elements were used for the springboards and cylinders. The two models vary in the way that they represent the inner and outer rings. The elements that were tested on the inner and outer rings are indicated with an asterisk.

*S4R (shell) – The default element for shell sections. This four-noded doubly curved shell element uses reduced integration and includes displacement and rotational degrees of freedom. S4R elements are suitable for both thick and thin shells. They account for finite membrane strains, shear flexibility, and thickness change. The formulation reflects Mindlin shell theory for thick shells and collapses to Kirchoff Theory as the shell thickness decreases.

*S4 (shell) – Similar to S4R except full integration is used to compute the stiffness matrix.

M3D4R (shell) – Membrane elements support only in-plane loads and have no bending stiffness.

*C3D8R (solid) – The default element for solid sections. This “brick” element has 8 nodes and has only displacement degrees of freedom. It also uses reduced integration.

*C3D8I (solid) – This “incompatible mode” element is like C3D8R, but it has 13 additional internal degrees of freedom which prevent the element from being overly stiff in bending. Full integration is used in formulating the stiffness matrix

*SC8R (solid) – The continuum shell family uses first-order composite theory. Unlike conventional shells, they can be stacked. Unlike continuum elements, they are formulated to model shell behavior without requiring multiple layers. Continuum shells allow finite membrane deformation, transverse shear deformation, and thickness change.

To test each element type, a wheel was loaded on a rigid surface by applying lunar gravity (1.600 m/s^2) to the wheel mass as well as the 1500 kg point mass at the center of the hub. The shell model was used for the shell elements and the solid-shell model was used for the solid elements. The wheel models are not identical, so direct comparison of deflections is not appropriate. In a first-order analysis of the terrestrial Tweel™, the predicted pressure distribution is uniform from front to back and side to side [6]. Testing of the prototype lunar Tweel™ showed that the pressure is highest near the edges of contact and lowest beneath the center cylinder. Early numerical analysis have indicated distinct pressure spikes beneath each cylinder, with the outermost cylinders having the highest peaks [17], but the sharp peaks were not observed in the experiment. The goal is to find out which, if any, of the element types show potential to predict the pressure distribution that has been measured. The solid elements were tested using one and two elements through the thickness of the ring. The first trials were run using a very coarse mesh. The pressure profiles are shown in Figures 3.10-3.17. The plane of symmetry is at the top of each image.

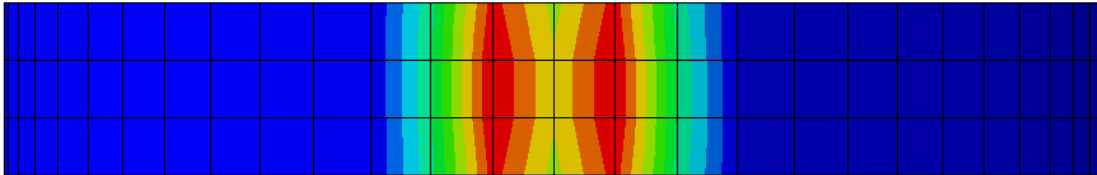
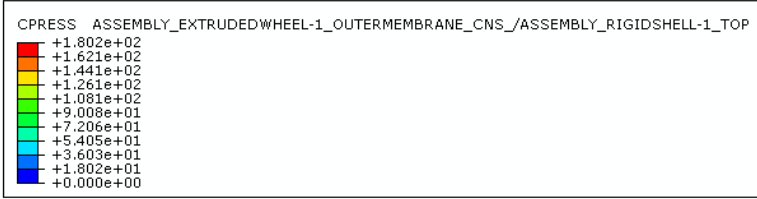


Figure 3.10 Contact Pressure - S4R Elements

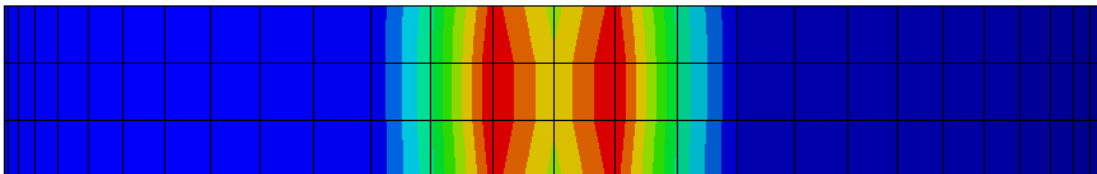
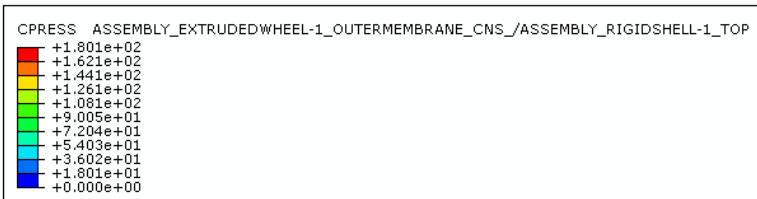


Figure 3.11 Contact Pressure - S4 Elements

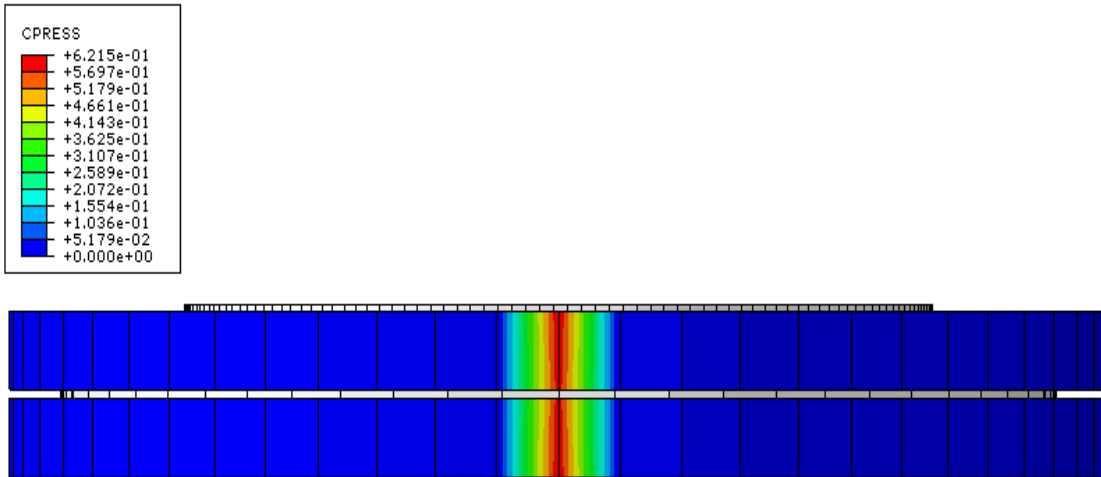


Figure 3.12 Contact Pressure - C3D8R Elements, 1 Element Thick

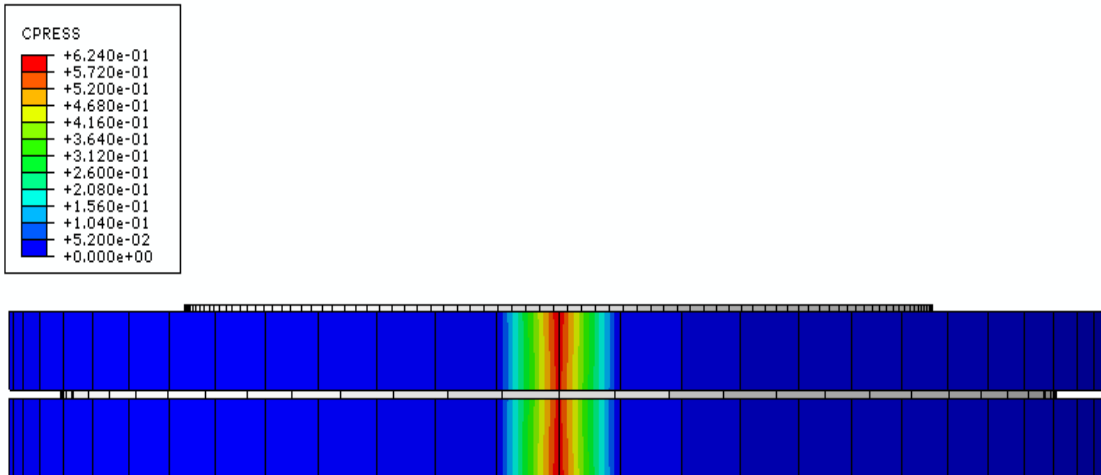


Figure 3.13 Contact Pressure - C3D8R Elements, 2 Elements Thick

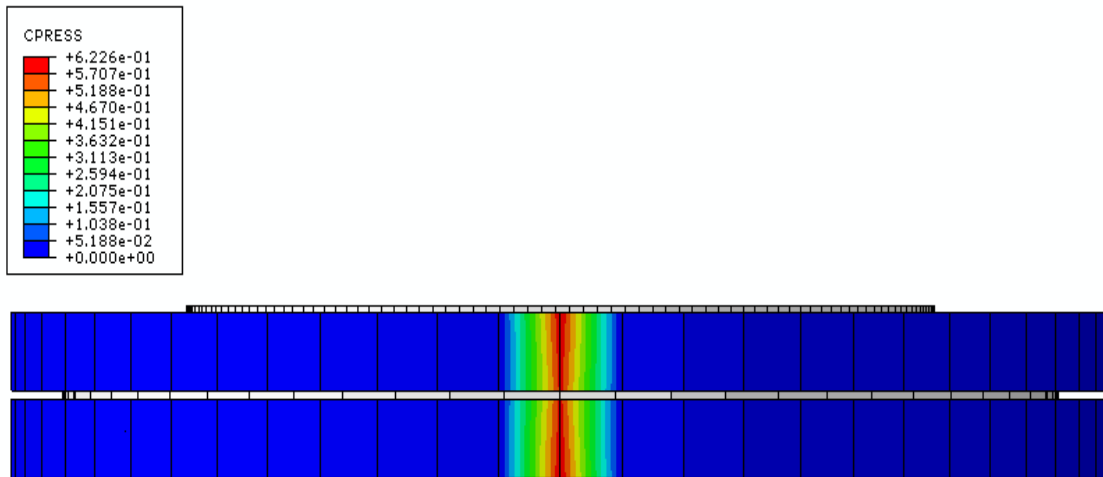


Figure 3.14 Contact Pressure - C3D8I Elements, 1 Element Thick

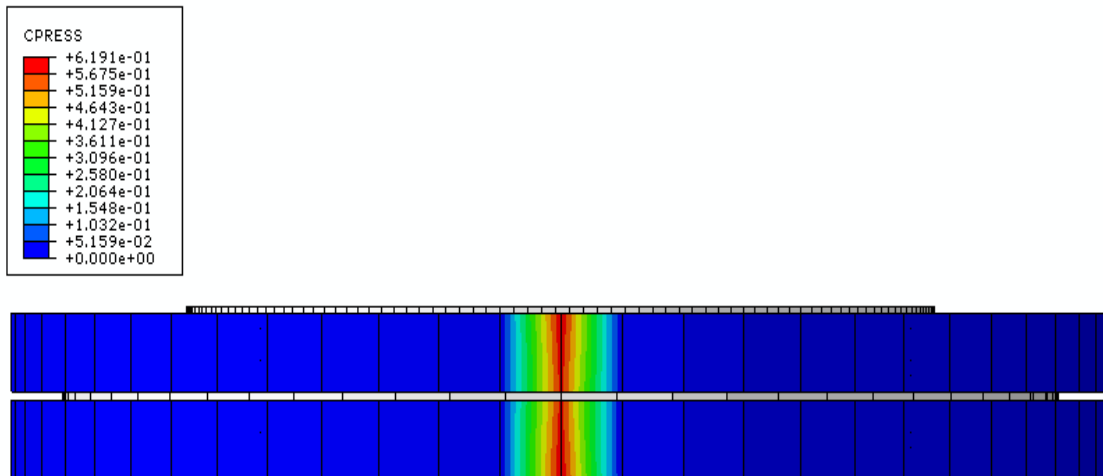


Figure 3.15 Contact Pressure - C3D8I Elements, 2 Elements Thick

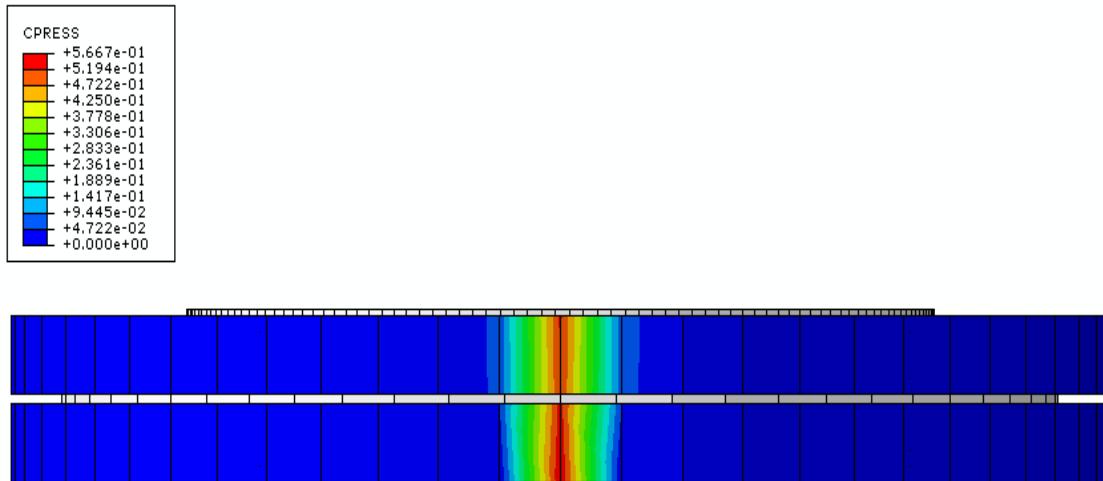


Figure 3.16 Contact Pressure - SC8R Elements, 1 Element Thick

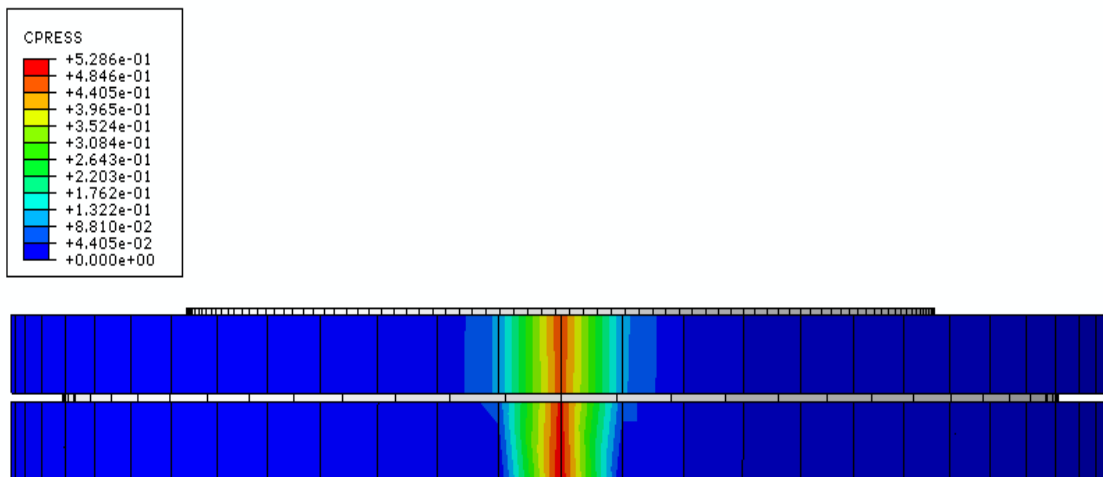


Figure 3.17 Contact Pressure - SC8R Elements, 2 Elements Thick

The computational times for each simulation are shown in Table 3.2. Each job was run on two nodes. For the solid model, default mesh settings were accepted for each

part, which resulted in a coarse mesh for the large parts and a more moderate mesh for the smaller parts like the cylinders. One difficulty with the shell model is that because it is all one part, the element length in the axial direction must be the same throughout the wheel. Working with the mesh is not as straightforward. In this case, the default mesh was very fine, with over 50,000 elements. To make a fair comparison, the shell model was remeshed to have similarly sized elements on the outer ring as the shell-solid model.

Table 3.2 Element Types

Element type	Wheel Model Used	Elements through thickness	Elements	Wall time (hh:mm:ss)	Cylinders in Contact with ground	Wheel Deflection (mm)
S4	Shell	1	7047	0:33:20	-13.13	-13.13
S4R	Shell	1	7047	0:28:00	-13.33	-13.33
C3D8I	Shell-Solid	1	23307	3:16:33	3	-7.47
C3D8I	Shell-Solid	2	23587	3:15:05	3	-7.59
C3D8R	Shell-Solid	1	23307	3:19:26	1	-6.21
C3D8R	Shell-Solid	2	23587	3:20:25	1	-6.03
SC8R	Shell-Solid	1	23307	3:09:06	3	-7.82
SC8R	Shell-Solid	2	23587	3:57:10	3	-7.87

For the 2400 N load used, the wheel deflection should be between 12 and 13 mm. The wheels have not yet been calibrated, but it is clear that the shell model is already closer to that target. The pressure profiles looked similar for all the solid elements, but the C3D8R elements were overly stiff. The Abaqus Documentation suggests that at least 4 of these elements should be used through the thickness of a thick shell part. For a large thin ring like the one studied here, this requires an impractical number of elements and an

unfeasibly small stable time step, so C3D8R elements were eliminated from further consideration.

The C3D8I elements are less stiff than the C3D8R elements, but not as flexible as the SC8R elements. The SC8R elements are selected for further refinement because they can capture shell behavior with only one layer and are marginally less computationally expensive. All models except the C3D8R models have 3 cylinders in contact with the ground. Only one cylinder contacts the ground in the overly stiff C3D8R models.

A second round of simulations was completed for the S4R and SC8R elements using a refined mesh. The pressure profiles as are shown in Figures 3.18-3.219.

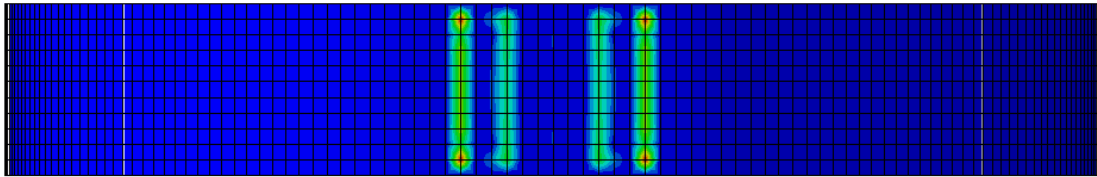
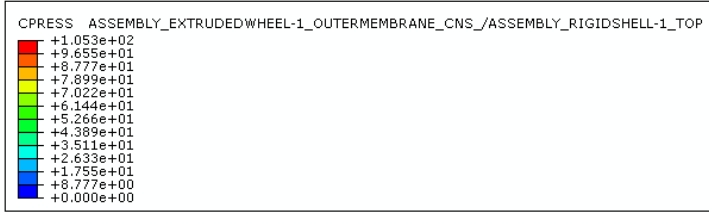


Figure 3.18 S4R Elements, Refined Mesh

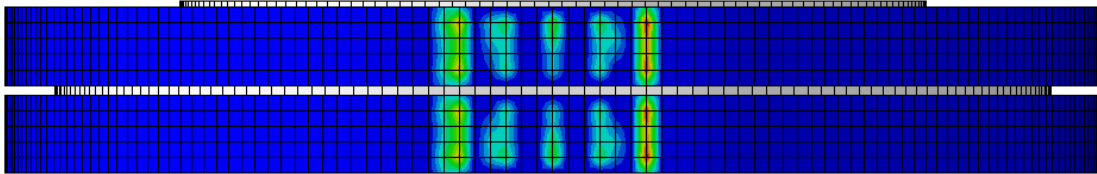
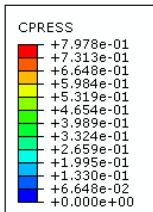


Figure 3.19 SC8R Elements, Refined Mesh

Even with a refined mesh, neither of the selected element types gave the smooth pressure profile observed in experiments. Computation times are listed in Table 3.3. The SC8R elements did not show any advantage over the S4R elements in predicting the

pressure profile, so the shell model with S4R elements was chosen for the rest of the study due to its computational efficiency.

Table 3.3 Computation Times of Refined Wheel Meshes

Element type	Elements	Wall time	Wheel Deflection (mm)
S4R	30800	3:36:41	-11.49
SC8R	27427	5:39:58	-13.79

3.4 Contact

In all of the above simulations, a hard contact formulation was used which resulted in pressure spikes. In order to smooth out the pressure profile, a softened contact formulation is examined in this section. In the hard contact formulation, no penetration is allowed. The Lagrange multiplier method of enforcement allows a virtually unlimited amount of pressure to build up between the wheel and the rigid surface. In the following simulations, a linear pressure-overclosure relationship is used. The constant k is the slope of the pressure-overclosure curve. For example, when $k = 10$, 10 MPa is added for every mm of overclosure (penetration). The pressure profiles were examined for three values of k : 10, 100, and 1000 (Figures 3.22-3.24).

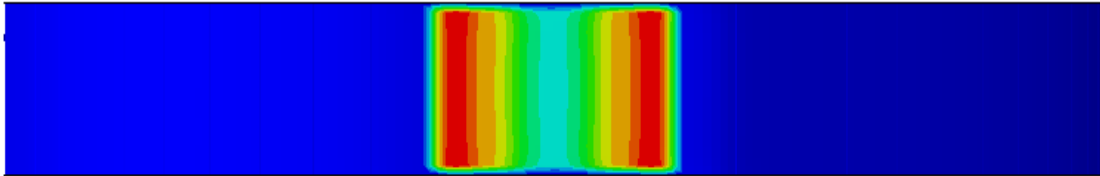
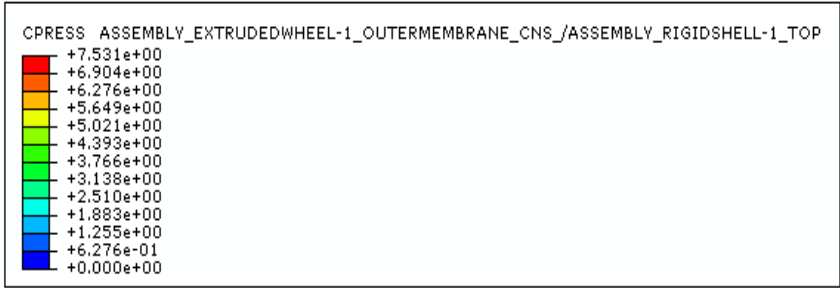


Figure 3.20 Pressure Distribution for $k=10$ MPa/mm

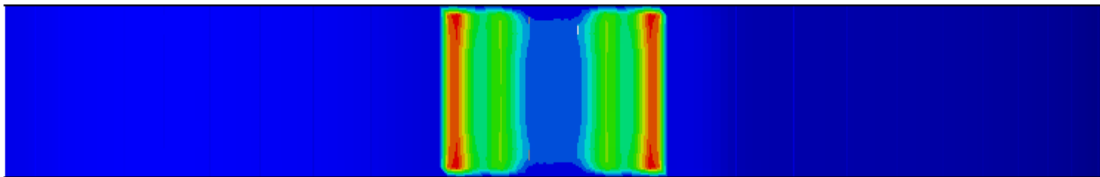
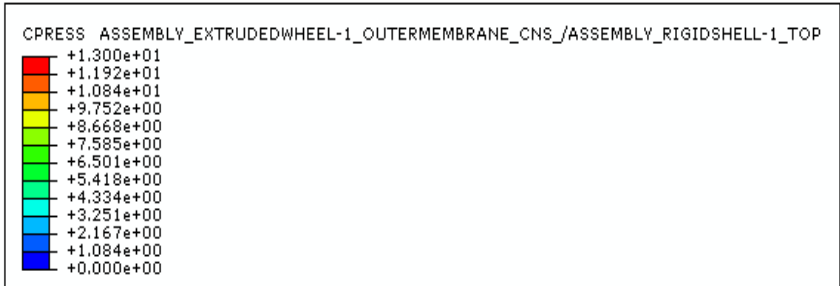


Figure 3.21 Pressure Distribution for $k=100$ MPa/mm

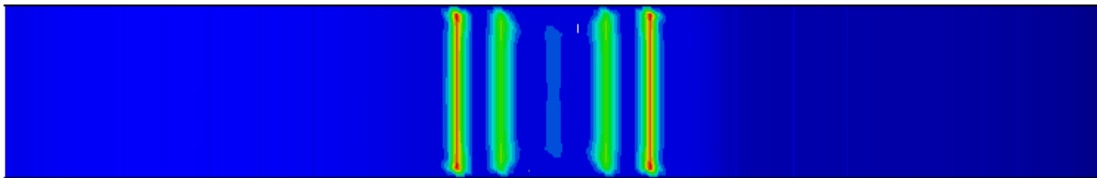
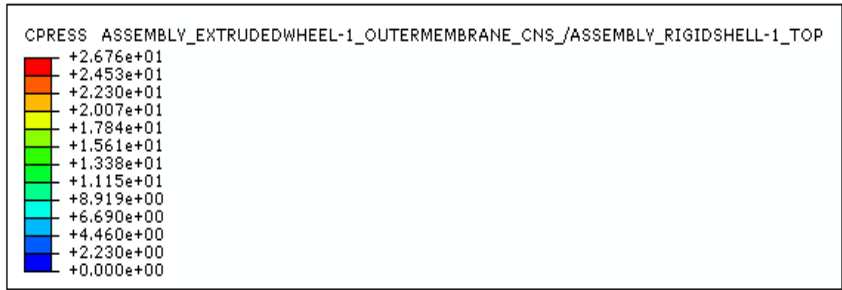


Figure 3.22 Pressure Distribution for $k=1000$ MPa/mm

With a stiff pressure overclosure relationship ($k=1000$), pressure spikes are still observed below each cylinder. The pressure distributions for $k = 10$ and $k = 100$ are much smoother. However, Table 3.4 shows that setting the contact stiffness to $k = 10$ changes the deflection of the wheel by more than a half a millimeter. The contact stiffness $k = 100$ MPa/mm is selected for the model.

Table 3.4 Effect of Contact Stiffness on Wheel Deflection

Contact Stiffness (MPa/mm)	Elements	Wall time	Wheel Deflection (mm)
10	37314	5:32:11	-13.00
100	37314	5:35:24	-12.44
1000	37314	5:29:10	-12.34

3.5 Wheel Mesh Refinement

Three mesh sizes were used to check for convergence. The driving factor in simulation time for the wheel is not the number of elements, but the size of the smallest elements. The delicate wheel geometry has features that require small elements, and small elements have small stable time increments. As shown in Table 3.5, setting the element size to 3 mm x 3 mm made almost no change in the wheel deflection, but significantly increased the computation time. The coarse mesh allowed a significantly larger time increment; it reduced the wall time by over 90% yet still calculated the wheel deflection within a half a millimeter of the fine mesh. Therefore, an element length of 12 mm was selected.

Table 3.5 Wheel Mesh Refinement

Mesh	Element Size on Outer Ring (mm)	Elements	Wall time	Wheel Deflection (mm)
Coarse	12	16641	1:41:44	-12.73
Medium	6	37314	5:35:24	-12.44
Fine	3	89133	24:00:15	-12.33

3.6 Calibration

To ensure that the model is representative of the prototype wheel, parameters such as spoke thicknesses were adjusted until the load-deflection curve matched experimental data. The wheel was placed on a rigid plate and gravity was applied slowly over 12 seconds to the wheel, including a 1500 kg point mass at the center of the hub. Lunar gravity ($g = 1.6 \text{ m/s}^2$), which is about 1/6 of earth's gravity is used in the simulation. A

1500 kg lunar load is equivalent by weight to a 250 kg load on earth. The configuration of this simulation is as shown in Figure 3.5 with a cylinder set centered at the contact point. The final result is shown in Figure 3.23. The load-deflection curve of the finite element model wheel (blue) is plotted over the load-deflection curves obtained experimentally on the prototype wheel at the Michelin America Research Center (gray). Multiple experimental curves represent results for the same wheel rotated 0, 90, 180, and 270 degrees from two symmetric conditions (a cylinder on the centerline and a space between cylinders at the centerline). The finite element line follows the high side of the hysteresis loop. The experimental hysteresis could be due to friction at the connection points, or friction and damping internal to the material, neither of which is included in the finite element model. Internal friction and damping lead to viscoelastic, or in this case anelastic behavior. Anelastic materials are a subset of viscoelastic materials in which the strain lags the stress but the equilibrium configuration is ultimately recovered after the removal of load. Overall, the numerical results align very nicely with the experimental results.

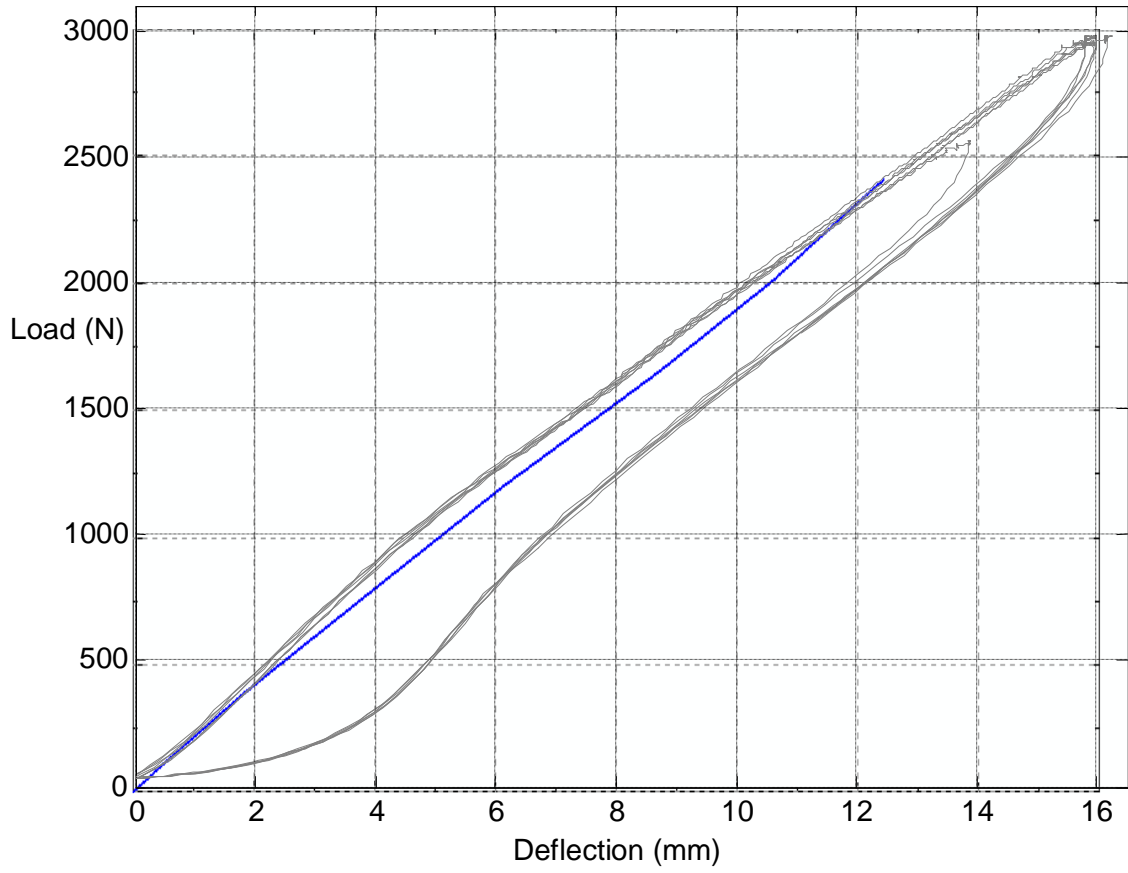


Figure 3.23 Experimental (gray) and Numerical (blue) Load-Deflection Curves

3.7 Summary

After running multiple trials to select the element types, contact parameters, mesh refinement, and calibration the final wheel model is the shell model with reduced integration conventional shell elements. This was counter to the hypothesis that modeling the inner and outer rings as solid parts could add accuracy. It is still possible that solid elements could produce better results with further refinement, but within the resource constraints of this study, refining the solid elements to the point they would produce better results was not feasible. With appropriate contact conditions, the shell model provides reasonable results in a much shorter time. Soft contact with a stiffness of 100 MPa/mm is used and 12 mm x 12 mm was found to be a suitable element size for the outer ring. Results from the final model are plotted in Figure 3.24 through Figure 3.26 below. Table 3.6 summarizes the material properties and element types used for each component of the wheel

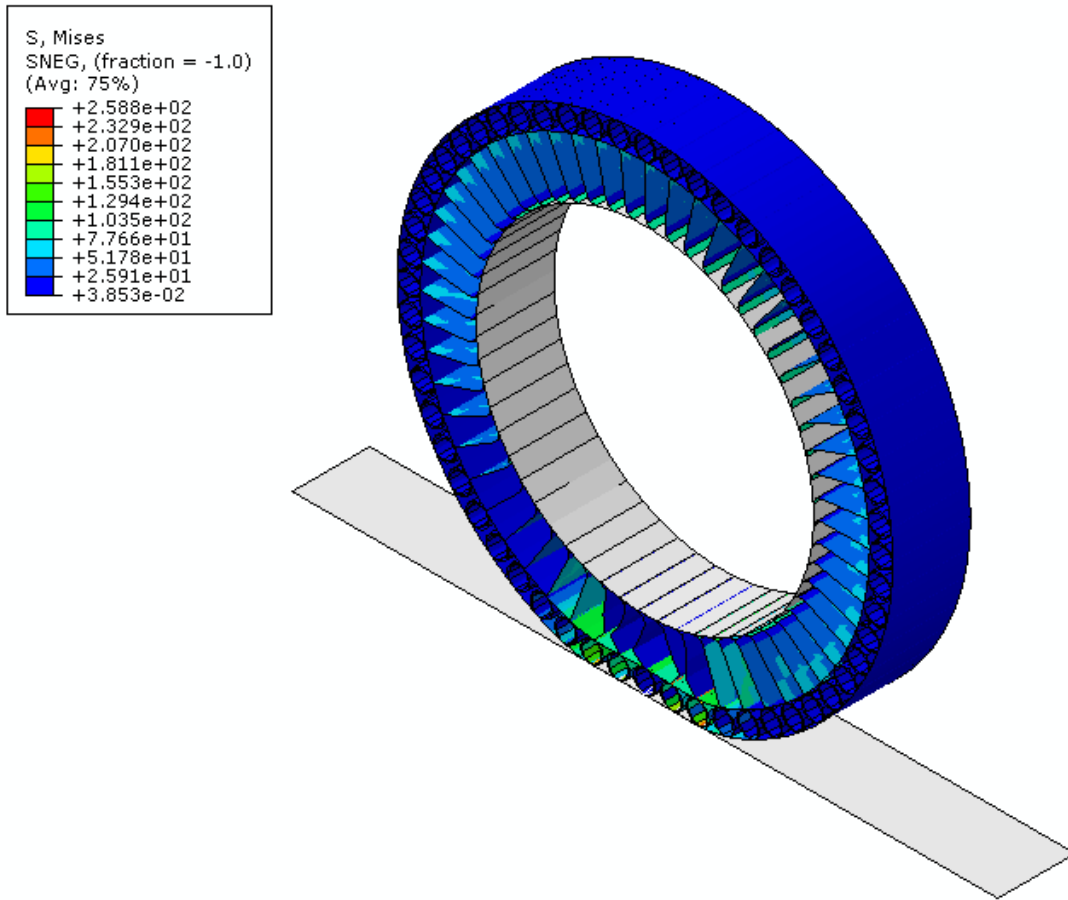


Figure 3.24 Final Wheel Model Showing von Mises Stress

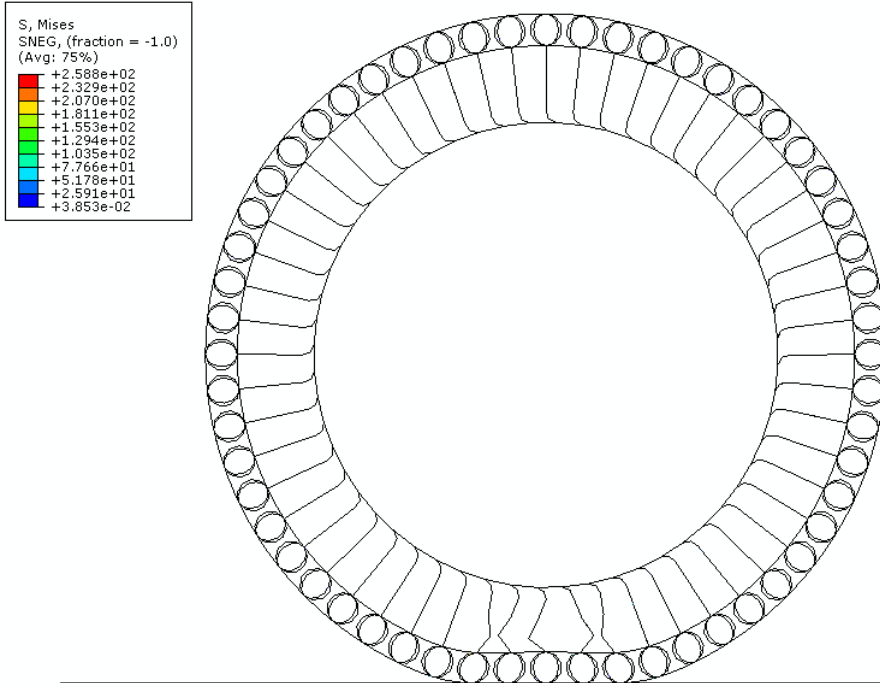


Figure 3.25 Side View of Final Wheel Model

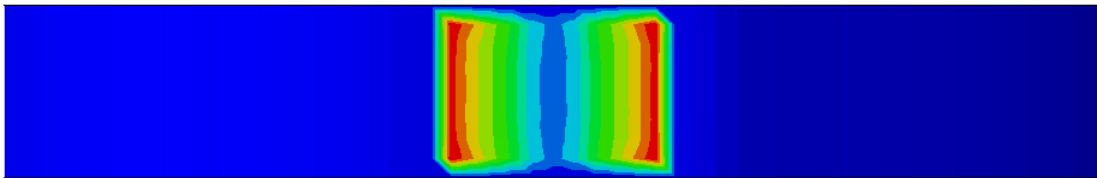
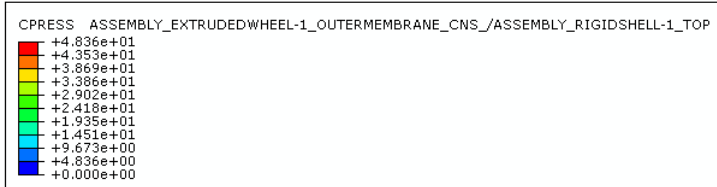


Figure 3.26 Final Wheel Model Contact Pressure on Rigid Surface

Table 3.6 Materials and Element Types by Section

Section	Material	Young's Modulus E (MPa)	Poisson's Ratio, ν	Thickness t (mm)	Element Type
Hub	NA	NA	NA	1	R3D4 (Rigid)
Springboard (Curved Spoke-to-Hub Connector)	Glass Composite	39969	0.29	1.5	S4R
Spoke	Glass Composite	39969	0.29	0.1	M3D4R
Inner Ring	Glass Composite	39969	0.29	1.5	S4R
Cylinders	Glass Composite	39969	0.29	0.7	S4R
Outer Ring	Glass Composite	39969	0.29	1.5	S4R

4. SOIL MODEL

In the following sections this chapter will address Research Questions 2 and 3. Question 2, “Can a constitutive model that captures experimentally observed soil behaviors such as side berms and rutting be implemented in the selected finite element code?” is discussed in sections 4.1-4.3. Question 3, “How can the finite element model parameters (such as boundary conditions and soil bed dimensions) be systematically selected in order to improve efficiency and maintain accuracy?” is answered in sections 4.4-4.6.

4.1 Material Model Selection

A variety of material models are available for modeling soil, several of which are built into Abaqus™. The advantages and disadvantages of each are summarized in Table 4.1. The table represents all the constitutive theories built into Abaqus™ that are relevant to soil modeling, hence they all meet the first constraint, that they are available in the selected code, Abaqus™. The second constraint is that the model is available in Abaqus/Explicit™ so that dynamic effects can be captured. As mentioned in Chapter 2, lunar soil is silty sand that exhibits frictional properties. Predicting frictional behavior requires a pressure dependent model. A model that uses non-associated flow is important for realistic dilatational behavior. Finally, a good soil model will account for plastic compaction because the mechanism by which the soil compresses changes with specific volume.

Table 4.1 Soil Model Properties

Soil Model	Constraint				
	Available in Abaqus	Available in Abaqus/Explicit	Pressure dependence	Non-associated flow	Plastic compaction/hardening
von Mises	Y	Y	N	N	N
Mohr-Coulomb	Y	N	Y	Y	N
Drucker-Prager	Y	Y	Y	Y	N
Drucker-Prager with Cap Plasticity	Y	Y	Y	Y	Y
Cam Clay (Critical State)	Y	N	Y	N	Y

The only material model that meets all the constraints is a Drucker-Prager Model with Cap Plasticity. Another advantage of this model is that it is possible to change the cross-section of the Drucker-Prager surface from a circle to a rounded triangle in order to nearly match experimental results from both triaxial compression and triaxial extension tests.

4.2 Soil Parameters

As discussed in Section 2.2, recommended values are available for the bulk density and the Mohr-Coulomb strength parameters of lunar soil. The soil is divided into three layers, representing the change in bulk density and shear strength with depth. For the third layer, equation (2-13) is used to compute an average value and the strength properties are continued from the second layer. Each layer has a modified Drucker-Prager material model with cap plasticity. Table 4.2 summarizes the properties used in

each layer in terms of both Mohr-Coulomb and corresponding Drucker-Prager parameters (according to equations (2-3) and(2-4)). The Mohr-Coulomb parameters are the recommended values from the Lunar Sourcebook [31].

Table 4.2 Bulk Density and Shear Strength Parameters of Soil Model Layers

Depth Range	Bulk Density ρ [31]	Mohr-Coulomb Cohesion c [31]	Mohr-Coulomb Friction Angle ϕ [31]	Inscribed Drucker-Prager Cohesion d equation (2-4)	Inscribed Drucker-Prager Friction Angle, β equation (2-3)
(cm)	(g/cm ³)	(kPa)	(degrees)	(kPa)	(degrees)
0-30	1.58	0.90	46	1.01	49.2
30-60	1.74	3.00	54	2.78	51.9
> 60	1.80	3.00	54	2.78	51.9

The Cap Plasticity model requires elastic properties to be defined, although in this case they will have little impact on the simulated outcomes. Data on the elastic properties of lunar soil are lacking, and a wide range of values have been reported for lunar soil simulant [29]. For simplicity, all elastic and cap plasticity parameters will be based on Ottawa sand [87]. Ottawa sand has strength properties similar to lunar soil and elastic properties within the range reported for lunar soil simulant. Table 4.3 identifies these material properties which are consistent for all layers.

Table 4.3 Soil Model Properties [87]

Property		Value
Elastic	Young's Modulus (MPa)	182
	Poisson's Ratio	0.28
Cap Plasticity	Cap Eccentricity Parameter	0.4
	Initial Cap Yield Surface Position	0
	Transition Surface Radius Parameter	0.05
	Flow Stress Ratio (K)	1

The cap hardening curve is tabulated according to (2-8) using the GRC-1 values of $C_c = 0.02$ and $C_s = 0.005$ with the initial void ratio equal to 0.5316 at $p = 6.9$ kPa [30].

Figure 2.7 is reproduced here for convenience.

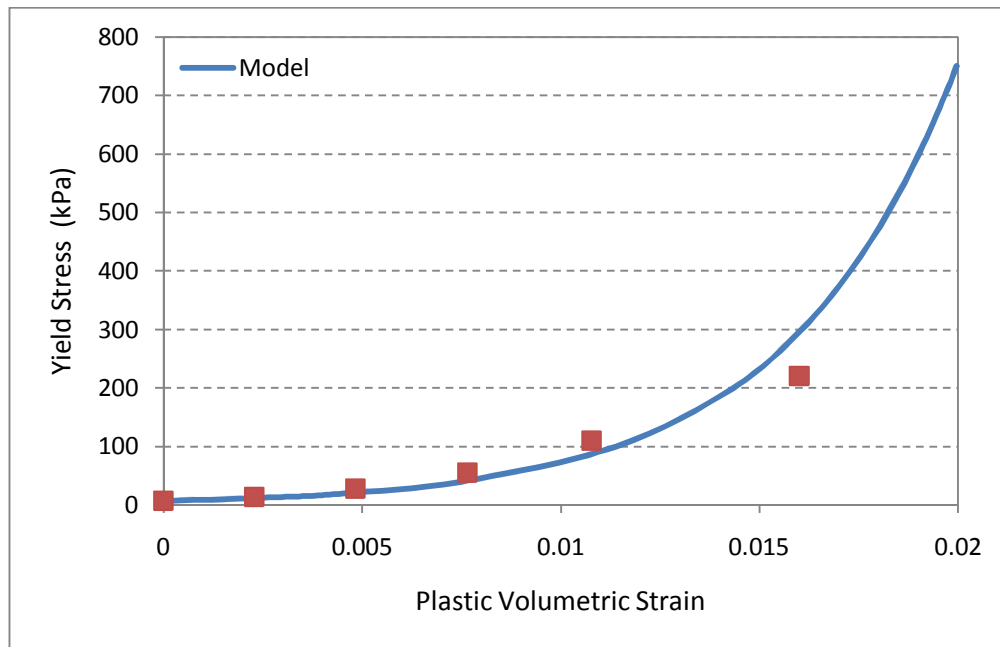


Figure 2.7 (repeated) Cap Hardening of GRC-1 (linear scale)

4.3 Reduction of Edge Effects

A sufficient amount of sand must be modeled so that edge effects are negligible. This size is determined by simulating a simple rigid wheel on a mass of sand and then iteratively adding and removing material until the remaining mass captures all the significant movement normal to the edges, without modeling unnecessary material. A rigid wheel is used to capture the most extreme soil deformation. Additionally, it saves computation time. For computational efficiency, a symmetry condition is set up at the center of the wheel in the xy-plane (normal to the wheel axis); the nodes initially in the plane are forced to remain in the plane throughout the simulation. The bottom and three remaining sides are constrained in all directions. Early trials used a no-slip condition between the rigid wheel and soil, but it was found that this unrealistic condition created convergence problems at the mesh refinement stage. The trials presented below define interaction between the wheel and soil as a hard contact with a friction coefficient equal to the tangent of the friction angle of the soil. Contact is defined between the outer surface of the wheel and a 200 mm strip along the top of the sand, adjacent to the symmetry surface.

Initially, a separate step was included to allow the soil to settle before the wheel load was applied; however, the settling of the soil under the lunar gravity (1.6 m/s^2) was only about 6 microns. Because the goal of this research is to be within the millimeter range of accuracy, this step was eliminated and gravity was applied to the wheel and soil simultaneously. First, gravity is ramped up smoothly over 10 seconds and then held for 2 seconds before angular velocity of the hub is added. The angular velocity smoothly

ramps from zero to 0.8 rad/sec (equivalent to 1 kph on a rigid surface with no slip) over a twenty second period. The smooth angular velocity ramp is a fifth-order polynomial, which makes the angular acceleration a fourth-order polynomial with a peak value of 1.88 times the average angular acceleration. In this case the peak equivalent horizontal acceleration on a rigid surface with no slip was 26 mm/s^2 .

Two methods were considered for selecting the size of the soil bed. Both started with the same initial size of $1.5d$ in width, depth, and distance ahead of and behind the wheel, based on a simulation reported by Hambleton [88]. The first method was sequential, varying one dimension at a time and using the horizontal and vertical displacement of the wheel as an indicator. The second method was holistic, looking at all the dimensions at once and this approach proved to be simpler, quicker, and more reliable.

4.3.1 Sequential Method

In the sequential method, one dimension is varied at a time and the optimal length is selected and used for all successive iterations. Holding all other dimensions constant, the width of the sample was varied from $1d$ to $2.5d$ in increments of $0.5d$. The percent difference in each indicator was checked against the $2.5d$ wide results to check for accuracy, as shown in Table 4.4. To check for mesh dependence, this process was repeated using roughly twice as many elements (mesh size 25.4 mm). A 0.5% tolerance was set for the vertical and horizontal displacement after rolling. Selecting the vertical depth proceeded in a similar manner. However, the trends were not consistent, possibly due to the rearrangement of the nodes that must happen every time a dimension is

changed. These criteria were sufficient for selecting a width and a depth, but showed no consistent trend in the dimension behind the wheel, so a third criterion had to be added. A 1% tolerance was set for the sinkage due to gravity alone. The gravity tolerance was set larger because there seemed to be more variability in this measure.

Several variations of this method were also tried, but there was too much noise in the data to clearly see how large each dimension needed to be. The results are very sensitive to the tolerance values selected. Additionally, this method requires many simulations to be run which makes using a fine mesh impractical and one dimension must be determined before the next set of simulations can be started, which makes it time consuming.

Table 4.4 Sequential Sizing Method

Width	Soil Dimensions				Soil Element Length = 32 mm				Soil Element Length = 25.4 mm			
	Width	Vertical depth	Behind wheel	Ahead of wheel	Elements	% Change due to gravity from reference (max 1%)	% Change Horiz. from reference (max 0.5%)	% Change Vert. from reference (max 0.5%)	Elements	% Change due to gravity from reference (max 1%)	% Change Horiz. from reference (max 0.5%)	% Change Vert. from reference (max 0.5%)
	1750	1050	1050	3850	269280	Reference			559314	Reference		
	1400	1050	1050	3850	215424	-0.30%	-0.01%	-0.03%	445830	-0.63%	0.02%	-0.09%
	1050	1050	1050	3850	161568	-0.66%	-0.02%	-0.03%	332346	-0.19%	0.03%	-0.20%
	700	1050	1050	3850	107712	-1.19%	-0.25%	2.26%	226968	0.04%	-0.11%	1.19%

Depth	Soil Dimensions				Soil Element Length = 32 mm				Soil Element Length = 25.4 mm			
	Width	Vertical depth	Behind wheel	Ahead of wheel	Elements	% Change due to gravity from reference (max 1%)	% Change Horiz. from reference (max 0.5%)	% Change Vert. from reference (max 0.5%)	Elements	% Change due to gravity from reference (max 1%)	% Change Horiz. from reference (max 0.5%)	% Change Vert. from reference (max 0.5%)
	1050	1750	1050	3850	269280	Reference			545997	Reference		
	1050	1400	1050	3850	215424	-0.11%	0.01%	-0.01%	435215	0.42%	0.00%	0.01%
	1050	1050	1050	3850	161568	0.53%	-0.01%	-0.06%	332346	0.49%	0.00%	-0.07%
	1050	700	1050	3850	107712	0.72%	0.00%	-0.06%	221564	0.33%	-0.02%	-0.04%
	1050	350	1050	3850	107712	-0.95%	-0.04%	-0.35%	110782	-0.72%	-0.03%	-0.94%

4.3.2 Holistic Method

A more efficient method for determining the size of the soil required was developed as outlined below:

- 1) Using the initial dimensions described above and an average element length of 25.4 mm (approximately $0.04d$), the magnitude of the displacement was plotted with the lower limit set to 0.1 mm as shown in Figure 4.1

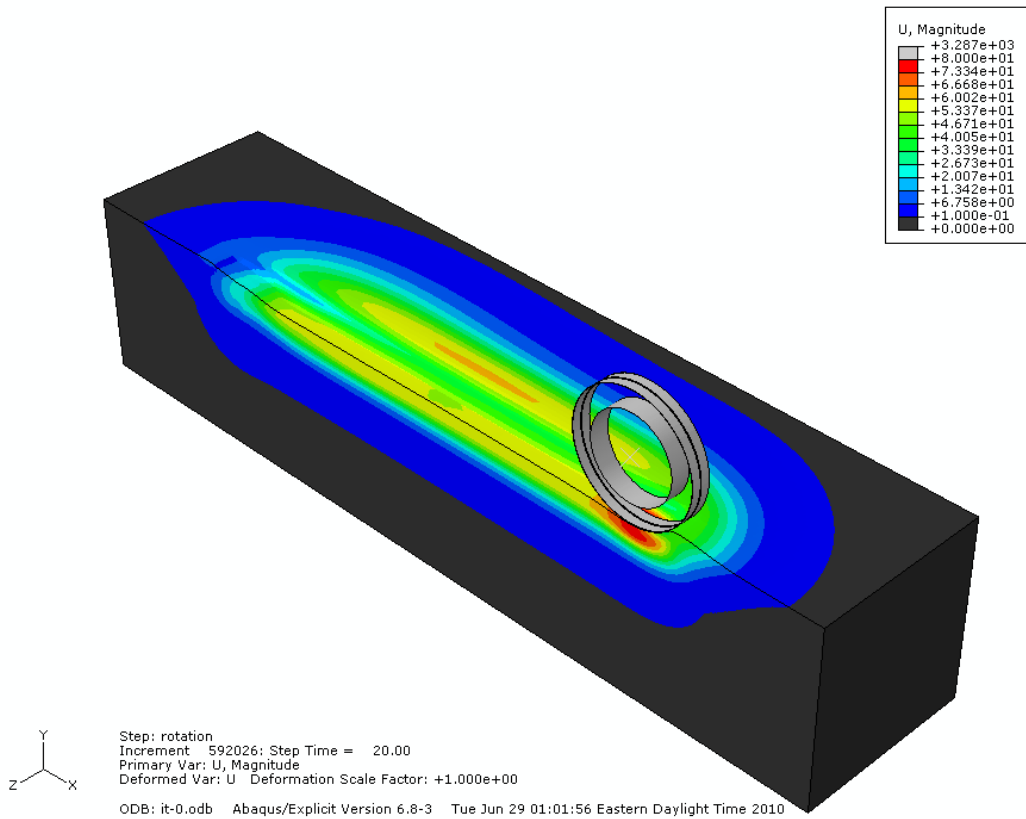


Figure 4.1 Initial Size

2) Each edge was examined to determine if the displacement was greater than 0.1 mm within $0.5d$ (≈ 350 mm) from the edge. The view cut tool is useful for this step. In all dimensions except the depth, there was displacement greater than 0.1 mm within 350 mm from the edge, so the dimensions were increased by $0.5 d$ and the simulation was repeated.

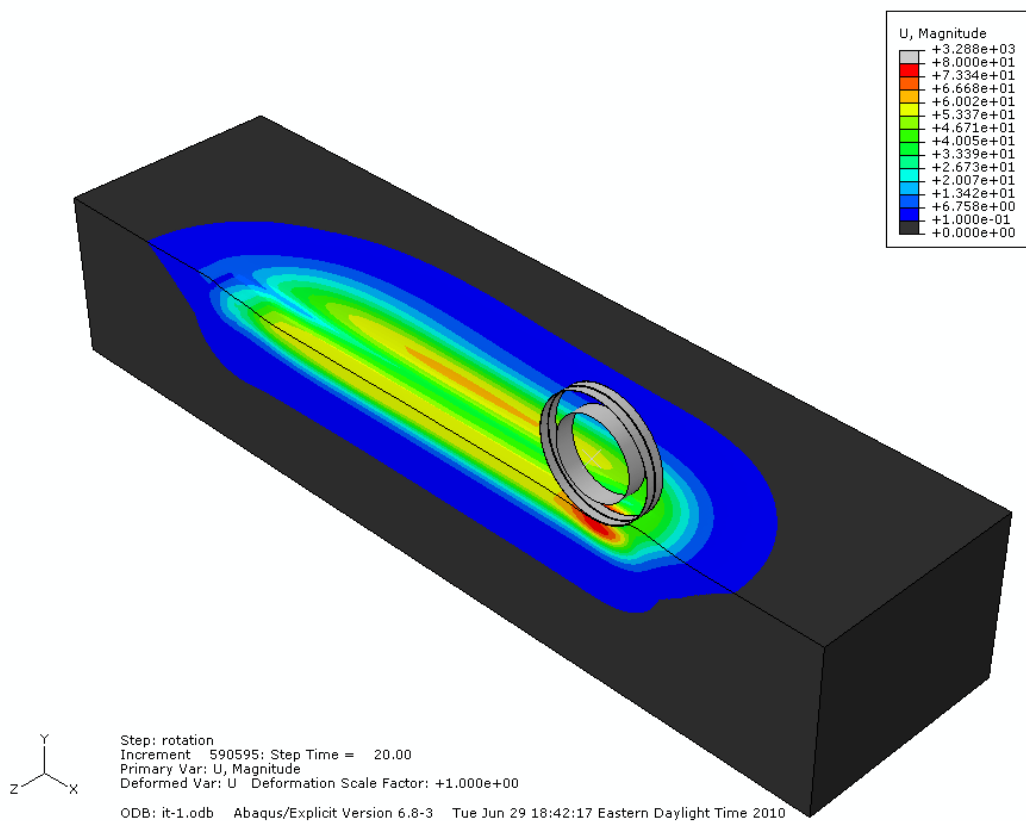


Figure 4.2 Iteration 1 – Increased Size

3) When the magnitude of displacement was less than 0.1 within $0.5d$ of all edges (as in Figure 4.2), the final dimensions were determined by removing regions of soil that had displacements less than 0.1, again using the view cut tool.

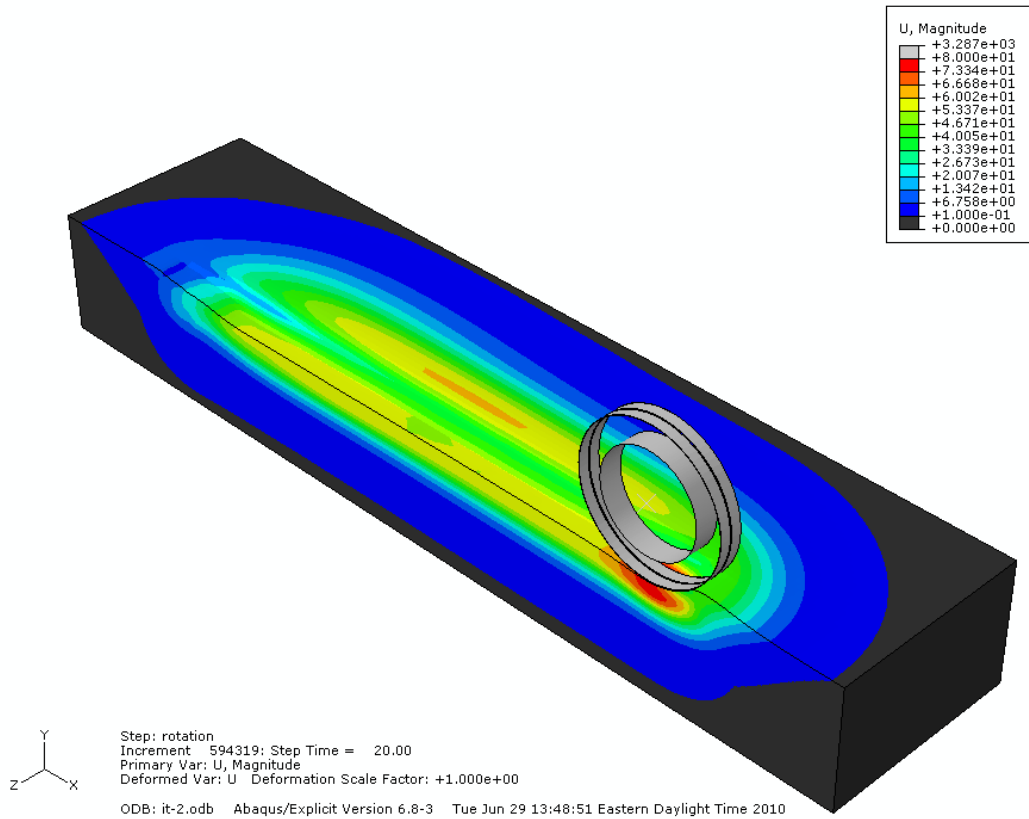


Figure 4.3 Iteration 2 - Decreased Size

- 4) Wheel displacements were compared to ensure that accuracy was maintained. The final dimensions are shown in Figure 4.3 and summarized in Table 4.5. The wheel displacements calculated from the final model are all within 0.5% of the displacements calculated from the oversized model.

Table 4.5 Summary of Holistic Sizing Method

	Width (mm)	Vertical Depth (mm)	Behind Wheel (mm)	Ahead of Wheel (mm)	Elements	Disp. due to Gravity (mm)	Horiz. Disp. (mm)	Vert. Disp. (mm)
Initial Size	1050	1050	1050	3850	332346	-27.64	2752	-61.16
Iteration 1: Increased Size (% Change from above)	1750	1050	1750	4550	508200	-27.96 (1.15%)	2753 (0.03%)	-61.24 (0.14%)
Iteration 2: Decreased Size (% Change from above)	1000	600	800	3700	165672	-27.85 (-0.38%)	2753 (-0.02%)	-61.02 (-0.36%)

This more holistic method was much quicker than running multiple simulations to determine each dimension. Because the oversized model did not show any displacements near the edges, it is reasonable to use this model as a reference and then move the boundaries as close in as possible without changing the soil displacement by more than 0.1 mm. Figure 4.4 below shows that altering the displacement limit by a factor of 10 from 0.05 mm to 0.5 mm makes little difference in the outcome.

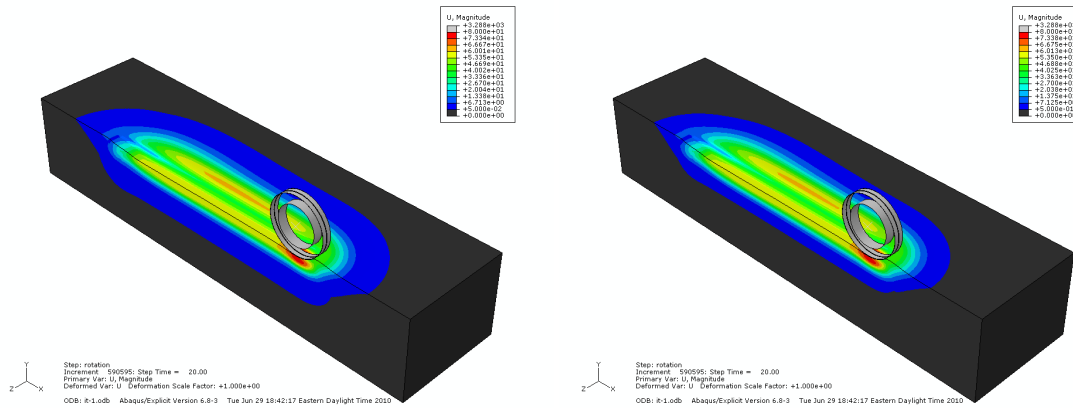


Figure 4.4 Comparison of Tolerance Limits: 0.05 mm (left) and 0.5 mm (right)

To ensure that the results are not mesh dependent, the process was repeated with a coarser mesh. The coarse mesh ran in about half the time. The only difference in results is a slightly more conservative width dimension, shown in Table 4.6.

Table 4.6 Effect of Mesh Size on Holistic Method Results

Element size (mm)	No. of elements in initial trial	Final dimensions determined by holistic method			
		Width	Vertical depth	Behind wheel	Ahead of wheel
25.4	332346	1000	600	800	3700
32	161568	1100	600	800	3700

4.4 Boundary Conditions

Far field stresses and displacements are expected to be zero; therefore if the soil bed modeled is large enough, the far field boundary conditions should not have a significant effect on the simulation. In reality, the boundaries would be subject to bearing pressure and friction from the sand around it. Numerically it is much more efficient to model the boundaries as either pinned or sliding conditions because friction requires

using a contact algorithm. At low shear stresses, a pinned condition acts similar to static friction. The difference is that in the case of static friction, once the shear force exceeds the normal force times the static friction coefficient, slip occurs and dynamic friction takes over. While it is expected that a pinned boundary condition is most realistic, if the boundaries are far enough away, they should have little effect. As shown in Table 4.7, this is indeed the case. Changing the boundary conditions at the sides to sliding constraints changes the results by less than two tenths of a millimeter. This is further confirmation that the selected dimensions are appropriate.

Table 4.7 Effect of Boundary Conditions

		Disp. due to gravity (mm)	Horizontal disp. (mm)	Vertical disp. (mm)
Boundary Condition	Pinned	-27.85	2752	-61.02
	Sliding	-27.71	2752	-61.09
Difference		-0.14	-0.13	0.07
% Difference		-0.51%	0.00%	0.11%

4.5 Friction Coefficient

Unless otherwise noted, the simulations in this work use a friction coefficient of 1.04 between the soil and the wheel. This is equivalent to the tangent of the friction angle of the soil. In other words, the friction between the wheel and soil is equal to the shear strength of the soil in the absence of any cohesion. This essentially assumes that a thin layer of sand is adhered to the tread. This variable is easily modifiable once a more reliable estimate of the coefficient of friction is known. However, as Table 4.8 shows,

the coefficient of friction does not have a remarkable impact on the final result, thus a rough estimate is sufficient.

Table 4.8 Effect of Friction Coefficient

		Displacement due to gravity (mm)	Horizontal displacement (mm)	Vertical displacement (mm)
Friction Coefficient	$\mu = 1.04$	-27.85	2752.23	-61.02
	$\mu = 0.5$	-27.48	2677.35	-61.81
Difference		0.37	-74.88	-0.79
% Difference		-1.34%	-2.72%	1.29%

4.6 Soil Mesh Refinement

With appropriate dimensions and boundary conditions in place, the model development can proceed with determining an appropriate mesh size. This is especially important in a three-dimensional simulation because cutting the element length in half increases the number of elements eight-fold. It is important that the elements be small enough that the solution is mesh-independent, but to reduce computation time, they should be as large as possible. The initial element length was 32 mm; approximately $0.05d$. To create a mesh with approximately twice as many elements, this length was multiplied by $2^{-1/3}$. The mesh size, number of elements, and key indicators are summarized in Table 4.9. For the mesh refinement simulations, the deformable wheel defined in Chapter 3 is used. The simulation with 25.4 mm elements takes 30% less time to run than the simulation with 20.2 mm elements, and the results are within 5% of the

finer mesh. For most studies, this is a reasonable amount of error. The 25.4 mm element size could be used for comparison studies to determine optimal values of wheel parameters and a finer mesh could be used for final verification. The remaining simulations in this document use the 25.4 mm mesh.

Table 4.9 Soil Mesh Refinement

Element size (mm)	Elements	Wall time	Horizontal disp. (mm)	Vertical disp.	Horizontal % change from reference	Vertical % change from reference
20.2	367950	15:37:22	2704	-71.19	reference	reference
25.4	190275	9:40:25	2719	-68.40	0.5%	-3.9%
32.0	91086	6:03:10	2702	-65.99	-0.1%	-7.3%

The selected model is shown in Figure 4.5 through Figure 4.9. In Figure 4.5, the soil deformation looks smooth and there is no displacement greater than 1 mm close to the edges, which indicate that the mesh is reasonably refined and the soil bed is large enough, respectively. The wheel shows only small deformation of the shear band, but it is enough that seven spokes collapse due to the weight (Figure 4.6). The rotation of the hub winds the spokes tight so that at full speed only six spokes have visibly started to collapse (Figure 4.7).

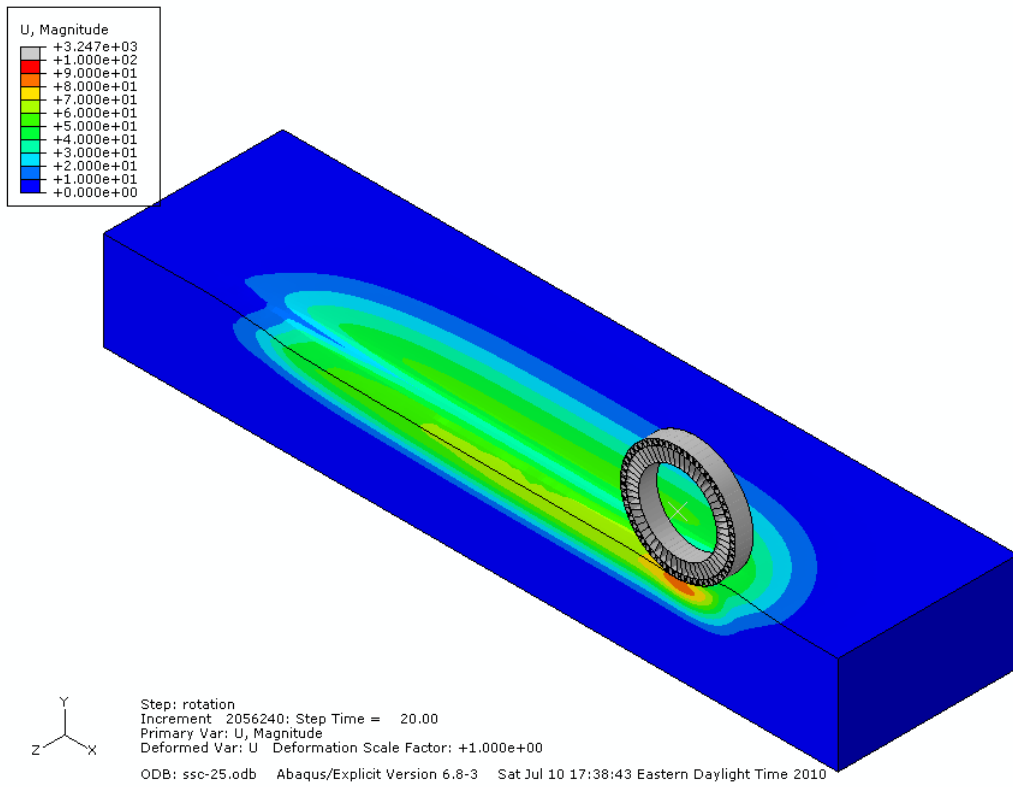


Figure 4.5 Results of Mesh Refinement

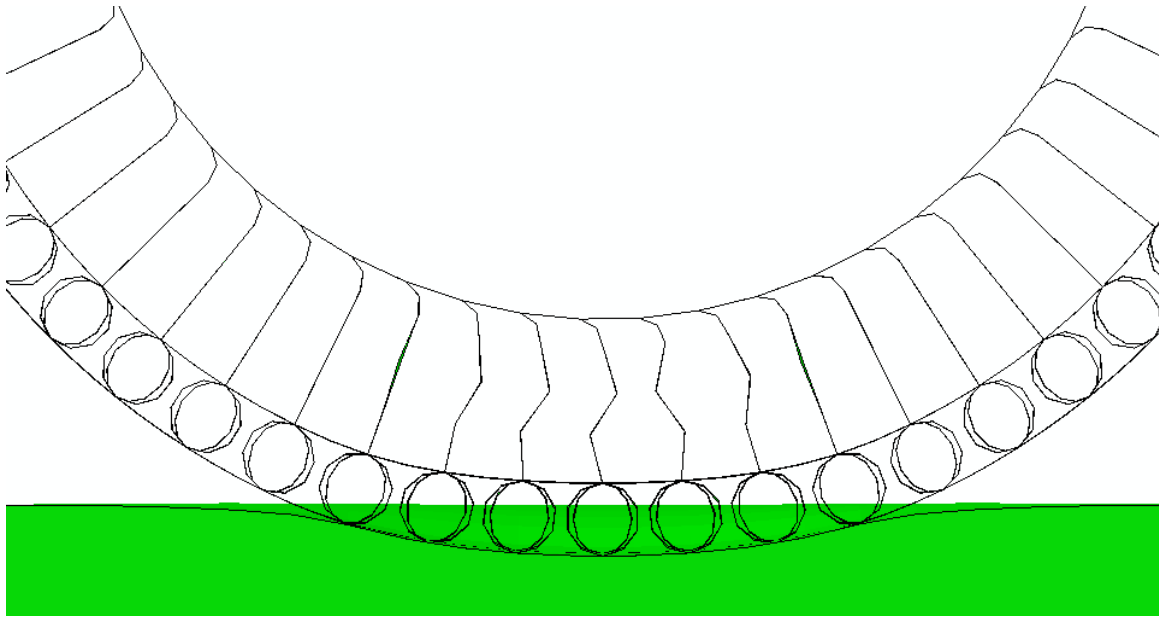


Figure 4.6 Spokes Collapsing Under Gravity Load

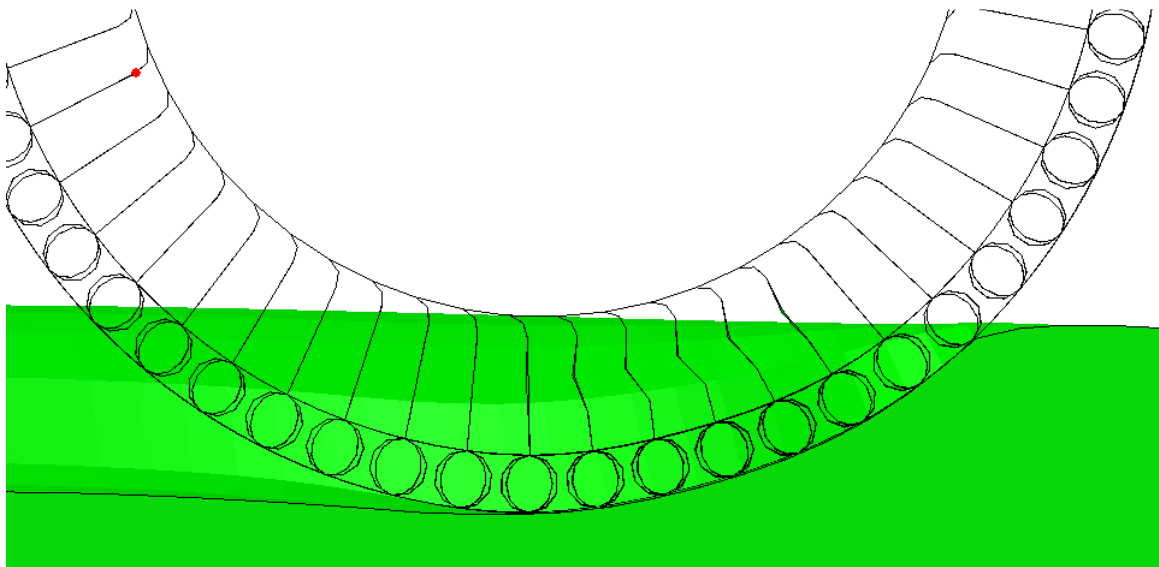


Figure 4.7 Spokes Collapsing due to Rotation

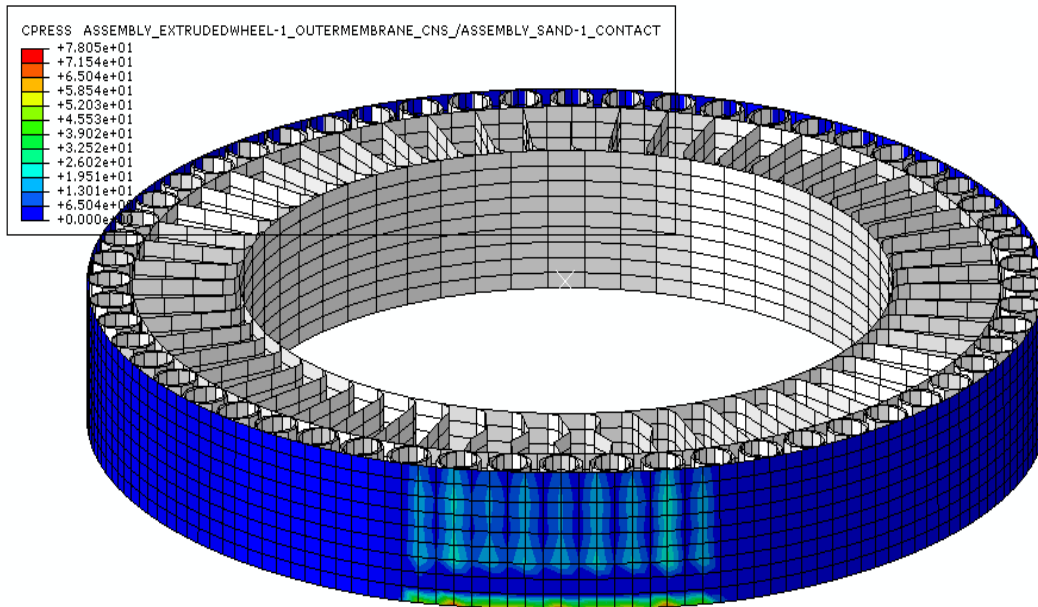


Figure 4.8 Contact Pressure due to Gravity Load (bottom is outside edge of wheel)

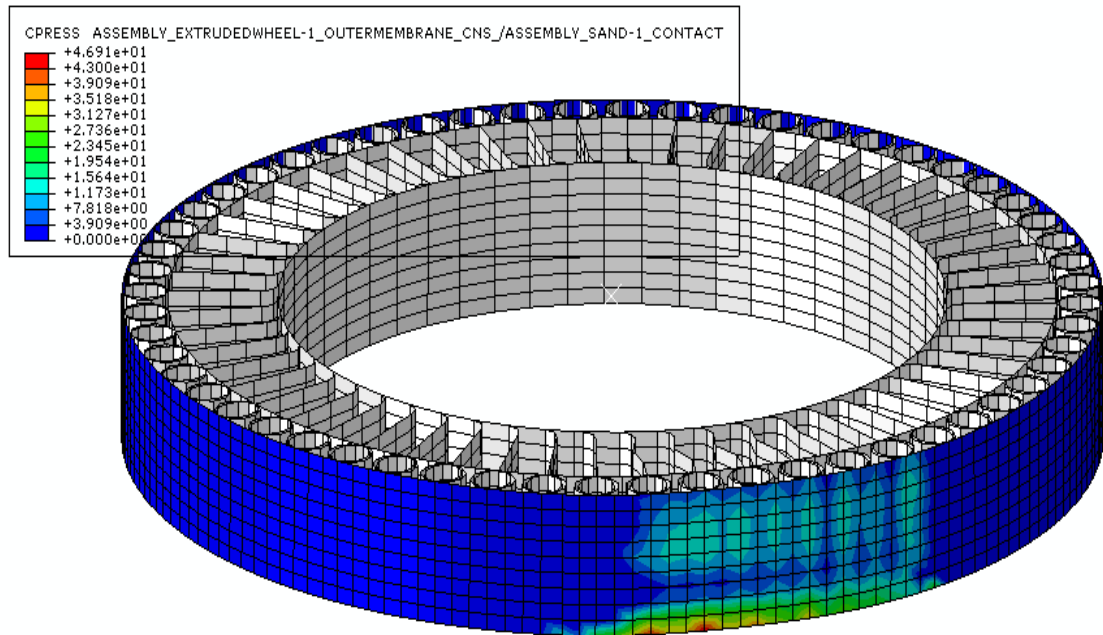


Figure 4.9 Contact Pressure due to Rotation (bottom is outside edge of wheel, rolling to the right)

Figure 4.8 and Figure 4.9 show that the pressure distribution on soil is quite different from that on a rigid surface. On the outside edge of the wheel (shown at the bottom of the figure), red pressure peaks appear directly below the cylinders. Away from the edge, smaller light blue peaks appear between cylinders. This indicates that miniature berms are created in front of and behind each cylinder. When the wheel is rolling, the contact pressure is shifted to the front half of the wheel with the highest peaks near the bottom where the soil is most compacted. This is in keeping with experimental results from Onafeko and Reece [55].

Most importantly, these results indicate that rigid surface tests may not be a good indicator of the pressure distribution on soil. It is very difficult to measure contact pressure on sand without interfering with the measurement. Numerical modeling may be the best way to obtain information about the contact pressure.

5. DEMONSTRATION OF THE INTEGRATED MODEL

In this chapter, the utility of the developed model will be demonstrated with three studies. The first study will examine how the start-up acceleration affects the distance traveled per revolution. This information will be useful in setting the operation guidelines for the ATHLETE. The second and third studies are relevant to the design of the wheel. They explore the effects of the cylinder wall thickness and the spoke stiffness. Comparative studies like these can help designers optimize performance. Physical testing is still essential, but for tests like these to be carried out, at least one physical prototype would be required for each data point. Using the model, an optimal value for each variable can be selected and physical testing can be used for final verification.

5.1 Start-up Effects

The primary purpose of this study is to demonstrate the utility of the model in informing the operation of the ATHLETE and possibly the need to optimize the model further by uncovering the effects of the rate of start-up. Three trials were run using the same angular velocity profile distributed over 5, 10, and 20 seconds. The smooth step angular velocity profile is defined by equation (5-1) [83]:

$$\omega(\xi) = \omega_i + (\omega_{i+1} - \omega_i)\xi^3(10 - 15\xi + 6\xi^2) \quad \text{where} \quad \xi = \frac{t - t_i}{t_{i+1} - t_i} \quad (5-1)$$

The velocity and acceleration for a rigid wheel with no slip are illustrated in Figure 5.1 and Figure 5.2.

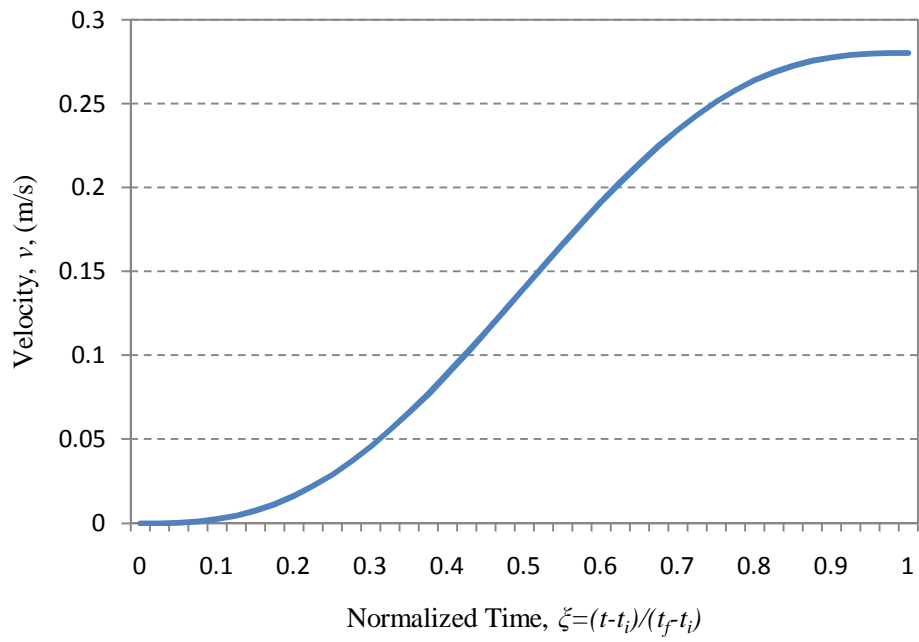


Figure 5.1 Smooth Step Velocity Profile

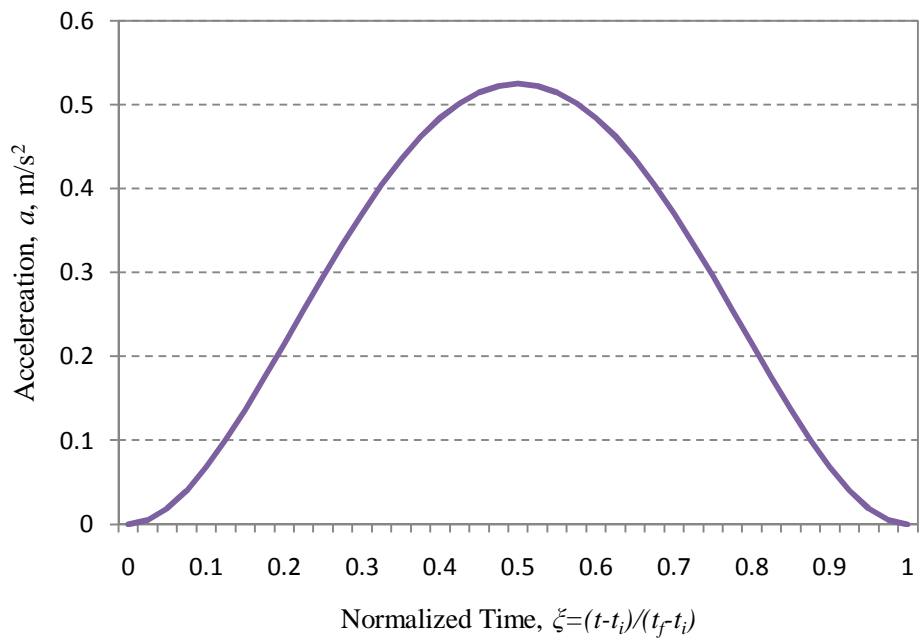


Figure 5.2 Smooth Step Acceleration Profile

The distance travelled by a rigid wheel assuming no slip can be found by integrating the product of the angular velocity and the radius over time (equation (5-2)).

$$u = \int_0^{t_f} v dt = \int_0^{t_f} r \omega dt = \frac{r \omega_f t_f}{2} \quad (5-2)$$

Angular velocity was selected as the cause of motion because all six wheels of the ATHLETE can be driving wheels. A horizontal force is typically used for towed wheels. Controlling the torque is another valid option, but angular displacement can be easily related to the horizontal velocity specification. It is anticipated that the ATHLETE will have adequate control systems to control the angular velocity. The thrust (forward force) from the soil due to the angular rotation is plotted in Figure 5.3 for the three start-up times the 12 second gravity step is not shown because thrust is negligible during the application of gravity. Thrust is also plotted for a 10 second start-up time followed by five seconds at constant speed using a dashed line. This line corresponds with the 10 second start-up line until the 22 second mark (12 seconds for the gravity step plus 10 seconds of accelerating).

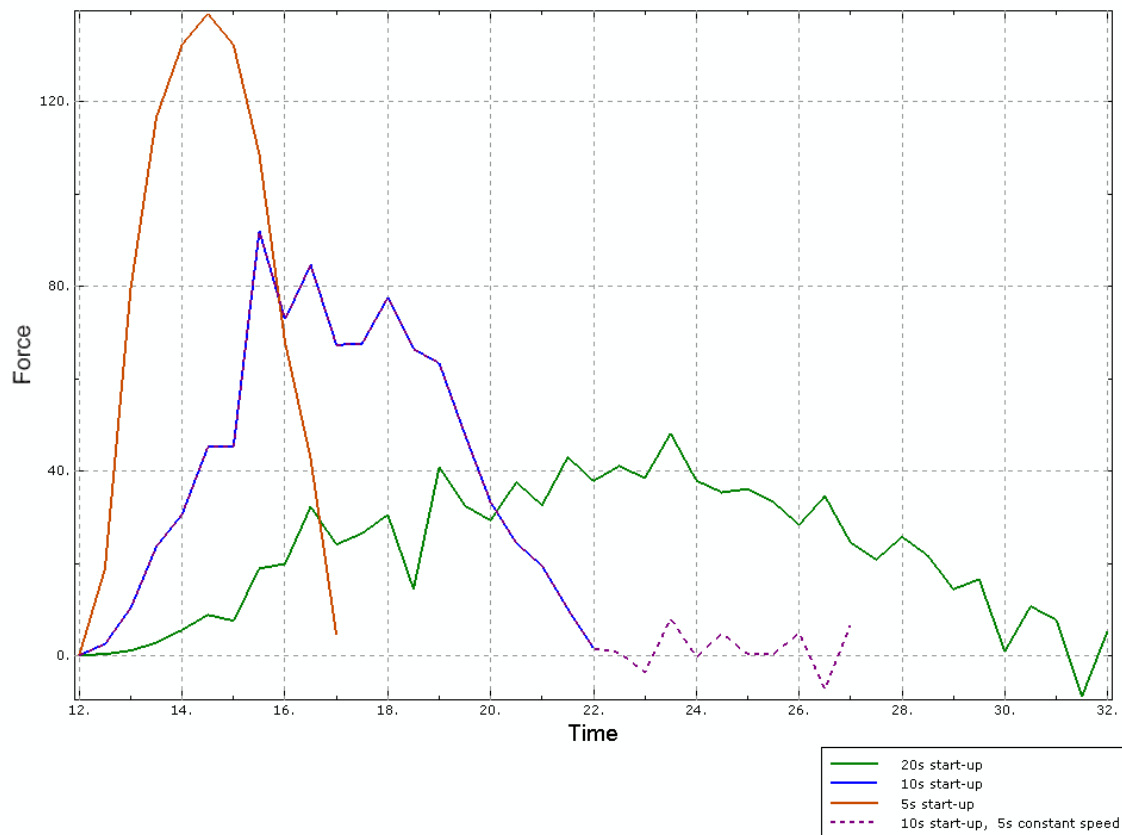


Figure 5.3 Soil Thrust over the Start-up Period

The predicted values of distance (horizontal displacement) are calculated for three different start-up times in Table 5.1. When the velocity is ramped up over 20 seconds, the wheel goes 97% of the maximum distance. When that time period is halved, the wheel still achieves almost 96% of the maximum distance, although it does sink in slightly deeper, presumably because soil is displaced from under the wheel as it spins. As the start-up time is decreased, the wheel digs deeper and does not go as far per rotation. Although physical testing should also be completed for verification, this study implies that accelerating slowly is the most efficient use of energy.

Table 5.1 Effect of Start-up Time on Traction

Start-up Time, 0 to 0.8 rad/s (s)	Vertical Displacement (mm)	Horizontal Displacement (mm)	Expected Horizontal Displacement (mm)	% Traction
20	-68.40	2719	2804	97.0%
10	-71.37	1345	1402	95.9%
5	-77.73	663	701	94.6%
10, plus 5 seconds of travel at constant angular velocity	-68.06	2717	2804	96.9%

Additionally, the results in Table 5.1 indicate that future simulations can use a start-up period of 10 seconds and a five second constant speed period with only a slight loss of traction. The same travel distance will be covered, but the simulation will not take as long because less time increments will be required. Graphical outputs are shown in Figure 5.4-Figure 5.7.

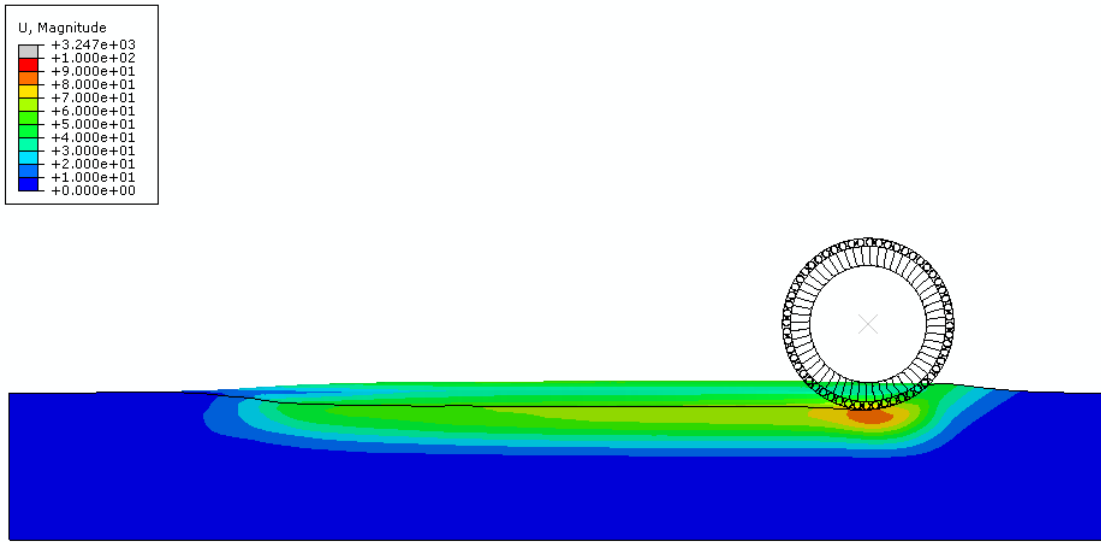


Figure 5.4 Start-up: 0 to 0.8 rad/s in 20 seconds

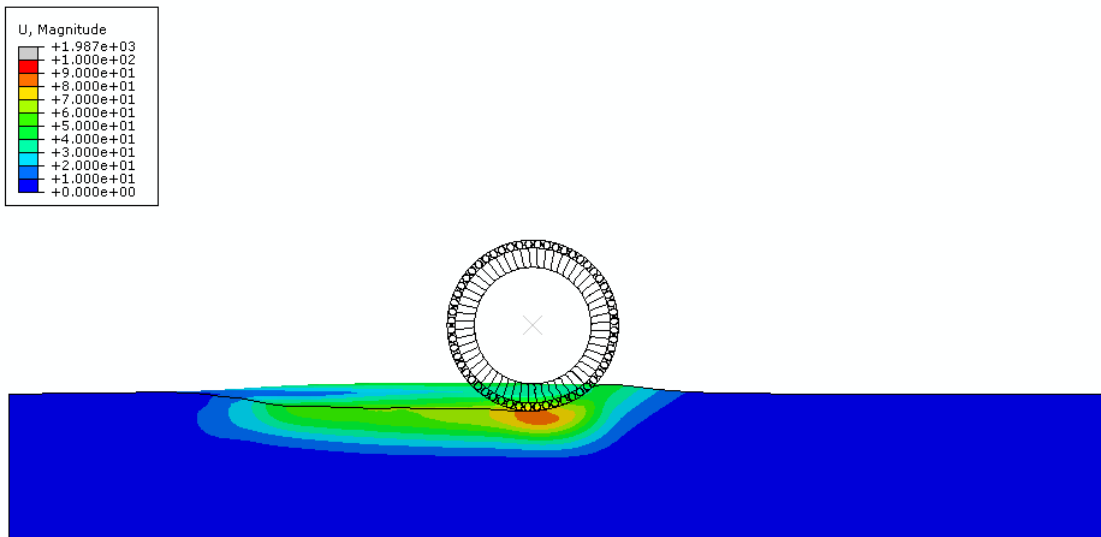


Figure 5.5 Start-up: 0 to 0.8 rad/s in 10 seconds

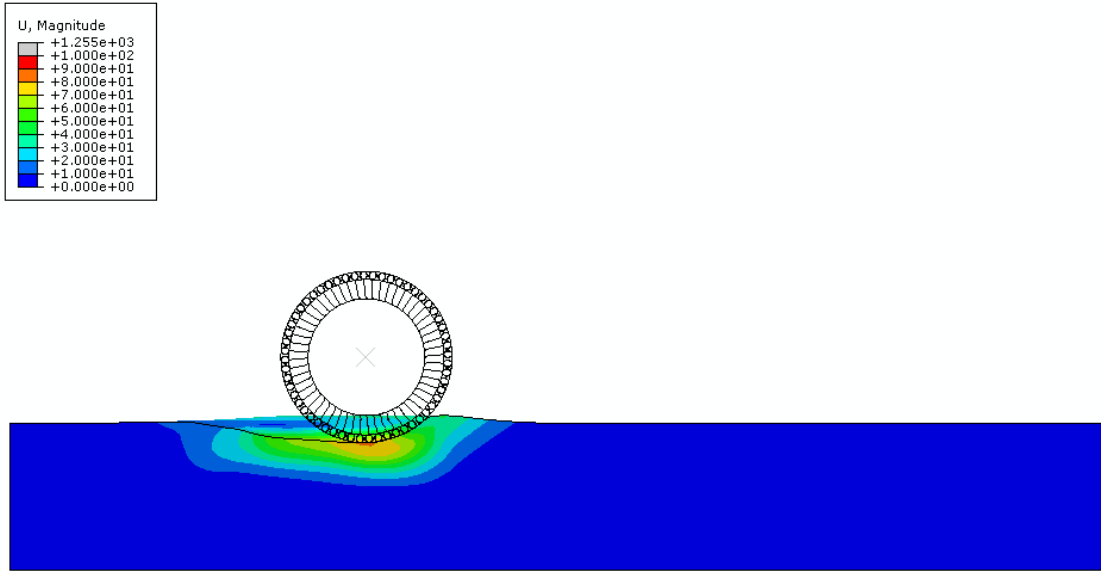


Figure 5.6 Start-up: 0 to 0.8 rad/s in 5 seconds

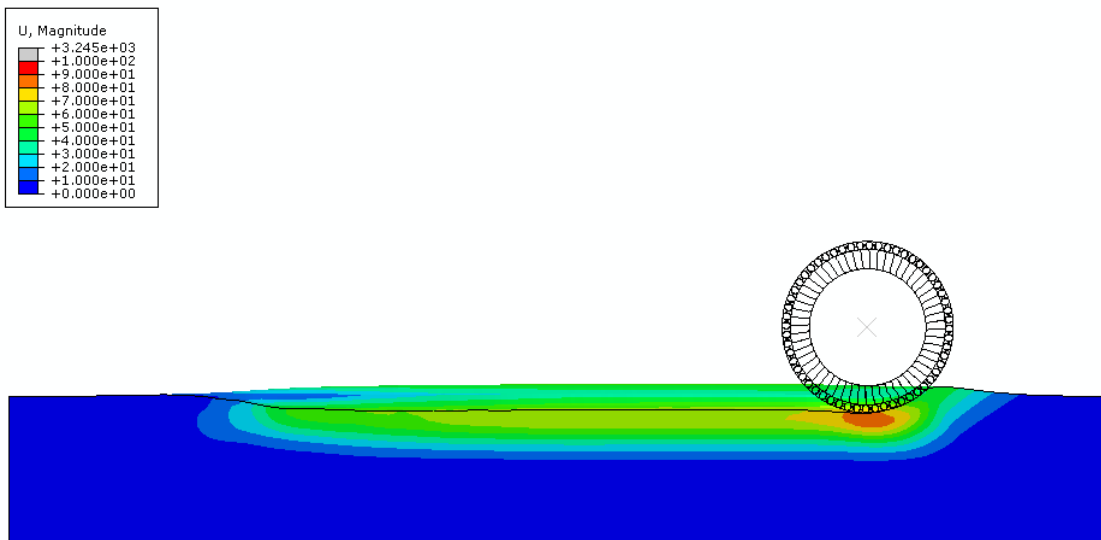


Figure 5.7 Start-up: 0 to 0.8 rad/s in 10 seconds, followed by constant speed for 5 seconds

5.2 Cylinder Wall Thickness

As described in Appendix B, the cylinder wall thickness has a direct impact on the effective shear modulus of the shear band, which in turn influences the contact pressure through equation (2-14). The cylinder with baseline wall thickness, 0.7 mm, acted nearly rigid, so two experimental values were chosen to reduce the cylinder wall thickness and hence make the wheel more deformable. The results are summarized in Table 5.2 and Figure 5.8-Figure 5.10. Note that the color map of the magnitude of displacement is the same for all figures. The 0.5 mm cylinders cause less movement of the sand which allows the wheel to travel farther than the 0.7 mm cylinders. However, when the cylinder thickness is reduced to 0.3 mm, the shear band becomes so soft that the wheel collapses on itself. Clearly the shear band would not actually pass through the hub as shown in the model, but a similar failure mechanism has been observed in a field trial after the prototype lunar wheel rolled over an obstacle. To study the behavior after collapse, self-contact must be defined, which is a simple modification, but increases the computation time.

Table 5.2 Effect of Cylinder Wall Thickness

Cylinder wall thickness (mm)	Wall time	Disp. due to gravity (mm)	Horiz. disp. (mm)	Vert. disp. (mm)	Notes
0.7	8:13:23	-25.56	2717	-68.06	Baseline
0.5	8:11:11	-26.45	2768	-60.62	
0.3	8:46:37	-126.37	2609	-151.37	Wheel collapses

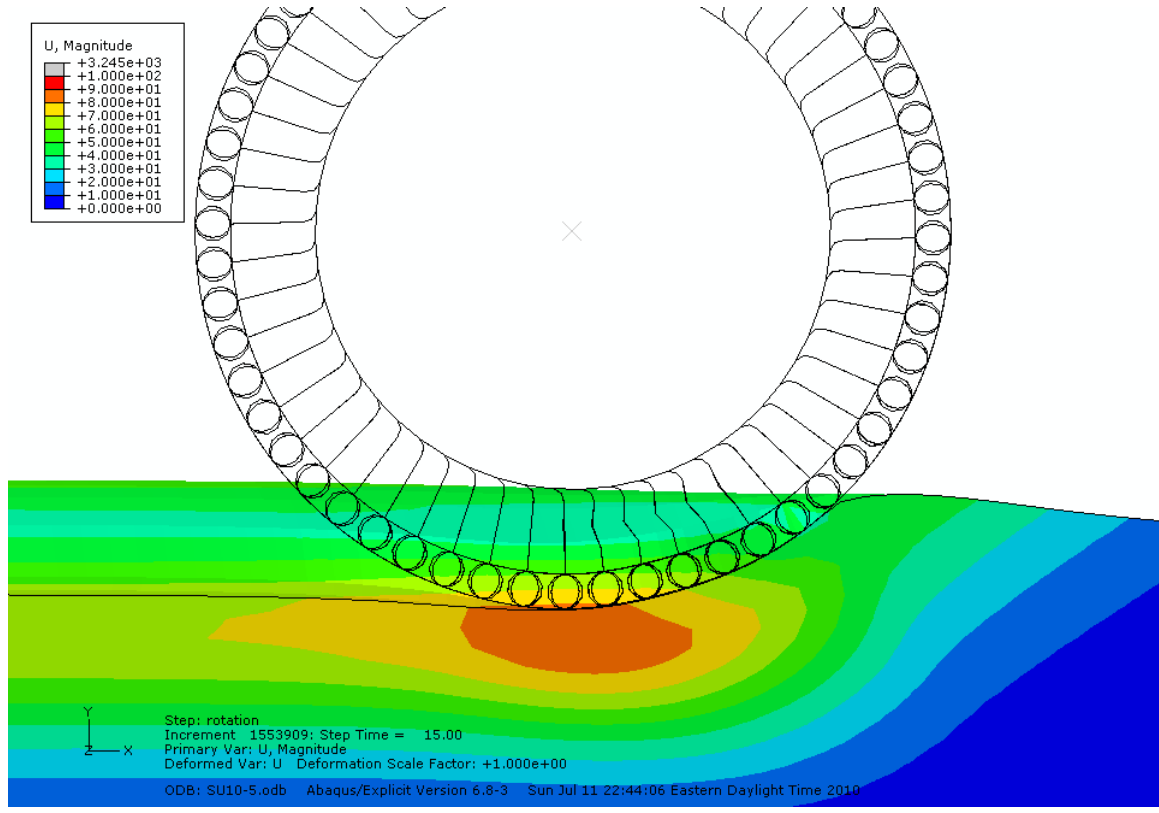


Figure 5.8 Cylinder Wall Thickness = 0.7 mm (baseline)

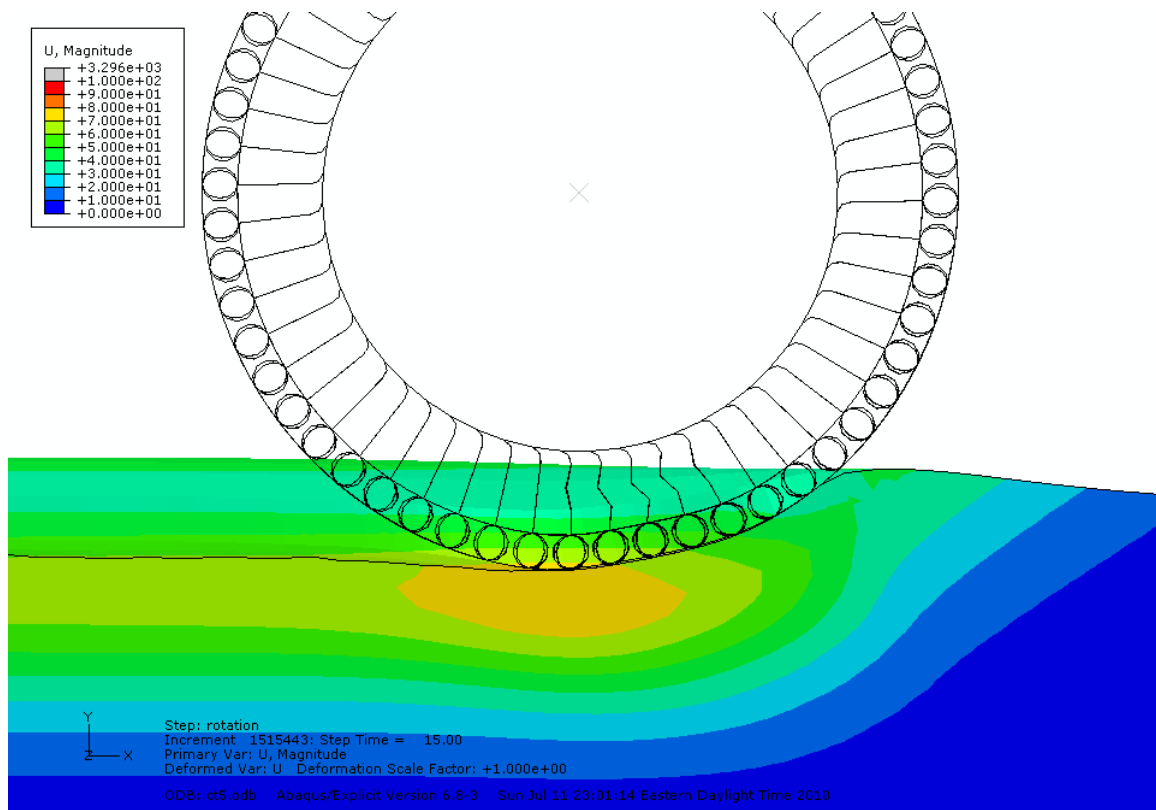


Figure 5.9 Cylinder Wall Thickness = 0.5 mm

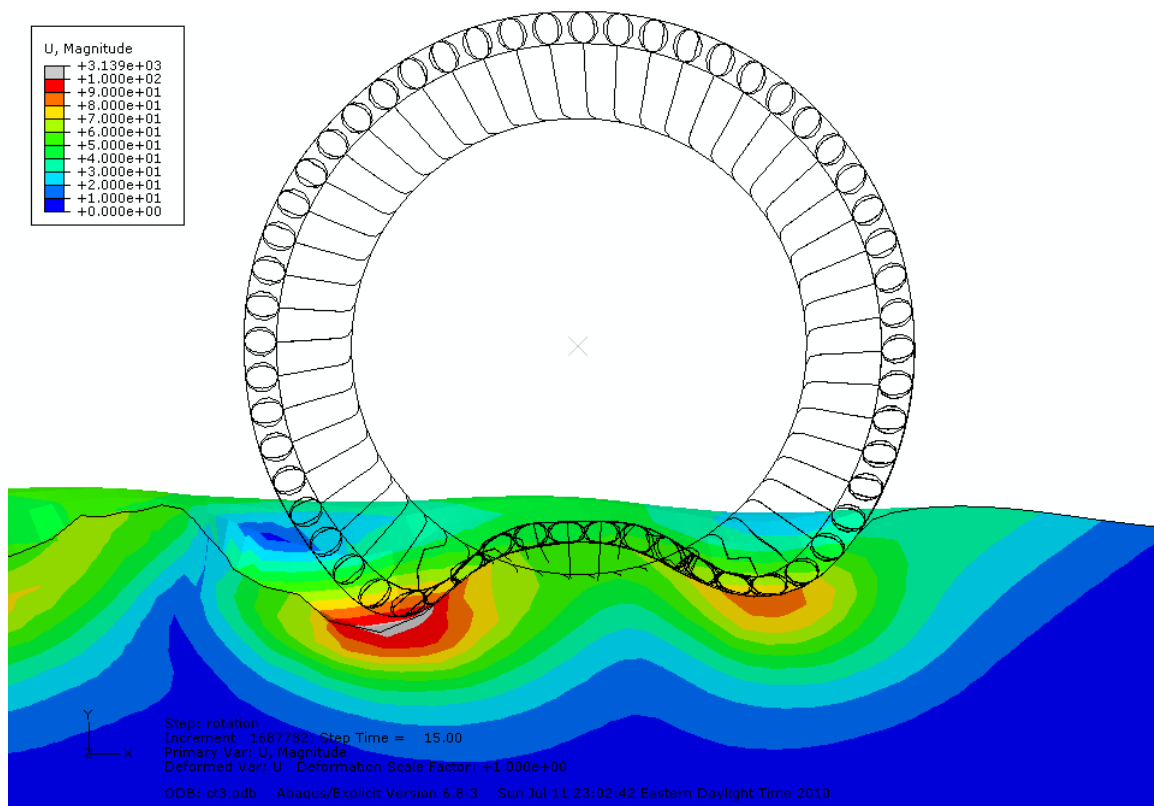


Figure 5.10 Cylinder Wall Thickness = 0.3 mm

5.3 Spoke Stiffness

According to Tweel™ mechanics [6], the spoke stiffness determines the length of the contact patch for a given displacement on a rigid surface. In this study, three spoke stiffness values are compared to determine if the proposed model predicts any differences in traction as a result. Rather than altering the material stiffness directly, the spoke extensibility is controlled by altering the thickness and therefore cross-sectional area of the spoke. The properties of the curved springboards remain unchanged. As shown in Figure 5.11, the contact area varies through the rolling step, to the contact area reported

in Figure 5.3 is taken from the two seconds after gravity has been fully applied and before rolling has begun.

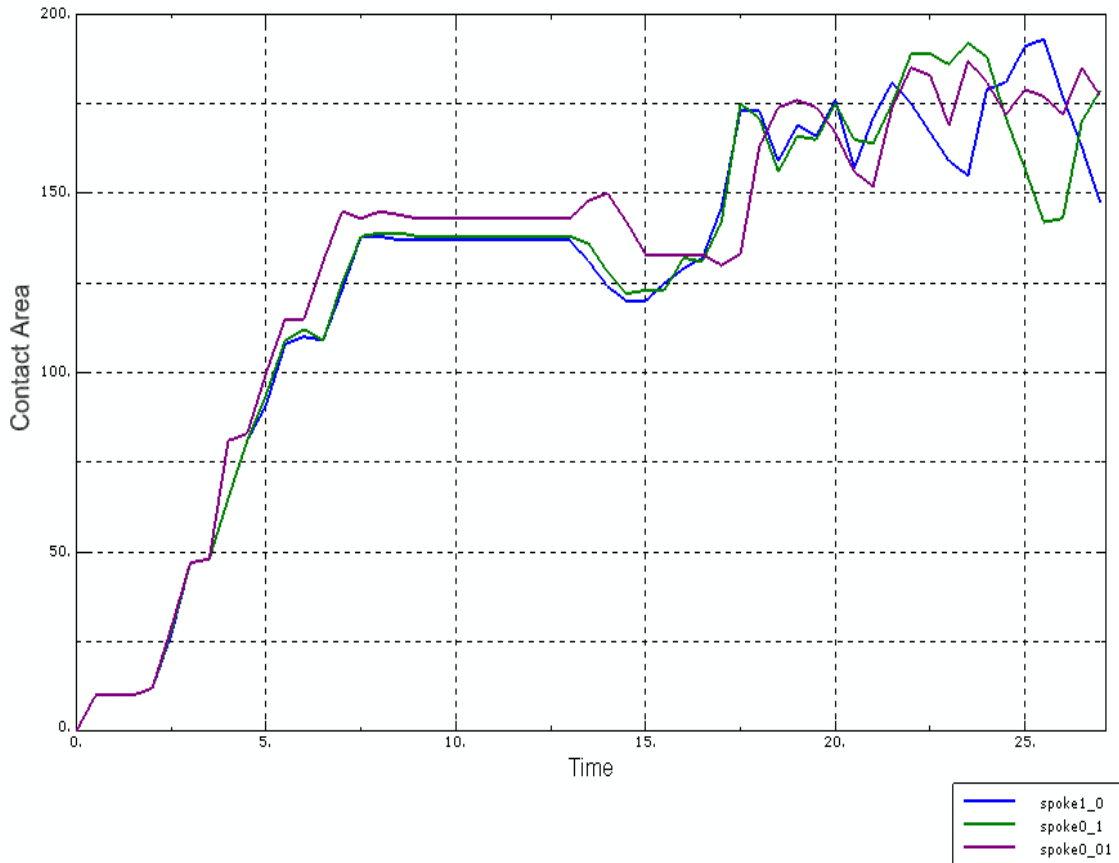


Figure 5.11 Contact Area vs. Time

Table 5.3 Effect of Spoke Stiffness on Displacement and Contact Area

Spoke thickness (mm)	Disp. due to gravity (mm)	Horizontal displacement (mm)	Vertical displacement (mm)	Contact area due to gravity (mm ²)
0.01	-28.23	2778	-60.34	143
0.1	-25.56	2717	-68.06	138
1	-25.39	2712	-69.20	137

Reducing the spoke thickness to 0.01 mm increased the distance travelled by slightly more than reducing the cylinder thickness did in the previous study. A possible direction for future work could be exploring the relationship between these two variables and finding their optimal values for maximum traction. Counter to analysis of a terrestrial Tweel™ on a rigid surface [6], for the lunar Tweel™ on sand, the contact area decreased with increasing spoke stiffness. This is probably due to the fact that the conforming nature of the soil does not require the contact area to be flat like a rigid surface does. Figures 5.12 - 5.14 show the wheel deformation.

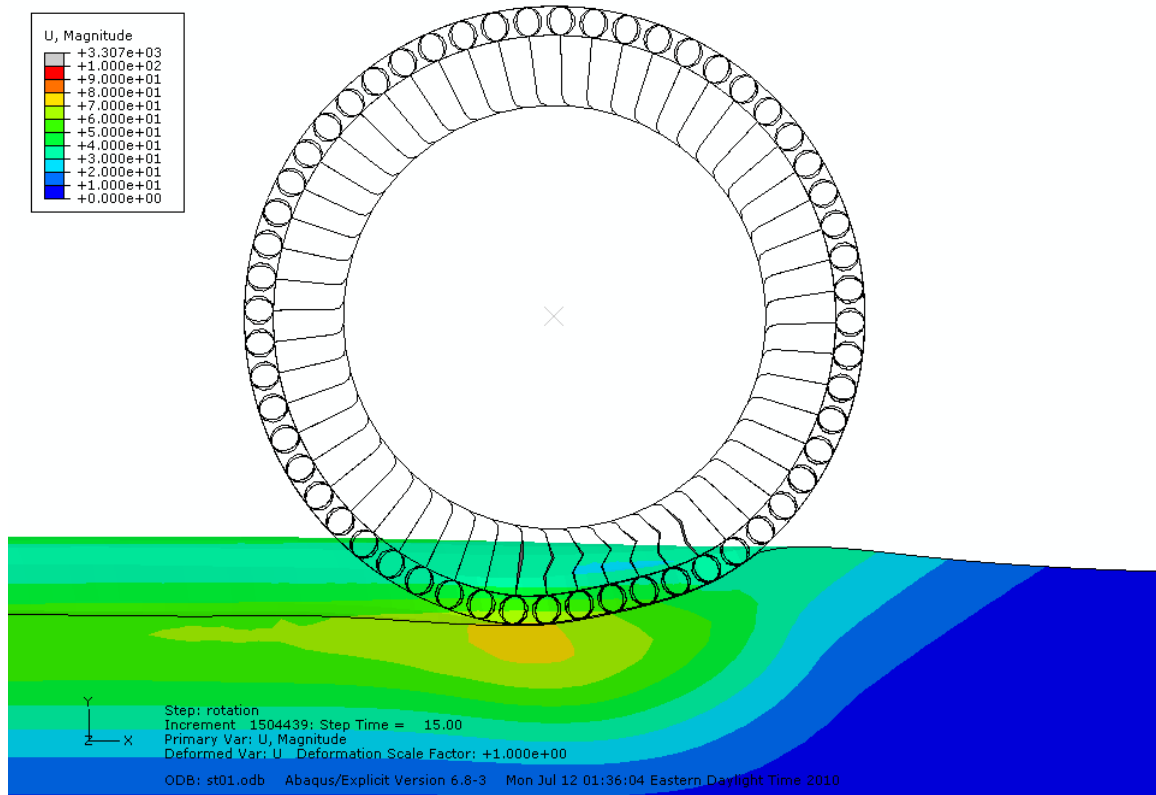


Figure 5.12 Spoke Thickness 0.01 mm

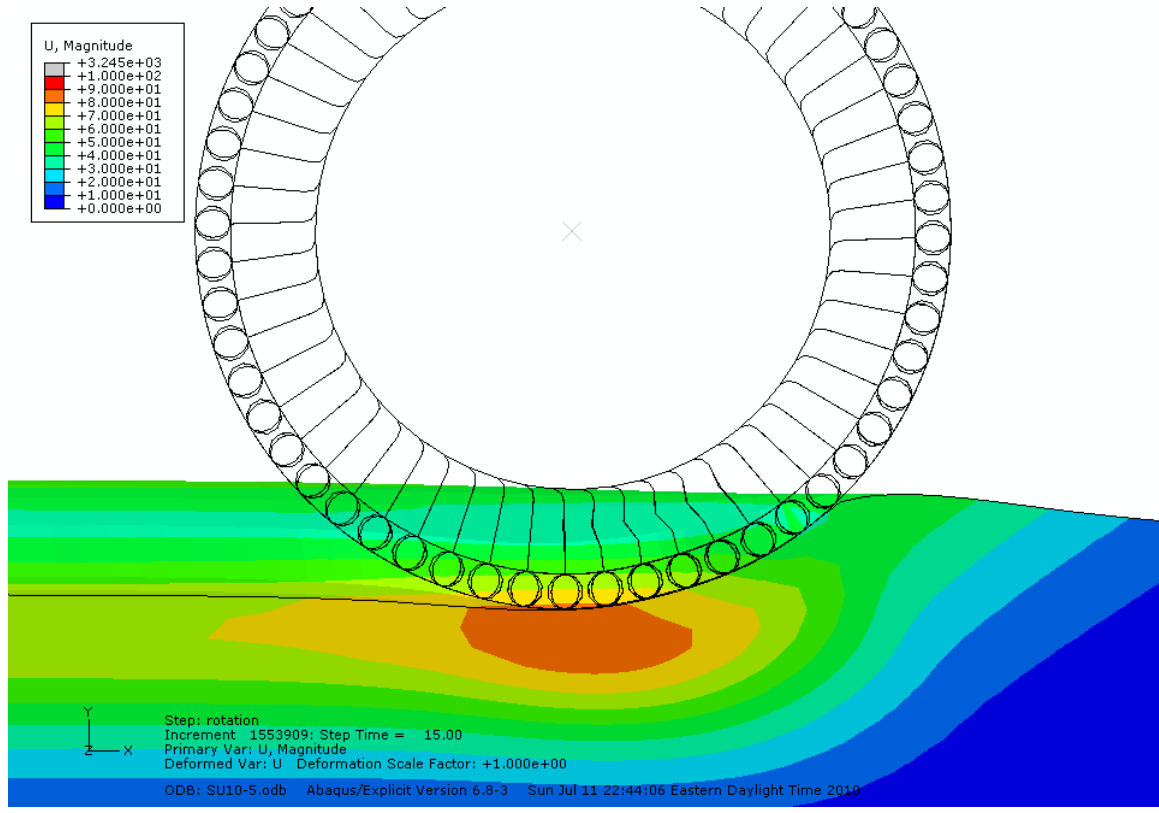


Figure 5.13 Spoke Thickness 0.1 mm

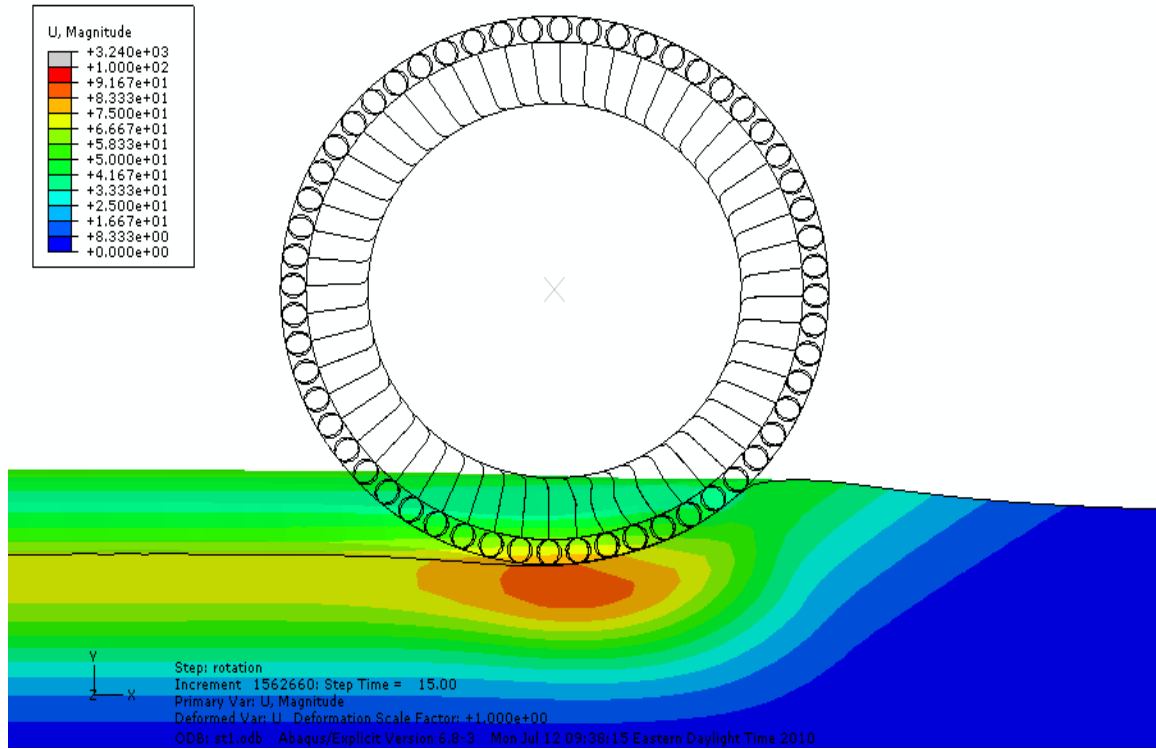


Figure 5.14 Spoke Thickness 1 mm

6. CONCLUSIONS AND FUTURE WORK

A finite element model that will allow designers to predict the behavior of a lunar Tweel™ on lunar soil has been developed and tested. Of the options considered, a shell model wheel utilizing reduced integration S4R elements with length of 12 mm around the outer ring produced the most reasonable results in the least amount of time, especially with a contact stiffness of 100 MPa/mm. A holistic method of determining the appropriate soil bed size was quick and efficient and found that the largest dimension required to capture the majority of the soil movement was the width. This dimension was almost 10 times the width of the wheel. Less than one wheel diameter was required of the depth. The wheel and soil models were successfully integrated. Studies of the rate of start-up, cylinder wall thickness, and spoke stiffness showed that the integrated model could predict differences in traction due to changes in the wheel design and operation. A summary of the research questions is presented in Table 6.1.

Table 6.1 Research Questions Answered

Research Question #1	Does a wheel model with 3-D solid elements for some of its components offer visible improvements in the prediction of the pressure distribution of the prototype wheel over a shell-based 3-D model?
	No, at least not within the limits of a 3 day maximum computation time. A single-part shell model was just as effective as a multi-part solid-shell model. This is may be due to the two-dimensional nature of the Tweel™ and may not hold true for other wheel designs. It was found that the contact stiffness was the most important variable in predicting a smooth pressure distribution.

Research Question #2	Can a constitutive model that captures experimentally observed soil behaviors such as side berms and rutting be implemented in the selected finite element code?
	Yes, an elasto-plastic, pressure-dependent, Drucker-Prager model with Cap Plasticity has been implemented in Abaqus™ using a parameter set compiled from actual lunar soil, lunar soil simulant, and Ottawa sand. Results show rutting behind the wheel and berms to the side of the wheel.
Research Question #3	How can the finite element model parameters (such as boundary conditions and soil bed dimensions) be systematically selected in order to improve efficiency and maintain accuracy?
	Soil bed dimensions can be systematically selected using a holistic method that accounts for interactions between the dimensions. With appropriately selected soil dimensions, the boundary conditions have an insignificant effect on the results.
Research Question #4	How can the model be used to inform wheel design and operation?
	The model can be used to inform wheel operation, for example, determining how quickly the wheel can accelerate without significant slippage. The model can also inform design decisions. The pilot tests in Chapter 5 suggested that softening the cylinders and/or the spokes could improve traction, but softening the cylinders too much can lead to failure.

As with all research, generating answers always generates more questions. Some of the new questions that can be studied in the future are:

1. What aspects of the model can be simplified for efficiency?
2. How does each individual wheel parameter affect performance?
3. How do different wheel parameters interact?
4. How does varying the soil parameters affect wheel performance?

Other possible future directions for this research involve modifying the model further, for example, an additional step could be added with a linearly increasing backward force to determine the drawbar pull. The drawbar pull would be equal to the force at which the wheel stops moving forward. Another option is to use a program such as Isight² to simultaneously optimize multiple wheel parameters for given mobility requirements.

The model presented here is a tool that can potentially impact future missions to the moon and perhaps one day Mars. It will allow designers to see the effect of design changes in hours instead of weeks, and thus can enhance and expedite the lunar wheel design process.

² <http://www.simulia.com/products/isight2.html>

APPENDICES

Appendix A: The Stress Tensor

The state of stress for a point in 3-dimensional space can be defined in multiple ways. Most familiar to many new engineers are the stress components, which can be presented in matrix form with subscripts x , y , and z representing coordinate directions. The first subscript represents the plane in which the stress is acting and the second indicates its direction. Often this matrix is written in indicial form, where the coordinate directions are represented by the numbers 1 through 3, as shown below.

$$\begin{bmatrix} \sigma_{xx} & \sigma_{xy} & \sigma_{xz} \\ \sigma_{yx} & \sigma_{yy} & \sigma_{yz} \\ \sigma_{zx} & \sigma_{zy} & \sigma_{zz} \end{bmatrix} = \begin{bmatrix} \sigma_{11} & \sigma_{12} & \sigma_{13} \\ \sigma_{21} & \sigma_{22} & \sigma_{23} \\ \sigma_{31} & \sigma_{32} & \sigma_{33} \end{bmatrix} = \sigma_{ij} \text{ for } i, j = 1, 2, 3 \quad (\text{A-1})$$

Cauchy has shown that in the absence of body moments, the stress tensor is symmetric, thus $\sigma_{ij} = \sigma_{ji}$. When the coordinate axes are transformed to align with the principal stress directions, the stress tensor takes the form

$$\sigma_{ij} = \begin{bmatrix} \sigma_1 & 0 & 0 \\ 0 & \sigma_2 & 0 \\ 0 & 0 & \sigma_3 \end{bmatrix} \quad (\text{A-3})$$

where σ_1 , σ_2 , and σ_3 are the major (largest positive or smallest negative), intermediate, and minor (smallest positive or largest negative) principal stresses. Because this tensor can take many forms, it is often convenient to use the invariants of the stress tensor. The invariants are subject to a variety of naming conventions. Based on a compilation of multiple sources [89, 87, 81], the following nomenclature and definitions are selected for this document.

$$\begin{aligned}
I_1 &= \sigma_1 + \sigma_2 + \sigma_3 \\
I_2 &= \sigma_1\sigma_2 + \sigma_2\sigma_3 + \sigma_3\sigma_1 \\
I_3 &= \sigma_1\sigma_2\sigma_3
\end{aligned}
\tag{A-4}$$

The stress tensor can also be decomposed into hydrostatic and deviatoric components. The mean stress, p , is one third of the first stress invariant, I_1 . The deviatoric tensor, s_{ij} , can then be calculated according to equation B-5 using the Kronecker delta, δ_{ij} , which has a value of 1 when $i = j$ and 0 when $i \neq j$.

$$s_{ij} = \sigma_{ij} - p\delta_{ij} \tag{A-5}$$

The deviatoric stress tensor has its own invariants:

$$\begin{aligned}
J_1 &= s_{kk} = 0 \\
J_2 &= \frac{1}{2} s_{ij}s_{ij} = \frac{1}{3} (I_1^2 + 2I_3) \\
J_3 &= \frac{1}{3} s_{ij}s_{jk}s_{ki} = \frac{1}{27} (2I_1^3 + 9I_1I_2 + 27I_3)
\end{aligned}
\tag{A-6}$$

The second deviatoric stress invariant indicates the magnitude of shear stress, and the third represents the direction.

In soil mechanics, common variables used to define yield surfaces can be defined in terms of the invariants described above. These are the mean pressure, p ; the generalized shear stress, q ; and a manipulation of the third deviatoric invariant called r . Unlike the original invariants, these variables all have units of force per length-squared.

$$\begin{aligned}
p &= \frac{1}{3} I_1 \\
q &= \sqrt{3J_2} \\
r &= \left(\frac{27}{2} J_3\right)^{1/3}
\end{aligned}
\tag{A-7}$$

Appendix B: Characterization of Discrete Shear Band

Recalling equation (2-14), the interesting parameters related to the shear band are the shear modulus, G , and the height, h . The outer radius, R , cannot be increased due to design limitations. Because the shear band is not composed of a continuous material, changing G is not straightforward. A proxy parameter for the shear modulus, G , is the thickness, t , of the glass cylinder walls. The height of the shear band can be easily changed; however, changing the height also changes the geometry of the cylinders and therefore the effective shear modulus, as well as the spacing between cylinders. Before a factorial experiment is designed, it is prudent to explore the relationships between the variables of interest, t and h , and their effects on the *effective* shear modulus.

To understand the effects of changing the geometric parameters on the meta-material shear properties, two experiments were carried out. The goal of the experiments was to find the effect of changing the cylinder height and thickness on the effective shear modulus, respectively. Because the shear band is discontinuous, it does not truly have a single shear modulus, but by setting up a simple coupon test we can calculate an *effective* shear modulus as a ratio of shear stress (over a predetermined area) to shear deformation.

For the reference wheel configuration, the arc length between cylinder centers is 39.4 mm at the outer radius. For the experiment, each cylinder is sandwiched between two rigid plates that are 39.4 mm long and 50 mm deep (Figure B.1). The bottom plate is fixed and the top plate is constrained to remain horizontal.

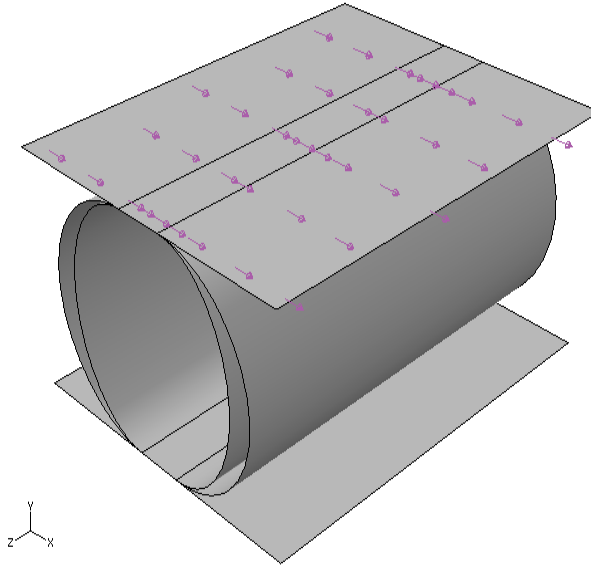


Figure B.1 Coupon Test

A horizontal velocity is applied to the top plate, which is free to move vertically. The shear stress is plotted against the shear deformation, and the effective shear modulus is taken to be the slope of the linear portion of the graph.

B.1 Coupon Test 1: Shear Band Height

For all three cases, the cylinder wall thickness was held constant at the reference configuration value. Case 1 is the reference configuration, with height 31.2 mm. Case 2 is half that height, and so it has 2 sets of cylinders. Case 3 is one quarter of the height and has four cylinder sets. These are shown in Figure B.2 through Figure B.4. The color map of the von Mises stress is the same for all three figures and the size is approximately to scale.

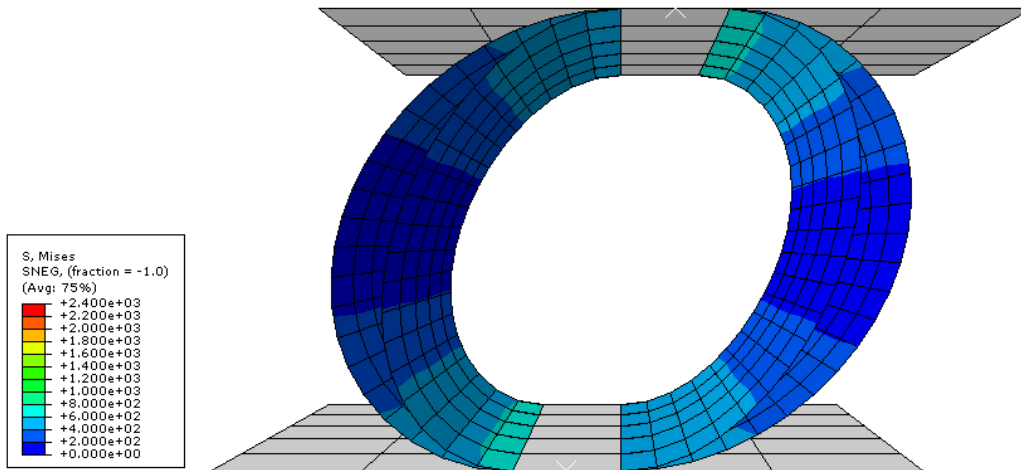


Figure B.2 Case 1, Height = 31.2 mm, 1 cylinder set

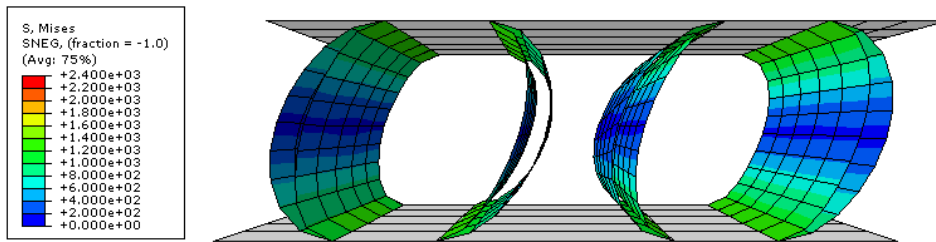


Figure B. 3 Case 2, Height = 15.6 mm, 2 cylinder sets

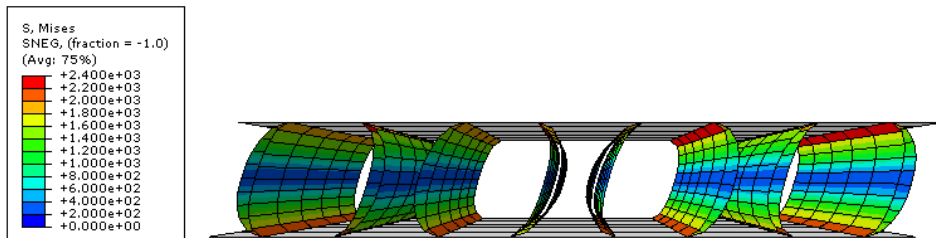


Figure B.4 Case 3, Height = 7.8 mm, 4 cylinder sets

For each case, the shear stress was plotted against the shear strain in Figure B.5. This graph shows that in the linear region, the effective shear modulus is approximately inversely proportional to h^3 .

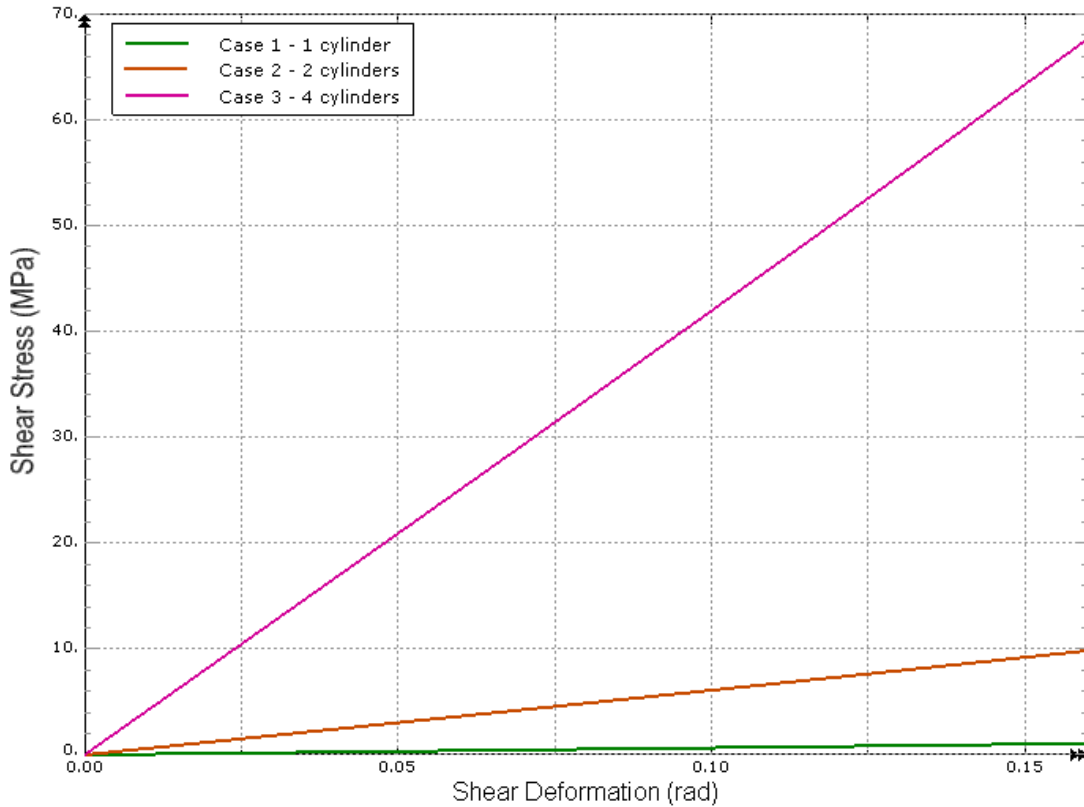


Figure B.5 Shear Stress vs. Strain for Three Shear Band Heights

B.2 Coupon Test 2: Cylinder Wall Thickness

For the cylinder wall thickness coupon test, the height was held constant at the reference value and the cylinder wall thickness was set to $0.5t$, t , and $2t$, respectively for cases 1, 2, and 3. These results are shown in Figure B.6. As shown in Figure B.5 and

Figure B.6, the effective shear modulus is approximately proportional to t^3/h^3 in the linear region.

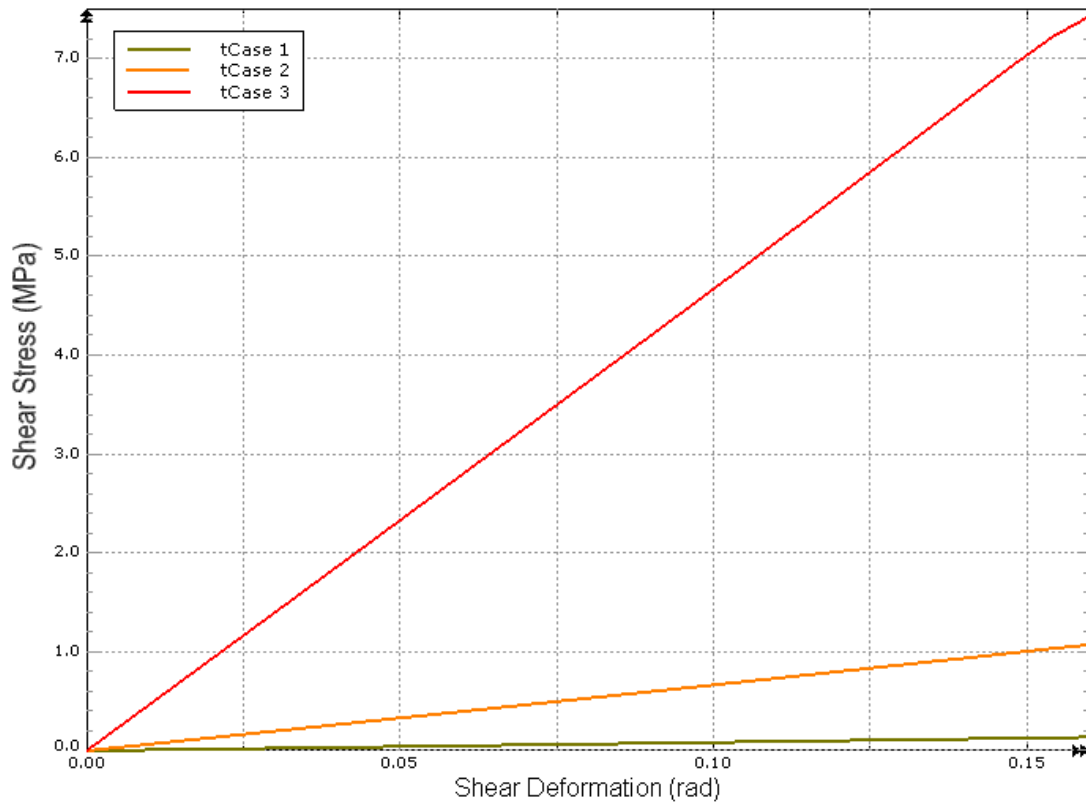


Figure B.6 Shear Stress vs. Strain for Three Glass Cylinder Thicknesses

Appendix C: Implementation on the Palmetto Cluster

The Palmetto Cluster is a shared computing infrastructure operating at 66 teraFLOPS (trillion floating point operations per second), which ranks 85th in the world³. It is the sixth most powerful supercomputing site at an academic institution in the US as of June 2010. This section describes the process by which jobs can be created and run on the Palmetto Cluster. The first step is creating the job in Abaqus/CAE. This includes defining the geometry, boundary conditions, loads, and mesh. Once this step is completed, the input file can be written, as shown in Figure C.1. A sample input file is included in Appendix D.

³ <http://www.top500.org/list/2010/06/100>

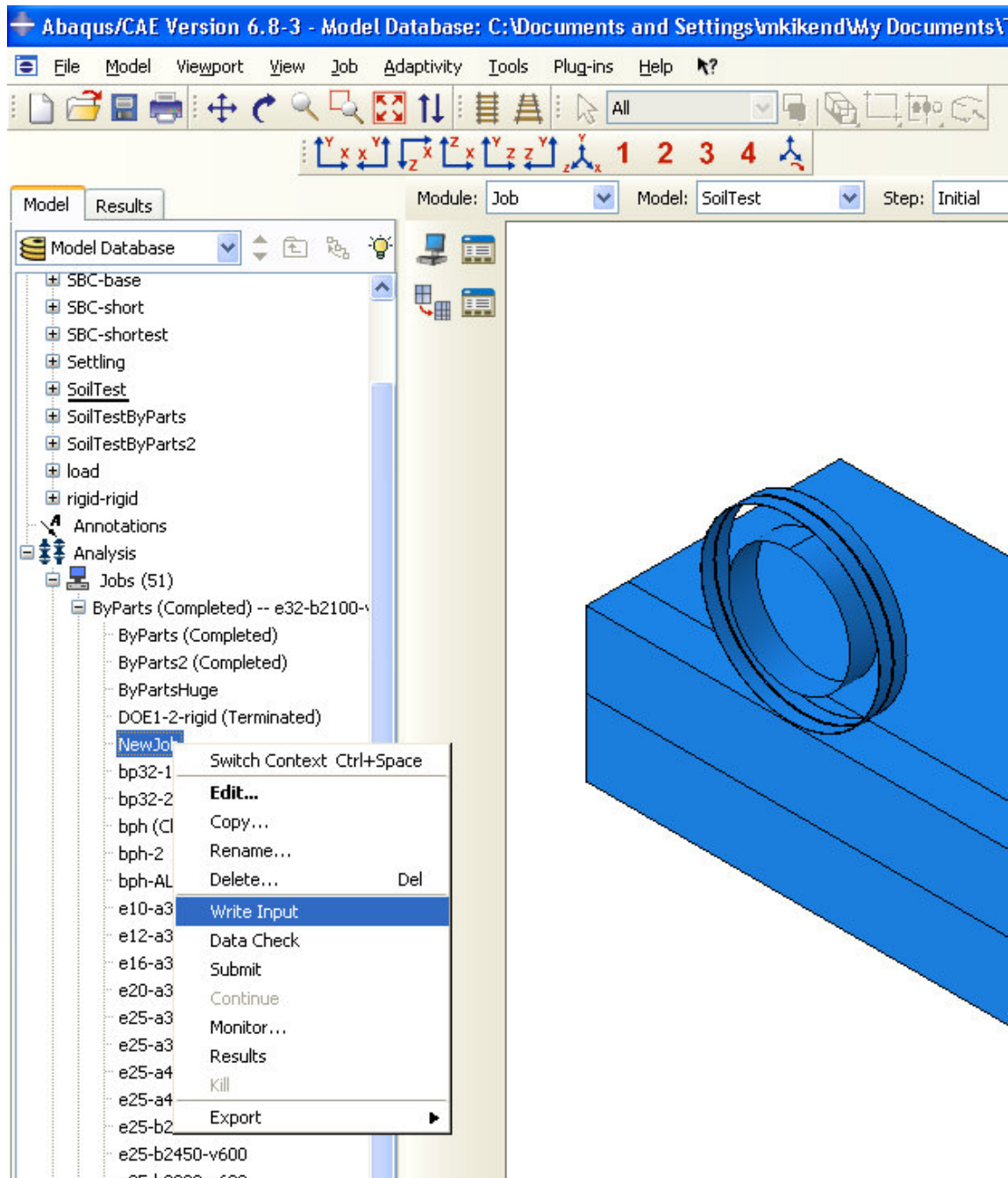


Figure C.1 Writing the Input File

Next, the file must be uploaded to the server. In this case the folder /lustre/marisaklustre/new was used (Figure C.2). The /lustre folder is very large, but any files that have not been accessed in a month are deleted. This makes it ideal for running simulations that create multiple extraneous output files.

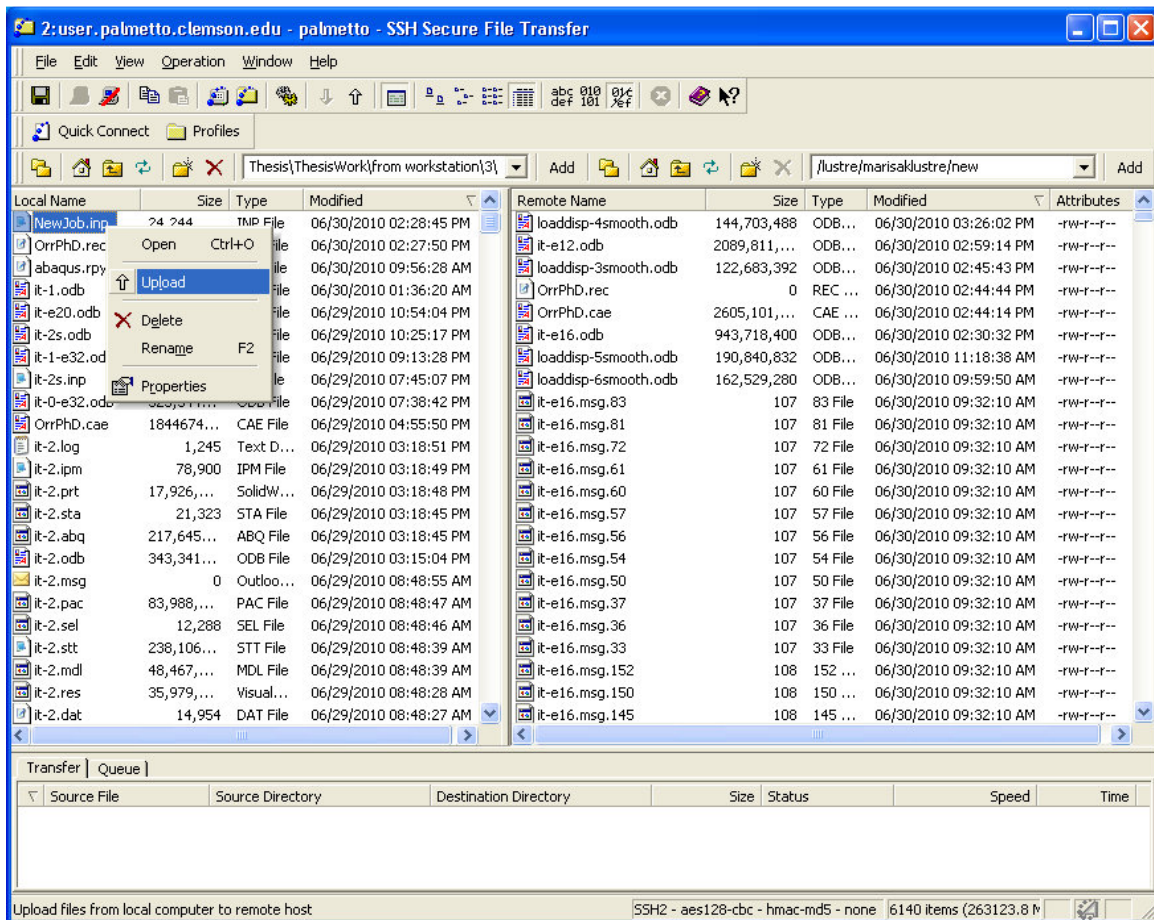
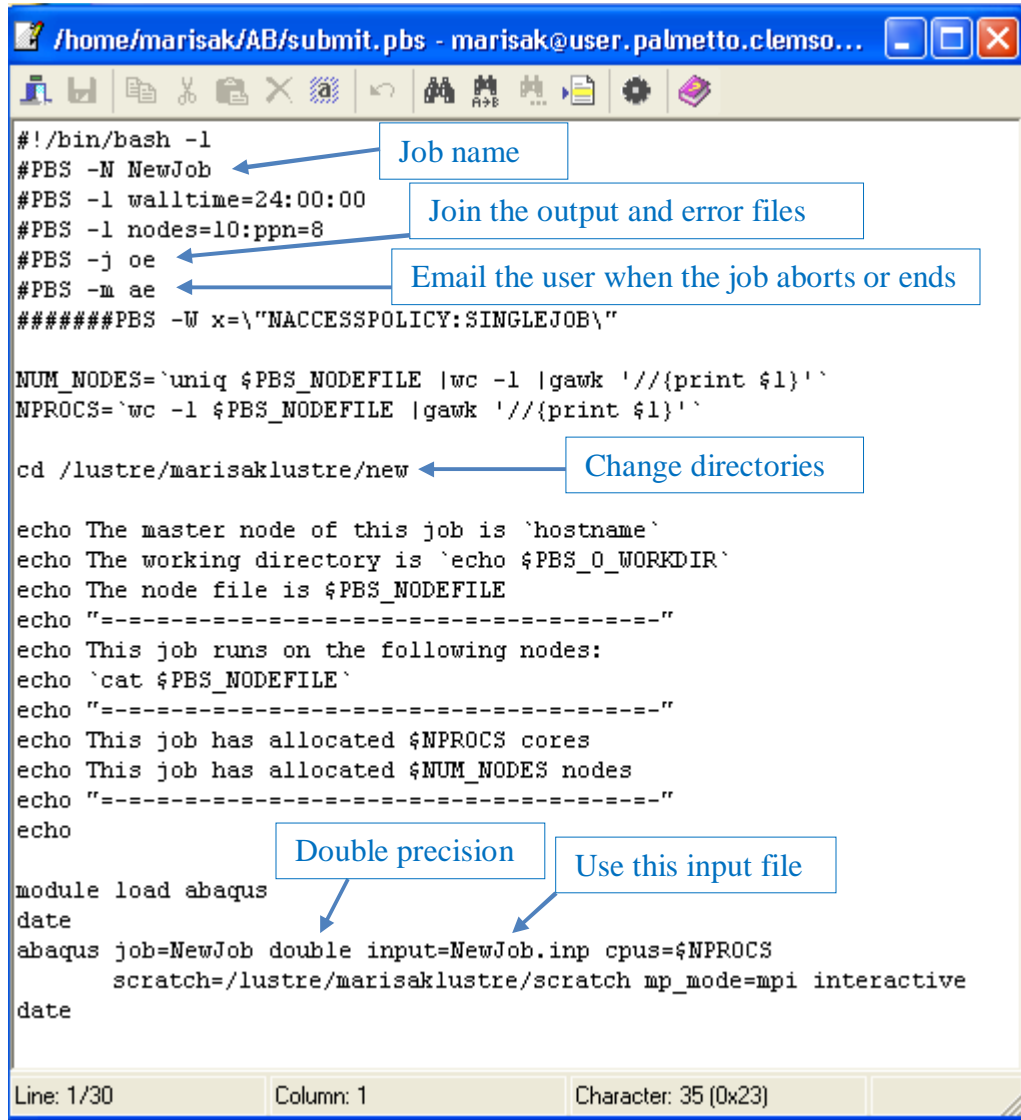


Figure C.2 Uploading to the Remote Directory

In order to submit the job to the cluster queue, a .pbs file is created like the one in Figure C.3, which is saved in /home/marisak/AB/submit.pbs



```
#!/bin/bash -l
#PBS -N NewJob
#PBS -l walltime=24:00:00
#PBS -l nodes=10:ppn=8
#PBS -j oe
#PBS -m ae
#####PBS -W x=\ "NACCESSPOLICY:SINGLEJOB\ "

NUM_NODES=`uniq $PBS_NODEFILE |wc -l |gawk '{print $1}'`
NPROCS=`wc -l $PBS_NODEFILE |gawk '{print $1}'`

cd /lustre/marisaklustre/new

echo The master node of this job is `hostname`
echo The working directory is `echo $PBS_O_WORKDIR`
echo The node file is $PBS_NODEFILE
echo "-----"
echo This job runs on the following nodes:
echo `cat $PBS_NODEFILE`
echo "-----"
echo This job has allocated $NPROCS cores
echo This job has allocated $NUM_NODES nodes
echo "-----"
echo

module load abaqus
date
abaqus job=NewJob double input=NewJob.inp cpus=$NPROCS
scratch=/lustre/marisaklustre/scratch mp_mode=mpi interactive
date
```

Annotations in the image:

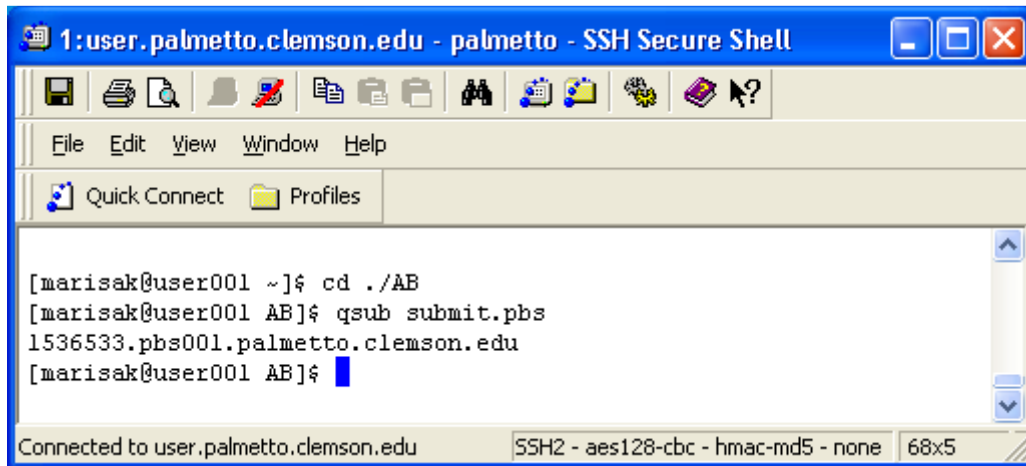
- Job name: points to `#PBS -N NewJob`
- Join the output and error files: points to `#PBS -j oe`
- Email the user when the job aborts or ends: points to `#PBS -m ae`
- Change directories: points to `cd /lustre/marisaklustre/new`
- Double precision: points to `double` in the abaqus command
- Use this input file: points to `input=NewJob.inp` in the abaqus command

Terminal status bar: Line: 1/30, Column: 1, Character: 35 (0x23)

Figure C.3 Creating a .pbs File

This file tells the cluster the job's name, how long to let it run, how many nodes to run it one, and where to write the output files.

Next, SSH Secure Shell is used to submit the .pbs file (Figure C.4). The first command is to change the directory to where the .pbs file is located. The second command, qsub, submits the file to the queue.



```
1:user.palmetto.clemson.edu - palmetto - SSH Secure Shell
File Edit View Window Help
Quick Connect Profiles
[marisak@user001 ~]$ cd ./AB
[marisak@user001 AB]$ qsub submit.pbs
1536533.pbs001.palmetto.clemson.edu
[marisak@user001 AB]$
```

Connected to user.palmetto.clemson.edu SSH2 - aes128-cbc - hmac-md5 - none 68x5

Figure C.4 Submitting the .pbs File to the Queue

When the job completes, an email is sent to the user detailing the computer resources and wall time used. The output database (.odb) file can then be downloaded from the /lustre directory and Abaqus/Viewer can be used to examine the results.

Appendix D: Sample Abaqus Input File

The complete file may be obtained by contacting Marisa Orr,
mkorr@alumni.clemson.edu

```
*Heading
** Job name: SU10-5 Model name: shell-soil
** Generated by: Abaqus/CAE Version 6.8-3
*Preprint, echo=NO, model=NO, history=NO, contact=NO
**
** PARTS
**
*Part, name=extrudedwheel
*Node
    1,      0.,      350.5,      0.
    2,      0.,      350.5,     110.

...<8000 pages omitted for brevity>

*Surface, type=ELEMENT, name=contact
_contact_S5, S5
** Section: sand2
*Solid Section, elset=Layer2, material=LunarSand2inscr

** Section: sand1
*Solid Section, elset=Layer1, material=LunarSand1inscr

*End Part
**
**
** ASSEMBLY
**
*Assembly, name=Assembly
**
*Instance, name=sand-1, part=sand
    700.,      0.,     -1100.
*End Instance
**
*Instance, name=extrudedwheel-1, part=extrudedwheel
```

```

0., 350.5, -110.
*End Instance
**
*Node
1, 0., 0., 0.
*Surface, type=NODE, name=extrudedwheel-1_OuterMembrane_CNS_,
internal
extrudedwheel-1.OuterMembrane, 1.
** Constraint: Hub
*Rigid Body, ref node=extrudedwheel-1.HubRefPt, elset=extrudedwheel-
1.Hub
*End Assembly
*Amplitude, name=SU5, definition=SMOOTH STEP
0., 0., 10., 1.,
100., 1.
*Amplitude, name=SU10, definition=SMOOTH STEP
0., 0., 10., 1.,
100., 1.
*Amplitude, name=SU20, definition=SMOOTH STEP
0., 0., 20., 1.,
100., 1.
*Amplitude, name=gravity, definition=SMOOTH STEP
0., 0., 10., 1.,
20., 1., 100., 1.
**
** MATERIALS
**
*Material, name=GlassCompositeIso40k
*Density
1.89e-09,
*Elastic
39969., 0.29
*Material, name=LunarSandlinscr
*Cap Plasticity
0.00101, 49.2, 0.4, 0., 0.05, 1.
*Cap Hardening
0.0069, 0.
0.01, 0.00158
0.02, 0.004532
0.04, 0.007483
0.06, 0.00921
0.08, 0.010435
0.1, 0.011385
0.15, 0.013111
0.2, 0.014336
0.3, 0.016063
0.4, 0.017288
0.5, 0.018238
0.6, 0.019014
0.7, 0.019671
0.8, 0.020239

```

```

    0.9, 0.020741
    1., 0.021189
    10., 0.030994
*Density
  1.58e-09,
*Elastic
  182.4, 0.3
*Material, name=LunarSand2inscr
*Cap Plasticity
  0.00278, 51.9, 0.4, 0., 0.05, 1.
*Cap Hardening
  0.0069, 0.
    0.01, 0.00158
    0.02, 0.004532
    0.04, 0.007483
    0.06, 0.00921
    0.08, 0.010435
    0.1, 0.011385
    0.15, 0.013111
    0.2, 0.014336
    0.3, 0.016063
    0.4, 0.017288
    0.5, 0.018238
    0.6, 0.019014
    0.7, 0.019671
    0.8, 0.020239
    0.9, 0.020741
    1., 0.021189
    10., 0.030994
*Density
  1.74e-09,
*Elastic
  182.4, 0.3
*Material, name=LunarSand3inscr
*Cap Plasticity
  0.00278, 51.9, 0.4, 0., 0.05, 1.
*Cap Hardening
  0.0069, 0.
    0.01, 0.00158
    0.02, 0.004532
    0.04, 0.007483
    0.06, 0.00921
    0.08, 0.010435
    0.1, 0.011385
    0.15, 0.013111
    0.2, 0.014336
    0.3, 0.016063
    0.4, 0.017288
    0.5, 0.018238
    0.6, 0.019014
    0.7, 0.019671

```

```

    0.8, 0.020239
    0.9, 0.020741
    1., 0.021189
    10., 0.030994
*Density
  1.8e-09,
*Elastic
  182.4, 0.3
*Material, name=leather
*Density
  1.9e-09,
*Elastic
  500., 0.3
**
** INTERACTION PROPERTIES
**
*Surface Interaction, name=Smooth
*Friction
  0.,
*Surface Behavior, pressure-overclosure=HARD
*Surface Interaction, name=friction1
*Friction
  1.,
*Surface Behavior, pressure-overclosure=HARD
*Surface Interaction, name=friction104
*Friction
  1.04,
*Surface Behavior, pressure-overclosure=LINEAR
  100.,
*Surface Interaction, name=rough
*Friction, rough
*Surface Behavior, pressure-overclosure=HARD
**
** BOUNDARY CONDITIONS
**
** Name: back Type: Velocity/Angular velocity
*Boundary, type=VELOCITY
sand-1.back, 1, 1
sand-1.back, 2, 2
sand-1.back, 3, 3
** Name: fixbottom Type: Velocity/Angular velocity
*Boundary, type=VELOCITY
sand-1.bottom, 2, 2
** Name: holdwheel Type: Velocity/Angular velocity
*Boundary, type=VELOCITY
extrudedwheel-1.HubRefPt, 1, 1
extrudedwheel-1.HubRefPt, 3, 3
extrudedwheel-1.HubRefPt, 4, 4
extrudedwheel-1.HubRefPt, 5, 5
** Name: sides Type: Velocity/Angular velocity
*Boundary, type=VELOCITY

```

```

sand-1.sides, 1, 1
sand-1.sides, 2, 2
sand-1.sides, 3, 3
** Name: symmetry Type: Velocity/Angular velocity
*Boundary, type=VELOCITY
sand-1.symm, 3, 3
sand-1.symm, 4, 4
sand-1.symm, 5, 5
** -----
**
** STEP: gravity
**
*Step, name=gravity
*Dynamic, Explicit
, 12.
*Bulk Viscosity
0.06, 1.2
** Mass Scaling: Semi-Automatic
**           Whole Model
*Fixed Mass Scaling, dt=1e-05, type=below min
**
** BOUNDARY CONDITIONS
**
** Name: back Type: Velocity/Angular velocity
*Boundary, op=NEW, type=VELOCITY
sand-1.back, 1, 1
sand-1.back, 2, 2
sand-1.back, 3, 3
** Name: fixbottom Type: Velocity/Angular velocity
*Boundary, op=NEW, type=VELOCITY
sand-1.bottom, 2, 2
** Name: holdwheel Type: Velocity/Angular velocity
*Boundary, op=NEW, type=VELOCITY
extrudedwheel-1.HubRefPt, 1, 1
extrudedwheel-1.HubRefPt, 3, 3
extrudedwheel-1.HubRefPt, 4, 4
extrudedwheel-1.HubRefPt, 5, 5
** Name: sides Type: Velocity/Angular velocity
*Boundary, op=NEW, type=VELOCITY
sand-1.sides, 1, 1
sand-1.sides, 2, 2
sand-1.sides, 3, 3
** Name: symmetry Type: Velocity/Angular velocity
*Boundary, op=NEW, type=VELOCITY
sand-1.symm, 3, 3
sand-1.symm, 4, 4
sand-1.symm, 5, 5
**
** LOADS
**
** Name: gravity Type: Gravity

```

```

*Dload, amplitude=gravity
, GRAV, 1600., 0., -1., 0.
**
** INTERACTIONS
**
** Interaction: ContactPatch-sand
*Contact Pair, interaction=friction104, mechanical
constraint=PENALTY, cpset=ContactPatch-sand
sand-1.contact, extrudedwheel-1_OuterMembrane_CNS_
**
** OUTPUT REQUESTS
**
*Restart, write, overlay, number interval=24, time marks=NO
**
** FIELD OUTPUT: F-Output-1
**
*Output, field, time interval=3.
*Node Output
RF, U, V
*Element Output, directions=YES
LE, PE, PEEQ, S
*Contact Output
CSTRESS,
**
** HISTORY OUTPUT: H-Output-2
**
*Output, history, time interval=0.5
*Contact Output, cpset=ContactPatch-sand
CAREA, CFN1, CFN2, CFN3, CFNM, CFS, CFT, CMN, CMS, CMT, XN, XS, XT
**
** HISTORY OUTPUT: H-Output-1
**
*Output, history, variable=PRESELECT, time interval=0.5
*End Step
** -----
**
** STEP: rotation
**
*Step, name=rotation
*Dynamic, Explicit
, 15.
*Bulk Viscosity
0.06, 1.2
**
** BOUNDARY CONDITIONS
**
** Name: angular_velocity Type: Velocity/Angular velocity
*Boundary, op=NEW, amplitude=SU10, type=VELOCITY
extrudedwheel-1.HubRefPt, 6, 6, -0.8
** Name: back Type: Velocity/Angular velocity
*Boundary, op=NEW, type=VELOCITY

```

```

sand-1.back, 1, 1
sand-1.back, 2, 2
sand-1.back, 3, 3
** Name: fixbottom Type: Velocity/Angular velocity
*Boundary, op=NEW, type=VELOCITY
sand-1.bottom, 2, 2
** Name: holdwheel Type: Velocity/Angular velocity
*Boundary, op=NEW, type=VELOCITY
extrudedwheel-1.HubRefPt, 3, 3
extrudedwheel-1.HubRefPt, 4, 4
extrudedwheel-1.HubRefPt, 5, 5
** Name: sides Type: Velocity/Angular velocity
*Boundary, op=NEW, type=VELOCITY
sand-1.sides, 1, 1
sand-1.sides, 2, 2
sand-1.sides, 3, 3
** Name: symm Type: Velocity/Angular velocity
*Boundary, op=NEW, type=VELOCITY
sand-1.symm, 3, 3
sand-1.symm, 4, 4
sand-1.symm, 5, 5
**
** OUTPUT REQUESTS
**
*Restart, write, overlay, number interval=40, time marks=NO
**
** FIELD OUTPUT: F-Output-1
**
*Output, field, time interval=1.
*Node Output
RF, U, V
*Element Output, directions=YES
LE, PE, PEEQ, S
*Contact Output
CSTRESS,
**
** HISTORY OUTPUT: H-Output-2
**
*Output, history, time interval=0.5
*Contact Output, cpset=ContactPatch-sand
CAREA, CFN1, CFN2, CFN3, CFNM, CFS, CFT, CMN, CMS, CMT, XN, XS, XT
**
** HISTORY OUTPUT: H-Output-1
**
*Output, history, variable=PRESELECT, time interval=0.5
*End Step

```

REFERENCES

- [1] "The Vision for Space Exploration," National Aeronautics and Space Administration February, 2004.
- [2] B. H. Wilcox, "ATHLETE: An Option for Mobile Lunar Landers," in *Aerospace Conference, 2008 IEEE*, 2008, pp. 1-8.
- [3] B. H. Wilcox, *et al.*, "Athlete: A cargo handling and manipulation robot for the moon," *Journal of Field Robotics*, vol. 24, pp. 421-434, 2007.
- [4] V. Asnani, *et al.*, "The development of wheels for the Lunar Roving Vehicle," *Special Issue: Robotics*, vol. 46, pp. 89-103, 6 2009.
- [5] D. Stowe, *et al.*, "Designing a lunar wheel," presented at the 2008 ASME International Design Engineering Technical Conferences (ASME-DETC2008, ATTV-49981), Brooklyn, NY, 2008.
- [6] T. B. Rhyne and S. M. Cron, "Development of a Non-Pneumatic Wheel," *Tire Science and Technology*, vol. 34, pp. 150-169, 2006.
- [7] M. G. Bekker, *Theory of land locomotion; the mechanics of vehicle mobility*. Ann Arbor,: University of Michigan Press, 1956.
- [8] M. G. Bekker, *Introduction to terrain-vehicle systems*. Ann Arbor,: University of Michigan Press, 1969.
- [9] J. Y. Wong, *Theory of ground vehicles*, 3rd ed. New York: John Wiley, 2001.
- [10] V. Asnani, *et al.*, "The development of wheels for the Lunar Roving Vehicle," *Journal of Terramechanics*, vol. 46, pp. 89-103, 2009.
- [11] T. Aubel, "FEM Simulation of the Interaction between an Elastic Tyre and Soft Soil," presented at the Proceedings of the 11th International Conference; International Society for Terrain-Vehicle Systems, Lake Tahoe, NV, 1993.
- [12] A. Balla, "Bearing capacity of foundations," *ASCE -- Proceedings -- Journal of the Soil Mechanics and Foundations Division*, vol. 88, pp. 13-34, 1962.
- [13] M. G. Bekker, "A System of Physical and Geometrical Soil Values for determination of Vehicle Performance and Soil Trafficability," presented at the Proc. Interserv. Symp., Stevens Inst. of Tech. and Duke Univ., Office of Ord. Res., Durham, NC, 1955.
- [14] M. G. Bekker, *Off-the-road locomotion; research and development in terramechanics*. Ann Arbor,: University of Michigan Press, 1960.
- [15] M. G. Bekker, "Off-road locomotion on the moon and on earth," *Journal of Terramechanics*, vol. 3, pp. 83-91, 1966.
- [16] M. G. Bekker and A. V. Butterworth, "Terrain-vehicle system evaluation," *Journal of Terramechanics*, vol. 2, pp. 47-67, 1965.
- [17] M. Chinnakonda, "Design and analysis of CDM Swiss Tweel: Final Report," January 31, 2008 2008.
- [18] R. C. Chiroux, *et al.*, "Three-dimensional finite element analysis of soil interaction with a rigid wheel," *Applied Mathematics and Computation*, vol. 162, pp. 707-722, 2005.

- [19] C. A. Coulomb, "Essai sur une application des regles des maximix at minimis a quelques problemes de staique relatifs a l'architecture," *Mem. pres. par div. savants*, vol. 7, pp. 343-382, 1773.
- [20] F. L. DiMaggio and I. S. Sandler, "Material Models for Granular Soils," *Journal of the Engineering Mechanics Division, ASCE*, vol. 97, pp. 935-950, 1971.
- [21] D. C. Drucker and W. Prager, "Soil Mechanics and Plastic Analysis for Limit Design," *Quarterly Applied Mathematics*, vol. 10, pp. 157-165, 1952.
- [22] C. W. Fervers, "FE-Simulation of Tyre-Profile-Effects on Terrain Mobility of Vehicles," presented at the 6th European ISTVS Conference, "Off-Road Vehicles in Theory and Practice", Vienna, Austria, 1994.
- [23] C. W. Fervers, "Improved FEM simulation model for tire-soil interaction," *14th International Conference of the ISTVS*, vol. 41, pp. 87-100, 0 2004.
- [24] D. R. Freitag, *et al.*, "Wheels for lunar vehicles," *Journal of Terramechanics*, vol. 8, pp. 89-105, 1972.
- [25] M. Garber and J. Y. Wong, "Prediction of ground pressure distribution under tracked vehicles: Effects of design parameters of the track-suspension system on ground pressure distribution," *Journal of Terramechanics*, vol. 18, pp. 71-79, 6 1981.
- [26] J. P. Hambleton and A. Drescher, "Modeling wheel-induced rutting in soils: Indentation," *Journal of Terramechanics*, vol. 45, pp. 201-211, 12 2008.
- [27] J. P. Hambleton and A. Drescher, "Modeling wheel-induced rutting in soils: Rolling," *Journal of Terramechanics*, vol. 46, pp. 35-47, 4 2009.
- [28] J. P. Hambleton and A. Drescher, "On modeling a rolling wheel in the presence of plastic deformation as a three- or two-dimensional process," *International Journal of Mechanical Sciences*, vol. 51, pp. 846-855, Nov-Dec 2009.
- [29] C. He and D. Zeng, "GRC-1 Bender and Extender Element Test Report," Case Western Reserve University, Cleveland, OH March 30 2009.
- [30] C. He and D. Zeng, "Results of Consolidation Tests on GRC-1 Simulant," Case Western Reserve University, Cleveland, OH February 19 2009.
- [31] G. Heiken, *et al.*, *Lunar sourcebook : a user's guide to the moon*. Cambridge [England] ; New York: Cambridge University Press, 1991.
- [32] J. G. Hetherington and I. Littleton, "The rolling resistance of towed, rigid wheels in sand," *Journal of Terramechanics*, vol. 15, pp. 95-105, 1978.
- [33] W. N. Houston and L. I. Namiq, "Penetration resistance of lunar soils," *Journal of Terramechanics*, vol. 8, pp. 59-69, 1971.
- [34] JPL Robotics. (2010, May 6, 2010). *The ATHLETE Rover*. Available: <http://www-robotics.jpl.nasa.gov/systems/system.cfm?System=11>
- [35] L. L. Karafiath, "Plasticity theory and the stress distribution beneath wheels," *Journal of Terramechanics*, vol. 8, pp. 49-60, 1971.
- [36] K. U. Kim and B. S. Shin, "Modeling motion resistance of rigid wheels," *Journal of Terramechanics*, vol. 22, pp. 225-236, 1985.
- [37] J. L. Klosky, *et al.*, "Geotechnical Behavior of JSC-1 Lunar Soil Simulant," *Journal of Aerospace Engineering*, vol. 13, pp. 133-138, 2000.

- [38] K. Kogure, "External motion resistance caused by rut sinkage of a tracked vehicle," *Journal of Terramechanics*, vol. 13, pp. 1-14, 1976.
- [39] K. Kogure and S. Isobe, "On the motion resistance due to sinkage of tracked vehicle," *Journal of Terramechanics*, vol. 24, pp. 115-116, 1987.
- [40] K. Kogure and T. Kudo, "Shearing properties of sand under a repeated loading representing the ground pressure distribution of a tracked vehicle," *Journal of Terramechanics*, vol. 14, pp. 237-248, 1977.
- [41] K. Kogure, *et al.*, "A simplified method for the estimation of soil thrust exerted by a tracked vehicle," *Journal of Terramechanics*, vol. 19, pp. 165-181, 1982.
- [42] K. Kogure, *et al.*, "Prediction of sinkage and motion resistance of a tracked vehicle using plate penetration test," *Journal of Terramechanics*, vol. 20, pp. 121-128, 1983.
- [43] K. Kogure and N. Sugiyama, "On contact shape and soil thrust of tracked vehicles," *Journal of Terramechanics*, vol. 21, pp. 305-305, 1984.
- [44] K. Kogure, *et al.*, "Comparison of strength and soil thrust characteristics among different soil shear tests," *Journal of Terramechanics*, vol. 25, pp. 201-221, 1988.
- [45] P. V. Lade and J. M. Duncan, "Elastoplastic stress-strain theory for cohesionless soil," *Journal of the Geotechnical Engineering Division, ASCE*, vol. 101, p. 1037, 1975.
- [46] W. Li, *et al.*, "Trafficability analysis of lunar mare terrain by means of the discrete element method for wheeled rover locomotion," *Journal of Terramechanics*, vol. 47, pp. 161-172, 2010.
- [47] D. S. McKay, *et al.*, "JSC-1: A New Lunar Soil Simulant," presented at the Engineering, Construction, and Operations in Space IV, 1994.
- [48] J. L. McRae, "Theory for a towed wheel in soil," *Journal of Terramechanics*, vol. 1, pp. 31-53, 1964.
- [49] J. L. McRae, "Theory for a towed wheel in soil," *Journal of Terramechanics*, vol. 3, pp. 93-100, 1966.
- [50] J. L. McRae, "Theory for a powered wheel in soil," *Journal of Terramechanics*, vol. 4, pp. 31-43, 1967.
- [51] G. G. Meyerhof, "Ultimate bearing capacity of foundations," *Geotechnique*, vol. 2, pp. 301-330, 1951.
- [52] J. K. Mitchell, *et al.*, "Mechanical properties of lunar soil: Density, porosity, cohesion, and angle of internal friction," in *Proceedings of the Third Lunar Science Conference*, 1972.
- [53] O. Mohr, *Abhandlungen aus dem Gebiete der technischen Mechanik*, 2nd Ed. ed. Berlin: W. Ernst, 1914.
- [54] H. Nakashima, *et al.*, "Parametric analysis of lugged wheel performance for a lunar microrover by means of DEM," *Journal of Terramechanics*, vol. 44, pp. 153-162, 2007.
- [55] O. Onafeko and A. R. Reece, "Soil stresses and deformations beneath rigid wheels," *Journal of Terramechanics*, vol. 4, pp. 59-80, 1967.

- [56] H. A. Oravec, *et al.*, "The Development of a Soil for Lunar Surface Mobility Testing in Ambient Conditions," in *11th International Conference on Engineering, Science, Construction, and Operations in Challenging Environments 2008*, 2008.
- [57] J. V. Perumpral, *et al.*, "A numerical method for predicting the stress distribution and soil deformation under a tractor wheel," *Journal of Terramechanics*, vol. 8, pp. 9-22, 1971.
- [58] L. Prandtl, "Uber die Eindringungsfestigkeit (Harte) plastische Baustoffe und die Festigkeit von Schnieden," *Zeitschrift fur Angewandte Mathematik und Mechanik*, vol. 1, pp. 15-20, 1921.
- [59] H. Shibly, *et al.*, "An equivalent soil mechanics formulation for rigid wheels in deformable terrain, with application to planetary exploration rovers," *Journal of Terramechanics*, vol. 42, pp. 1-13, 2005.
- [60] J. D. Summers, "Development of a Lunar Capable Rover Wheel for a Modular Rover System: Analytical and Experimental Research," SC NASA EPSCoR Technical Report 2009.
- [61] E. Susila and R. D. Hryciw, "Large displacement FEM modelling of the cone penetration test (CPT) in normally consolidated sand," *International Journal for Numerical and Analytical Methods in Geomechanics*, vol. 27, pp. 585-602, Jun 2003.
- [62] M. Z. Tekeste, *et al.*, "Non-linear finite element analysis of cone penetration in layered sandy loam soil - Considering precompression stress state," *Journal of Terramechanics*, vol. 46, pp. 229-239, 2009.
- [63] K. Terzaghi, *Theoretical soil mechanics*. New York: J. Wiley and Sons, 1943.
- [64] V. K. Tiwari, *et al.*, "A review on traction prediction equations," *Journal of Terramechanics*, vol. 47, pp. 191-199, 2010.
- [65] H. Tresca, " Sur l'enoulement des corps solides soumis a de fortes pressions," *C.R. Acad. Sci. (Paris)*, vol. 59, p. 754, 1864.
- [66] R. Von Mises, "Mechanik der festen Korper im plastisch deformation," *Zustand. Nachr. Ges. Wiss. Gottingen*, p. 582, 1913.
- [67] S. Wakabayashi, *et al.*, "Design and mobility evaluation of tracked lunar vehicle," *Journal of Terramechanics*, vol. 46, pp. 105-114, 2009.
- [68] A. Wilkinson and A. DeGennaro, "Digging and pushing lunar regolith: Classical soil mechanics and the forces needed for excavation and traction," *Journal of Terramechanics*, vol. 44, pp. 133-152, 2007.
- [69] J.-Y. Wong and A. R. Reece, "Prediction of rigid wheel performance based on the analysis of soil-wheel stresses part I. Performance of driven rigid wheels," *Journal of Terramechanics*, vol. 4, pp. 81-98, 1967.
- [70] J.-Y. Wong and A. R. Reece, "Prediction of rigid wheel performance based on the analysis of soil-wheel stresses: Part II. Performance of towed rigid wheels," *Journal of Terramechanics*, vol. 4, pp. 7-25, 1967.
- [71] J. Y. Wong, *Theory of ground vehicles*. New York: Wiley, 1978.
- [72] J. Y. Wong, "An introduction to terramechanics," *Journal of Terramechanics*, vol. 21, pp. 5-17, 1984.

- [73] J. Y. Wong, "Recent developments in terrain-vehicle systems analysis," *Journal of Terramechanics*, vol. 22, pp. 245-247, 1985.
- [74] J. Y. Wong, "Computer aided analysis of the effects of design parameters on the performance of tracked vehicles," *Journal of Terramechanics*, vol. 23, pp. 95-124, 1986.
- [75] J. Y. Wong, "Some recent developments in vehicle-terrain interaction studies," *Journal of Terramechanics*, vol. 28, pp. 269-288, 1991.
- [76] J. Y. Wong, *Theory of ground vehicles*, 2nd ed. New York, N.Y.: J. Wiley, 1993.
- [77] J. Y. Wong, *Theory of ground vehicles*, 4th ed. Hoboken, N.J.: Wiley, 2008.
- [78] J. Y. Wong and W. Huang, ""Wheels vs. tracks" - A fundamental evaluation from the traction perspective," *Journal of Terramechanics*, vol. 43, pp. 27-42, 2006.
- [79] J. Y. Wong and J. Preston-Thomas, "On the characterization of the shear stress-displacement relationship of terrain," *Journal of Terramechanics*, vol. 19, pp. 225-234, 1983.
- [80] R. N. Yong and E. A. Fattah, "Prediction of wheel-soil interaction and performance using the finite element method," *Journal of Terramechanics*, vol. 13, pp. 227-240, 1976.
- [81] H.-S. Yu, *Plasticity and geotechnics*. New York, N.Y.: Springer-Verlag, 2006.
- [82] M. A. Crisfield, *Non-linear finite element analysis of solids and structures*. Chichester ; New York: Wiley, 1991.
- [83] (2007). *ABAQUS Analysis User's Manual* [HTML].
- [84] G. G. Meyerhof, "Some recent research on bearing capacity of foundations," *Canadian Geotechnical Journal*, vol. 1, pp. 16-26, 1963.
- [85] K. H. Roscoe, *et al.*, "On the Yielding of Soils," *Geotechnique*, vol. 8, pp. 22-53, 1958.
- [86] S. Harvey. (2008, 7/17/2009). *Solar System Exploration: Planets:Earth's Moon*. Available:
<http://solarsystem.nasa.gov/planets/profile.cfm?Display=Facts&Object=Moon>
- [87] S. Helwany, *Applied soil mechanics : with ABAQUS applications*. Hoboken, N.J.: John Wiley & Sons, 2007.
- [88] J. P. Hambleton, "Modeling Test Rolling in Clay," MS, Civil Engineering, University of Minnesota, Minneapolis, 2006.
- [89] C. S. Desai and H. J. Siriwardane, *Constitutive Laws for Engineering Materials with Emphasis on Geologic Materials*. Englewood Cliffs, NJ: Prentice-Hall, Inc., 1984.